University of California
Santa Barbara

Nonequilibrium control of colloidal interactions

A dissertation submitted in partial satisfaction
of the requirements for the degree

Doctor of Philosophy
in
Chemical Engineering

by

Yaxin Xu

Committee in charge:

Professor Sho C Takatori, Chair
Professor M Scott Shell
Professor Todd Squires
Professor Angela Pitenis

September 2024

The Dissertation of Yaxin Xu is approved.

Professor M Scott Shell

Professor Todd Squires

Professor Angela Pitenis

Professor Sho C Takatori, Committee Chair

September 2024

Nonequilibrium control of colloidal interactions

by

Yaxin Xu

Acknowledgements

I would like to acknowledge the people who have supported me over the course of my degree. First, I want to thank my advisor Sho Takatori for his scientific mentorship and for giving me the opportunity to pursue theoretical and computational projects at a time when I had no prior experience. His respect for my ability to perform and communicate my work has helped me grow as a research scientist. I am grateful for his patience, knowledge, enthusiasm, and curiosity, qualities which I will strive towards throughout my professional career.

I want to express my gratitude towards my thesis committee, professor Scott Shell, professor Todd Squires, and professor Angela Pitenis for their invaluable input on my thesis direction over the years. I am indebted to professor Joonwoo Jeong and professor Eujin Um for introducing me to fascinating experimental systems and exchanging fruitful ideas during their sabbatical at Santa Barbara.

I am beyond grateful for my wonderful colleagues in the Takatori lab – Kevin Modica, Daniel Arnold, Sachit Nagella, Kyu Hwan Choi, Titus Quah, Aakanksha Gubbala, Joeseph Barakat, Chris Browne, Dae Yeon Kim, Prabhat Jandhyala, Anika Jena, Stephanie Anujarerat, Lawrence Xi, and Lesley Lu. To the graduate students, it has been a privilege to share this research journey with all of you. I value the stimulating discussions, ideas, and collaborations that we have fostered over the years. Daniel and Kevin, it feels like just yesterday when we unboxed our new desktops and became the first three members to join the lab. I would also like to acknowledge my friends in the chemical engineering department, including Zachary Westman, Emily Schroeder, Justin Marlowe, Graham Reitz, Lazarina Butkovich, Xichen Liang, and Neha Padwal who have been amazing colleagues and given me many fond graduate school memories to look back on. I would also like to express my gratitude to my friends outside of Santa Barbara – Anna Resnick, Ellin

Chung, Meera Krishnamoorthy, Gyu Bin Jung, Janice Lee, Karen Malacon, Mindy Kim, Sandra Liu, Joseph Schneider, William Schmidt, Karim Lakhani, and many others for the companionship they have provided.

Words cannot express how grateful I am for the support from my family: my amazing mother, Shelley He for her love and sacrifices throughout my life. My father, Ran Xu, for being proud of my every achievement. My late grandfather, Deming Xu, who inspired me to pursue science from a very young age. My extended family, Tong Lu, Gilbert Galvani, Yingxian Wang, Chao Xu, Ying Xu, Caroline Zhang, and numerous others. Lastly, my boyfriend Greg who has been a source of love, strength, and patience over the years.

Finally, I'd like to acknowledge the department for granting me the Dow Discovery Fellowship to pursue innovative research and the Air Force for funding part of this work. Many thanks to the staff at the Center of Scientific Computing for maintaining the computational resources needed for my research.

Curriculum Vitæ

Yaxin Xu

Education

September 2024	Doctorate of Philosophy in Chemical Engineering (Expected), University of California, Santa Barbara. Dow Discovery Fellow from 2021 - 2024 *Advisor*: Professor Sho C. Takatori
June 2019	Bachelor of Science in Chemical Engineering, California Institute of Technology. *Advisor*: Professor André Hoelz Minor: English

Selected Presentations

1	Oral Presentation, Y. Xu, S. C. Takatori, "Dynamic surfactants for colloidal self assembly," American Physical Society March Meeting, Minneapolis, MN, March 2024
2	Oral Presentation, Y. Xu, S. C. Takatori, "Controlling nonequilibrium depletion interaction through timescale modulation," SoCal Polymers and Soft Matter Symposium, Los Angeles, CA, May 2023
3	Oral Presentation, Y. Xu, K. H. Choi, S. G. Nagella, S. C. Takatori, "Dynamic interfaces for contact-time control of colloidal interactions," AIChE Conference, Phoenix, AZ, Nov 2022
4	Poster Presentation, Y. Xu, S. C. Takatori, "Nonequilibrium colloidal interactions facilitated by surface-mobile polymer brushes," Gorden Research Conference: Colloidal, Macromolecular, and Polyelectrolyte Solutions, Ventura, CA, Nov 2022

Awards and Fellowships

2021-2024	Dow Discovery Fellowship, Dept. of Chemical Engineering, University of California, Santa Barbara
2018	Rose Hills Foundation Fellowship, California Institute of Technology
2016	Edward W. Hughes Research Fellowship, California Institute of Technology
2015	National Merit Scholarship

Publications

1 Y. Xu and S. C. Takatori. "Nonequilibrium interactions between multi-scale colloids regulate the suspension microstructure and rheology". *Soft Matter* 2023, **19**, 8531-8541 doi: 10.1039/D3SM00947E.
Y.X. participated in the conception of the project, conducted simulations, analyzed the data, and participated in the writing of the manuscript.

2 Y. Xu*, K. H. Choi*, S. G. Nagella, and S. C. Takatori. "Dynamic interfaces for contact-time control of colloidal interactions." *Soft Matter* 2023, **19**, 5692–5700. doi: 10.1039/D3SM00673E. (* denotes equal contribution)
Y.X. participated in the conception of the project, conducted simulations, analyzed the data, and participated in the writing of the manuscript.

3 Arnold, D. P., Xu, Y., and Takatori, S. C. "Antibody binding reports spatial heterogeneities in cell membrane organization." *Nature Communications* 2023, **14**, 2884. doi: 10.1038/s41467-023-38525-2.
Y.X. conducted the simulations, analyzed the data, and participated in the writing of the manuscript.

4 Y. Xu, P. Jandhyala, and S. C. Takatori. "Dynamic surfactants for colloidal self assembly." *submitted.*
Y.X. participated in the conception of the project, conducted simulations, analyzed the data, and participated in the writing of the manuscript.

Abstract

Nonequilibrium control of colloidal interactions

by

Yaxin Xu

Colloidal suspensions, consisting of particles of nano to micron scale dispersed in a medium, experience interparticle interactions that profoundly impact the macroscopic properties of soft materials, including stability, structure formation, and dynamics. A mechanism to dynamically tune these interactions can provide new avenues for self assembly and material processing. However, while traditional colloidal interactions have been well understood, it has been theoretically challenging to develop frameworks for nonequilibrium systems where interactions are dynamically evolving on the order of colloidal timescales.

In this thesis, I combine theoretical, experimental, and computational efforts to understand out-of-equilibrium colloidal interactions that are modulated by external stimuli. These nonequilibrium interactions result from microscopic relaxation timescales which are intrinsic to the colloidal system and may be controlled to vary suspension-level properties such as viscosity and morphology. First, as a proof of concept, I demonstrate precise control of dynamic pair interactions using surface-mobile polymer-coated colloids that are inspired by biological cell membranes. I show that entropically-driven surface rearrangement of polymers at colloidal contact interfaces enable an effective, dynamic interaction which is controllable over a range of pico-Newton forces and seconds timescales. Later in the thesis, I extend the theoretical framework to attractive colloids and show that polymer entropic effects regulate structure formation and phase stability in the context of colloidal self assembly. Unlike traditional interactions, we show

that surface-mobile polymers act as dynamic surfactants and allow colloids to acquire anisotropic shape throughout the assembly process. Microscopic polymer distributions impose unique geometric constraints between colloids that precisely control their packing in lamellar, string, and vesicle superstructures. Then, to understand the material properties of the suspension, I develop a first-principle framework that captures the multiscale coupling between microscopic timescales and macroscopic transport properties. Using microrheology in a bidisperse suspension as a case study, we demonstrate that effective depletion interactions between driven colloids are sensitive to particle timescales out of equilibrium and cannot be predicted by equilibrium-based pair potentials. We show that the interplay between Brownian relaxation timescales of different species plays a critical role in governing the viscosity of multi-component suspensions. Finally, in the context of biological systems, I use Brownian Dynamics simulations and polymer theory to investigate crowding effects on reconstituted and living cell membranes and characterize spatial heterogeneities. Overall, several systems are presented which exhibit multiscale, nonequilibrium interactions, and a framework connecting local dynamics to macroscopic material properties is developed.

Contents

Chapter 1

Introduction

Colloids are intrinsically complex systems consisting of mesoscopic particles that are dispersed in a continuum medium. Due to their nano to micrometer length scales, colloidal particles move under thermal-scale forces, also known as Brownian motion, which may be directly observed using optical methods such as light scattering and confocal microscopy. A central theme to colloidal systems is that the microscopic interactions between constituent particles dictate a wide range of collective, macroscopic behaviors, such as the fluid microstructure, transport properties, and phase transitions. By controlling the range and magnitude of these interparticle interactions, colloids become versatile systems for engineering novel soft materials and fluids.

Interactions between colloidal particles are facilitated by their local, microscopic environment and have been well studied both theoretically and experimentally. For example, grafting polymer brushes onto colloidal surfaces results in a sterically repulsive force that helps to stabilize a suspension against aggregation. [1, 2, 3] Other common types of interparticle interactions include electrostatic interactions, modeled by DLVO theory, and depletion attraction due to nonadsorbing polymers, which is captured through Asakura Oosawa-type potentials.[4] Furthermore, recent works have functionalized the

surfaces of colloids with biological components such as single-stranded DNA to engineer programmable, specific interactions and modulate macroscopic phenomena such as self assembly of colloidal superstructures.[5, 6, 7, 8] In modelling these colloidal interactions, one typically assumes a separation of timescales between the rapid physical relaxation of the local species, whether it be ions, polymers, or other surface-bound species, and the colloidal Brownian diffusion to obtain a 'static' interparticle potential, which solely depends on the instantaneous separation between colloids.[9, 10, 11] Such equilibrium interactions are convenient for both theoretical and computational treatment. For example, interparticle potentials may be directly applied to perform large scale Brownian Dynamics simulations to understand macroscopic properties such as pressure and viscosity.

In some cases though, nonequilibrium processes such as external, time-varying force fields[12], hydrodynamic flows [13] or kinetic arrest [14] may reorganize colloids faster than the equilibration time of the local environment. While colloids at equilibrium follow Boltzmann-type distributions and well-defined thermodynamics, the physical mechanisms governing nonequilibrium colloidal systems are less understood. Examples of dynamic colloidal systems include self-propelling particles that exhibit collective motion, paramagnetic colloids that adopt string-like phases under externally toggled magnetic fields, and dynamic bonds between particles that break and reform at characteristic rates. Since pairwise potentials developed for equilibrium and near-equilibrium systems likely do not apply well under these highly dynamic environments, a new theoretical framework to understand nonequilibrium colloidal interactions is desirable.

In this thesis, I present several colloidal systems that exhibit unique, dynamic interactions when driven out of equilibrium. In one study, we investigate interacting colloids with surface-mobile, end-tethered biopolymers, inspired by the biological cell surface, or glycocalyx. The mammalian glycocalyx consists of a phospholipid bilayer onto which

many macromolecules, proteins, and biopolymers are anchored. The underlying bilayer acts as a 2-dimensional fluid and enables surface diffusion of the various species, which is critical in regulating cell-cell signalling and other physiological functions.[15, 16] In one work, I model the mechanical properties of bulky, disordered membrane proteins to investigate how surface mobile species regulate spatial heterogeneity and binding dynamics near the cell surface. Additionally, inspired by the biological interface, I aim to modulate the intrinsic timescales at colloidal contacts to engineer a dynamic pair potential for multiscale control of colloidal interactions out of equilibrium. In another study, I focus on depletion-type interactions in bi-disperse colloid polymer suspensions and demonstrate how out-of-equilibrium distributions of polymers induce colloidal microstructures and rheology that cannot be predicted by classic, equilibrium-based frameworks. In my research, I combine analytical theory, Brownian Dynamics simulations, and reconstituted experiments to understand the multiscale, hierarchical coupling between macroscale colloidal processes and molecular interfacial dynamics. I aim to advance our basic understanding of nonequilibrium colloidal interactions to achieve exquisite control over structure and material properties under dynamic environments.

This thesis consists of independent chapters that are presented in a form suitable for publication. The first chapter has provided an general introduction to colloidal interactions out of equilibrium. Subsequent chapters provide a more in-depth analysis of the relationship between dynamic interactions and various macroscopic behaviors exhibited by colloidal particles. I lay the groundwork in Chapter 2 by introducing a theoretical and experimental proof of concept for realizing non-equilibrium interactions between pairs of colloids using dynamic contact interfaces, inspired by the mammalian cell glycocalyx. I will describe how novel classes of surface-mobile polymers can influence the colloidal interactions dynamically. In Chapter 3, I discover that attractive colloids with surface-diffusing polymers self assemble adopt anisotropic shapes and form unique macroscopic

morphologies. In Chapter 4, I demonstrate that simple bi-disperse colloidal suspensions experience non-equilibrium depletion interactions and that the multi-scale dynamics precisely control the suspension microrheology. Finally, in Chapter 5, I return to biological systems and apply simulations and theory to describe crowding effects on reconstituted and living cell membranes.

Bibliography

[1] Jacob N. Israelachvili. "Intermolecular and Surface Forces, Third Edition". In: *Intermolecular and Surface Forces, Third Edition* (2010), pp. 1–674.

[2] P. G. de Gennes. *Polymers at an interface; a simplified view*. 1987.

[3] S. T. Milner. "Polymer Brushes". In: *Science* 251.4996 (Feb. 1991), pp. 905–914.

[4] W. B. Russel, D. A. Saville, and W. R. Schowalter. *Colloidal Dispersions*. Cambridge Monographs on Mechanics. Cambridge University Press, 1989.

[5] A. Paul Alivisatos et al. "Organization of 'nanocrystal molecules' using DNA". In: *Nature 1996 382:6592* 382.6592 (1996), pp. 609–611.

[6] P. J. Santos, T. C. Cheung, and R. J. Macfarlane. "Assembling Ordered Crystals with Disperse Building Blocks." In: *Nano Lett.* 19 (2019), pp. 5774–5780.

[7] Gang Chen et al. "Regioselective surface encoding of nanoparticles for programmable self-assembly". In: *Nature Materials* (2018).

[8] Chad A. Mirkin et al. "A DNA-based method for rationally assembling nanoparticles into macroscopic materials". In: *Nature 1996 382:6592* 382.6592 (1996), pp. 607–609.

[9] Federica Loverso, Sergei A. Egorov, and Kurt Binder. "Interaction between polymer brush-coated spherical nanoparticles: Effect of solvent quality". In: *Macromolecules* 45.21 (Nov. 2012), pp. 8892–8902.

[10] S A Egorov. "Interactions between polymer brushes in solvents of variable quality: A density functional theory study". In: *Journal of Chemical Physics* 129.6 (2008), p. 64901.

[11] Stefano Angioletti-Uberti, Bortolo M. Mognetti, and Daan Frenkel. "Theory and simulation of DNA-coated colloids: a guide for rational design". In: *Physical Chemistry Chemical Physics* 18.9 (Feb. 2016), pp. 6373–6393.

[12] James W. Swan et al. "Multi-scale kinetics of a field-directed colloidal phase transition". In: *Proceedings of the National Academy of Sciences* 109.40 (Oct. 2012), pp. 16023–16028.

[13] J Vermant and M J Solomon. "Flow-induced structure in colloidal suspensions". In: *Journal of Physics: Condensed Matter* 17.4 (Feb. 2005), R187–R216.

[14] P. Segrè et al. "Glasslike Kinetic Arrest at the Colloidal-Gelation Transition". In: *Physical Review Letters* 86.26 (June 2001), pp. 6042–6045.

[15] Monks CR et al. "Three-dimensional segregation of supramolecular activation clusters in T cells". In: *Nature* 395 (1998), pp. 82–86.

[16] Simon J. Davis and P. Anton van der Merwe. "The kinetic-segregation model: TCR triggering and beyond". In: *Nature Immunology 2006 7:8* 7.8 (2006), pp. 803–809.

Chapter 2

Dynamic pair interactions mediated by surface-mobile polymers

1. This chapter includes content from our previously published article:

   [1] Y. Xu*, K. H. Choi*, S. G. Nagella, and S. C. Takatori. "Dynamic interfaces for contact-time control of colloidal interactions." *Soft Matter* 2023, **19**, 5692–5700. doi: 10.1039/D3SM00673E.

   * denotes equal contribution

   Y.X. participated in the conception of the project, conducted simulations, analyzed the data, and participated in the writing of the manuscript.

2.1 Introduction

The material properties of colloidal suspensions depend on the multibody interactions between constituent particles.[1] These interactions may be programmed through functionalizing colloids with surface species such as DNA linkers [2, 3, 4, 5] or polymer brushes [6, 7] to guide or hinder colloidal aggregation. In modelling such systems,

one typically assumes a separation of timescales between the rapid relaxation of surface species and the colloidal Brownian diffusion [8] to obtain an effective, 'static' pair potential, which solely depends on the instantaneous pair separation.[9, 10] Although only exact at equilibrium, static potentials have been applied successfully to describe many colloidal suspensions out of equilibrium.

In some cases, however, nonequilibrium processes such as hydrodynamic flows [11] or kinetic arrest [12] drive colloids together or apart faster than the surface species equilibration, resulting in a nontrivial interplay between the macroscopic process timescale and kinetics at the contact interface. For instance, the stiffening of particle-particle contacts in dense colloidal suspensions can lead to logarithmic growth in the elastic moduli over time, in the absence of microstructural changes. [13, 14] Additionally, theoretical work has shown that suspensions of polymer-grafted particles can exhibit shear thickening through hydrodynamic interactions and contact relaxation.[15, 16] Dynamical interactions are also biologically relevant; cell membranes are coated by receptors and biopolymers which spatially rearrange over cell-cell contact timescales of seconds to minutes to trigger T cell activation.[17, 18] In these systems, a static potential is likely inadequate for predicting nonequilibrium pairwise interactions. By modulating the intrinsic timescales at colloidal contacts, we aim to engineer a dynamic pair potential for multiscale control of colloidal interactions out of equilibrium.

Consider the system in Fig 2.1: two colloids are coated by end-grafted polymers whose grafting sites are free to diffuse laterally along the surfaces. Colloids are brought to a small separation distance instantaneously and held fixed at those positions. Shortly after contact, colloids experience a strong steric repulsion due to polymer overlap between opposing surfaces. However, through grafting-site diffusion and chain relaxations at longer times, the polymers assume configurations that lower their overall energy, thereby reducing the effective repulsion experienced by the colloids. This contact-time dependent

interaction relaxes over colloidal timescales and can affect overall suspension dynamics. Mechanistic understanding of these interactions has not been previously considered theoretically or experimentally.

In this work, we combine theory, simulations, and experiments to directly measure the force transmission between two colloidal particles coated by surface-mobile polymers as a function of their contact time. We find that the relaxation timescale of this dynamic interaction is modulated by nonequilibrium protocols such as colloid approach speed. Our mechanical understanding of dynamic pair interactions may help predict the out of equilibrium assembly of colloidal structures.

This work is organised as follows. A brief overview of the theoretical model and simulations is presented in Section 2 and the experimental method is detailed in Section 3. In Section 4 we present results and analysis of contact-time dependent intercolloidal forces between two polymer-coated colloids as the system relaxes toward equilibrium and show how these interactions are precisely governed by nonequilibrium forcings. The work closes with a discussion of these data in Section 5 as well as a simple demonstration of how surface modifications may be leveraged to engineer different types of dynamic interactions.

2.2 Theoretical Model

2.2.1 Smoluchowski Theory

For the system shown in Fig. 2.1, we now provide an overview of an analytical theory to capture relaxation dynamics of surface-bound, semi-rigid polymers. The probability density $\rho(\mathbf{h}, t|H)$ of finding a monomer at position $\mathbf{h}$, given two colloids of size d_c at a

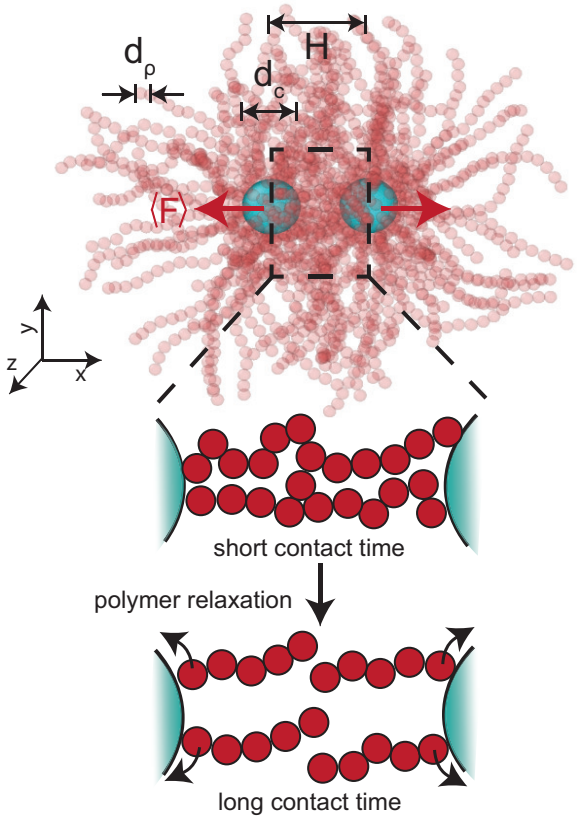

Figure 2.1: Brownian Dynamics (BD) snapshot of colloids coated with surface-mobile polymers. Two colloids (blue) with diameter d_c at separation H are coated by same-length, end-grafted polymers (red) with surface-mobile grafting sites, mean height h_0, bead diffusion coefficient D_ρ and bead diameter d_ρ. When the colloids are brought into a distance $H \ll 2h_0$ over a short timescale $\tau_{\text{process}} \ll d_c^2/D_\rho$, the polymers are forced into nonequilibrium configurations and generate a large effective force $\langle F \rangle$ between the colloids. As the polymers relax towards equilibrium, the effective interactions decay.

separation H, satisfies the Smoluchowski equation:

$$\frac{\partial \rho}{\partial t} = -\nabla_{\mathbf{h}} \cdot \mathbf{j} \tag{2.1}$$

where the flux contains thermal and interparticle contributions:

$$\mathbf{j} = -D_\rho \nabla_{\mathbf{h}} \rho - D_\rho \rho \nabla_{\mathbf{h}} V(\mathbf{h}|H)/k_{\text{B}}T. \tag{2.2}$$

Neglecting hydrodynamic interactions for now, D_ρ is simply the Stokes Einstein Sutherland (SES) diffusivity of the monomer. One may opt for a more sophisticated form of D_ρ for surface-mobile, end-grafted polymers, but we will use the SES diffusivity for simplicity. Assuming semidilute polymers, the interparticle potential $V = V_{\text{brush}} + V_{\text{HS}}$ is a sum of the entropic penalty of chain stretching and hard-core repulsion between monomers (see SI for functional forms). Normally, the translational motion of the colloids would also produce an advective particle flux contribution, $v\rho\mathbf{e}_x$, which scales with the approach velocity, v.[19, 20, 21, 22] Because our model aims to capture the transient relaxation after colloidal motion has ceased ($v = 0$ for $t \geq 0$), we choose to set an initial, nonequili-

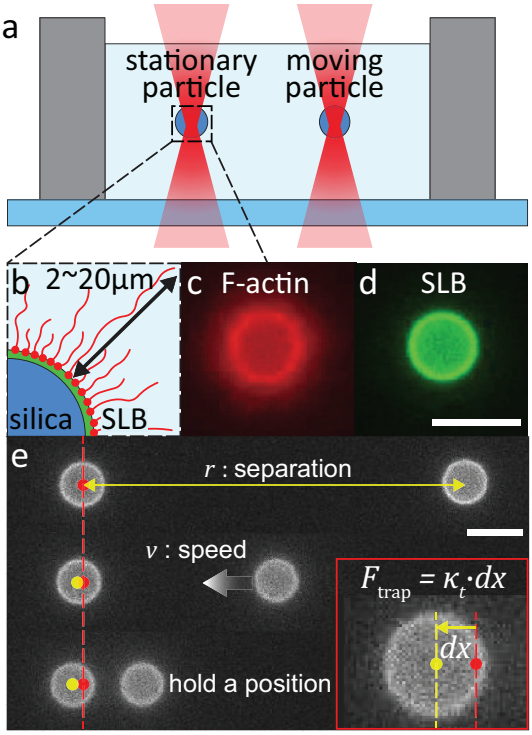

Figure 2.2: Experimental setup of a pair of Filamentous actin (F-actin) coated colloidal particles. (a) Schematic of optical laser tweezers and trapped particles in solution. (b) F-actin length ranges from 2μm to 20μm, with a mean $h_0 \approx 5\mu$m. (c,d) Fluorescence images of F-actin (red) bound to the lipid bilayer (green) containing polyhistidine tagged gelsolin and DGS-NTA(Ni). (e) Force measurement method. Inset shows the displacement from laser focus (red dot) to the mass center of the stationary colloid (yellow dot). All scale bars are 5μm.

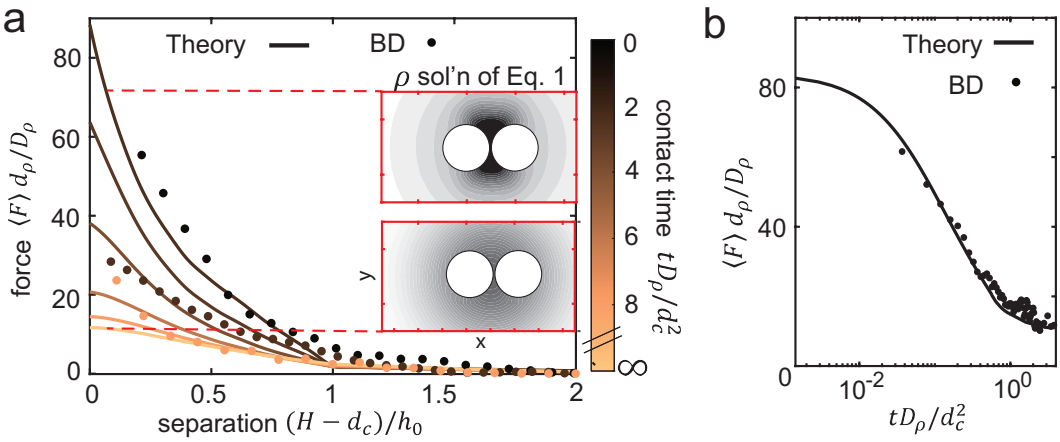

Figure 2.3: Effective repulsive forces between polymer-grafted colloids decay as a function of colloid-colloid contact time due to polymer relaxation at the contact interface. (a) Effective colloidal forces as a function of H for short (black) to long (yellow) contact times. Inset shows numerical solutions of Eq. 4.16-4.17 for polymer density ρ at short (top) and long (bottom) contact times, with the late stage, infinite time force measured at $tD_\rho/{d_c}^2 = 20$. Dark regions indicate higher polymer density. (b) Effective colloidal force as a function of contact time at colloidal contact, $H = d_c$. Solid lines are numerical solutions to Eq. 4.16-4.17, and markers are BD simulations.

brated concentration field to represent the state of monomers at $t = 0$ (see SI). Eq. 4.16 is numerically evaluated using the finite element software package FreeFEM++ [23] for an arbitrarily-large 3-dimensional volume which includes both colloidal particles and the two polymer brush domains.

2.2.2 Brownian Dynamics Simulations

To validate our theoretical model, we also perform coarse-grained Brownian Dynamics (BD) simulations using HOOMD-Blue, a GPU-accelerated simulation package (Supp. Video 1-3).[24] All particles in the simulation follow the overdamped Langevin equation of motion:

$$\zeta \frac{\Delta \mathbf{x}_i}{\Delta t} = \underbrace{\mathbf{F}_i^{\mathrm{P}}}_{\text{interactions}} + \underbrace{\mathbf{F}_i^{\mathrm{R}}}_{\text{Brownian}} \tag{2.3}$$

with contributions from interparticle interactions and thermal forces satisfying fluctuation dissipation theory. In Eq. 4.18, $\mathbf{x}_i$ is the position of particle i, and $\zeta = 3\pi\eta d_\rho$ is the drag coefficient. Polymers are modeled with identical properties using a Kremer-Grest bead-spring model with semi-flexibility,[25] where the grafting site is allowed to undergo diffusive translation along the surface (Fig. 2.1). To quantify the effective colloidal interaction mediated by brushes of mean height h_0, polymerization M and surface density n_ρ, we compute the force $\langle F(\mathbf{h}, t|H)\rangle$ exerted by polymers on the colloids along their line of centers, where $F = -n_\rho M \partial_H V$ and the brackets $\langle ...\rangle = \frac{1}{2}\int \rho ... d\mathbf{h}$. Polymer parameters and interactions with are chosen to match the experimental system (see SI).

2.3 Experimental Methods

In this section, we briefly summarize our experimental realization of surface-mobile polymer-coated colloidal particles and our interparticle force measurement technique. All force measurements were conducted using the optical tweezer (OT) setup described in Fig. 2.2a.[26] Two polymer-grafted beads were held in two separate optical traps focused more than 40μm from the bottom cover slip. A supported lipid bilayer (SLB) containing dioleoyl-sn-glycero-3-phosphocholine (DOPC) was constructed on $d_c = 4\mu$m silica beads to enable mobility of surface species (Fig. 2.2b,d).[27] We chose filamentous actin (F-actin) as the grafted polymer for its ability to polymerize to large lengths[28] and well-known mechanical properties.[29, 30] F-actin is known to polymerize to large length distributions,[28] and polymerization was quenched after reaching a length distribution of $2 - 20\mu$m by washing out unreacted materials. F-actin was end-grafted on the SLB by 6x-histidine tagged gelsolin to an anchoring lipid, 1,2-dioleoyl-sn-glycero-3-[(N-(5-amino-1- carboxypentyl)iminodiacetic acid)succinyl] (DGS-NTA(Ni)), which was doped in the bilayer over a range of $0 - 10\%$ to vary F-actin surface density between $n_{\text{actin}} \approx$

$0 - 12,000/\mu\text{m}^2$ (Fig. 2.2c, Supp. Video 4, see SI for F-actin density characterization). The mean separation between grafting sites is $10 - 20$nm, such that F-actin assumes a brush configuration. 1,2-dioleoyl-sn-glycero-3-phosphoethanolamine (DOPE) labeled with Atto-488 was added at 1% for fluorescence.

To characterize pair interactions out of equilibrium, a pair of colloids is placed in separate optical traps; one trap is stationary whereas the other trap translates at a fixed speed ($v = 0.5-10\mu$m/s) to bring the colloids from a large separation (35μm) to a closest distance of $400-500$ nm before being fixed at this position for 20s (Fig. 2.2e, Supp. Video 5-6). We then measured the stationary colloid displacement about its trap center at every time step, dx, following $\langle F \rangle = F_{\text{trap}} = \kappa_{\text{t}} \cdot dx$, with a trap stiffness $\kappa_{\text{t}} = 0.5 - 0.7\text{pN}/\mu\text{m}$. During the approach step, we did not observe convection-induced accumulation of F-actin to the rear of the colloid (Supp. Video 6), indicating that hydrodynamic forces do not macroscopically perturb the polymer distribution.

2.4 Results

2.4.1 Brush-mediated interactions relax over timescale of colloidal contact

In Fig. 2.3a, we plot the force exerted between the colloids as a function of the inter-colloidal separation H for a family of contact times. The inset shows cross-sectional monomer density solutions to Eq. 4.16 - 4.17 for short and long contact times. At a given separation, we observe that the repulsive forces decay as a function of contact time. At small times, $t \ll d_{\text{c}}^2/D_\rho$, we observe a repulsive force that strengthens when brushes are fully overlapped, $(H - d_{\text{c}}) = h_0$, resulting from high osmotic pressure across the contact interface.[1] When the contact times exceed the diffusive timescale for the

grafting site to explore the colloidal surface, $\tau_{\mathrm{R}} \sim d_{\mathrm{c}}^2/D_\rho$, polymers chains and their grafting sites have substantially depleted from the interfacial region, resulting in an order of magnitude decrease in force. Unlike static pair potentials, this dynamic interaction is unusual because the colloids' instantaneous separations do not fully capture their force and stress transmission. We also note that this dynamic interaction is governed by the intrinsic, diffusive timescales of the polymers and is distinct from externally-imposed, time-varying potentials.[31, 32, 33]

In the late stage, infinite time limit, taken to be $tD_\rho/{d_{\mathrm{c}}}^2 = 20$, compressed polymers fully relax through diffusive redistribution of their grafting sites out of the contact interface and spatial reorganization of the polymer chain. In Fig. 2.3b, we plot the colloidal force as a function of contact time when colloids are in contact at the closest separation, $H = d_c$. We show that the force decays exponentially towards the equilibrium value, suggesting a characteristic relaxation timescale associated with polymer reorganization over the colloidal surface. This relaxed force is weaker than static repulsion between polymer brushes whose grafting sites are not laterally mobile.[34, 1, 35, 36] We find good agreement between theoretical predictions and our BD simulations despite the simplicity of our polymer model.

2.4.2 Surface-mobile F-actin mediates dynamic colloidal interactions

So far, we have demonstrated that a nonequilibrium interaction exists between colloids coated with surface-mobile polymer layers through a theoretical model and BD simulations. Next, we present the experimental realization of this system. In Fig. 2.4, we plot the interaction force against time for various approach velocities, where the translating trap stops motion at $t = 0$. We observed that the repulsive forces increase as the two

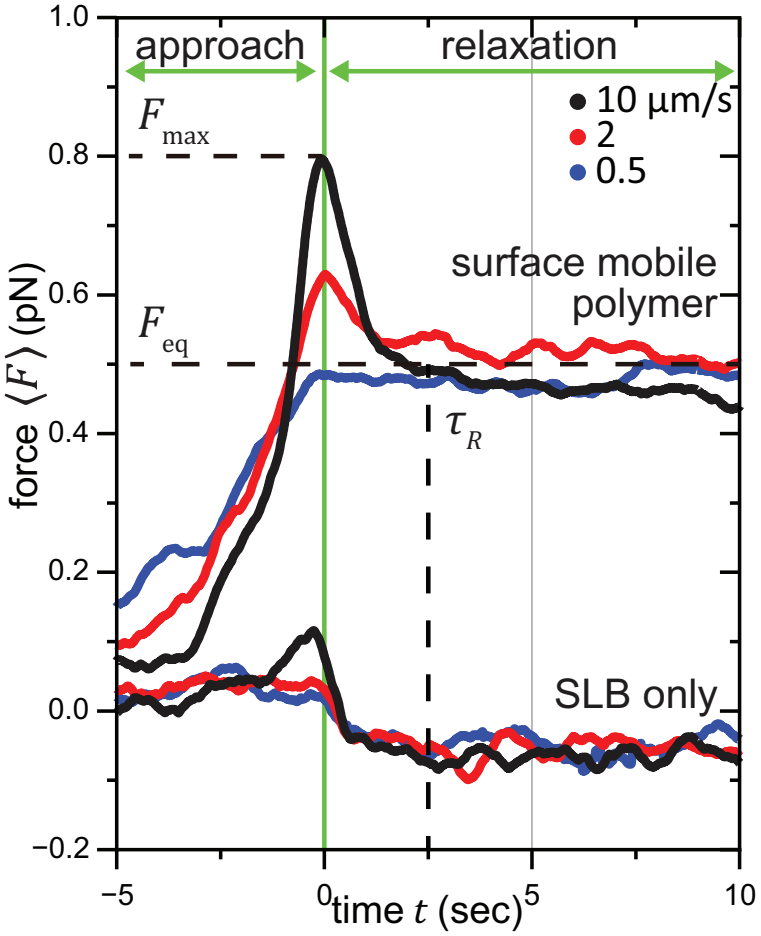

Figure 2.4: F-actin grafted on lipid bilayer-coated silica colloids generates contact–time dependent interactions between colloids. Plot shows force as a function of time on beads with F-actin surface density $n_{\text{actin}} \approx 12,000/\mu\text{m}^2$ and a separate measurement for bilayer-only control. Solid lines are time-average curves with approach speeds of 0.5 μm/s (blue), 2μm/s (red), and 10μm/s (black), averaged over five colloidal pairs. Times $t < 0$ correspond to the approach step and $t \geq 0$ represent times when the colloids are at close contact (see SI Fig. 4).

colloids approach for times $t < 0$ due to F-actin interactions with the opposing colloidal surface, and is maximized at the closest separation, $\langle F(t=0)\rangle = F_{\max}$. At the fastest approach velocity, 10μm/s (black curve), the repulsive force relaxes from $F_{\max}$ to the equilibrium force, $F_{\rm eq}$, on an observable timescale, $\tau_R \approx 2.5$s, consistent with literature values for F-actin spatial reorganization over the colloidal size, $\tau_R \sim 4\mu\text{m}^2/D_a \approx 2.7$s, where $D_a = 1.5\mu\text{m}^2/\text{s}$ is F-actin diffusivity in solution.[37] We therefore rationalize that the in-plane fluidity of the membrane surface enables an exquisite control over the reorganization of F-actin at the contact interface and the force transmission between the colloids.

At slow approach velocities, 0.5μm/s, the repulsive force between the colloids immediately equilibrates — their interactions are quasi-static because the polymers have sufficient time to reorganize during every step of approach. This equilibrium force is related to a potential of mean force, $F_{0.5\mu\text{m/s}} = -\int \rho_{\rm eq}\partial_{\rm H} V d\mathbf{h}$ where $\rho_{\rm eq} = e^{-V/k_{\rm B}T}$ is the equilibrium monomer distribution, and is analogous to the infinite contact time limit of Fig. 2.3a where interfacial polymers have fully relaxed.

As a control, we show that the forces between SLB-coated colloids without F-actin remained approximately zero throughout, except for the small peak associated with a lubrication force at the largest velocity. The small negative $F_{\rm eq} \approx 50$fN indicates a weak, van-der Waals-type attractions.

Figure 2.4 is an experimental realization of our simulations in Fig. 2.1 and 2.3, where two colloids placed quickly into contact experienced a repulsive force that decays with contact time. Using our membrane-coated colloids with different surface conditions, one can create a range of designer pair potentials with tunable contact-time interactions, as demonstrated theoretically in Fig. 2.3.

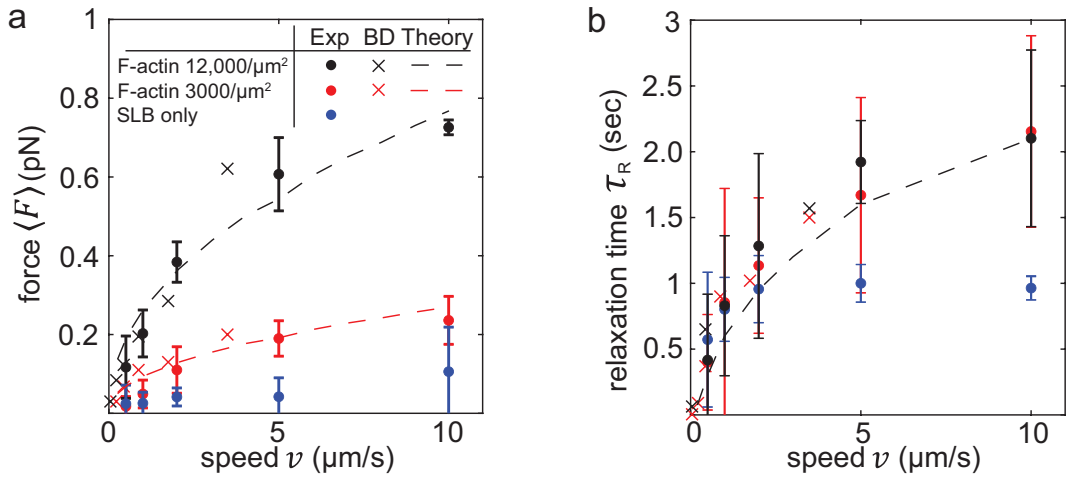

Figure 2.5: Nonequilibrium process timescale modulates strength and relaxation of dynamic colloidal interactions. (a) Effective colloidal force versus approach speed at a center-center separation of 8μm, for large actin density ($12,000/\mu\text{m}^2$) (black), moderate actin density ($3,000/\mu\text{m}^2$) (red), and SLB only (blue). (b) Relaxation time from peak force versus approach speed. Dashed curves are solutions to Eq. 4.16-4.17, filled circles are experiments, and crosses are BD simulations.

2.4.3 Nonequilibrium timescales compete with surface polymer relaxation

The contact-time dependent interactions in Fig. 2.3 and 2.4 arise from the nonequilibrium distributions of interfacial polymers. Therefore, any process that moves the colloids in and out of contact on a timescale that competes with polymer relaxation, such as hydrodynamic fluid flows and other non-conservative body forces, can induce a dynamic interaction. To understand the impact of these competing timescales, we systematically varied the approach velocities of the colloids leading to their closest separation.

In Fig. 2.5a, we measured the effective force as a function of approach velocity at a fixed colloidal separation ($H = 8\mu$m) for two actin surface densities, $12,000/\mu\text{m}^2$ and $3,000/\mu\text{m}^2$. We observe that the effective colloidal force increases for higher surface densities, consistent with our hypothesis that the polymer-mediated repulsion is induced by increased osmotic pressure (Fig. 2.3a, inset). Also, the forces generally increase for higher

approach speeds, which we attribute to the degree of F-actin compression at the contact interface. During a "fast" approach ($v > 2\mu$m/s), F-actin of mean height $h_0 \sim 5\mu$m is compressed at a timescale $\tau_{\text{process}} \sim h_0/v = 2.5$s, which is comparable to the F-actin reorganization on the colloid surface. Thus, polymers compress without having sufficient time to explore favorable configurations. Higher approach speeds induce an increasingly dense layer of interfacial F-actin, generating stronger forces. This repulsion begins to plateau at the highest approach speed (10μm/s), possibly because polymers cannot infinitely accumulate. Note in Fig. 2.5a that the theoretical polymer configurations were generated for the initial approach (see SI for polymer initialization).

Our results confirm that faster approach processes drive polymers further away from their equilibrium distribution. Therefore, the approach timescale should not only influence the strength of polymer-mediated interactions but also control their relaxations toward equilibrium. In Fig. 2.5b, we plot the characteristic relaxation time τ_{R} of the effective force as a function of approach speed. In experiments, theory, and simulations, τ_{R} is taken to be the time for the instantaneous force to relax 90% toward the equilibrium value F_{eq} from the peak value, F_{max}. We observe that the relaxation time increases with faster approach speeds, suggesting that polymers equilibrate more slowly when strongly compressed.

Interestingly, the relaxation time is independent of the F-actin surface density, as shown in Fig. 2.5b. From our flux expression (Eq. 4.17), we conclude that it is the *gradients* in polymer concentration along the colloidal surfaces, $\nabla_{\mathbf{h}}\rho$, which drive relaxation towards equilibrium. This is reminiscent of Marangoni forces that drive surfactant molecules from high to low concentrations.[38] Such a trend supports our theoretical framework of modeling relaxation as a diffusion-mediated process, as opposed to other mechanisms that depend on polymer concentration.

2.4.4 Fluid-mediated effects on colloidal interactions

Lubrication approximation on bare particles

In Fig. 2.5, we have found that a free-draining model of the F-actin layer sufficiently captures the key physics behind our experimental trends. In general, however, fluid-mediated effects cannot be neglected. As a control, we now show that forces between SLB-coated colloids without F-actin scale linearly with approach speed, which is consistent with low-Reynolds number hydrodynamics (Fig. 2.5a, Supp. Video 7).[39]

As shown in Fig. 2.2e, the moving bead is brought to the stationary particle at a fixed speed until they reach close contact. For bare, SLB-only colloids, the observed maximum in the force $F_{\max}$ primarily due to fluid-mediated hydrodynamic interactions.

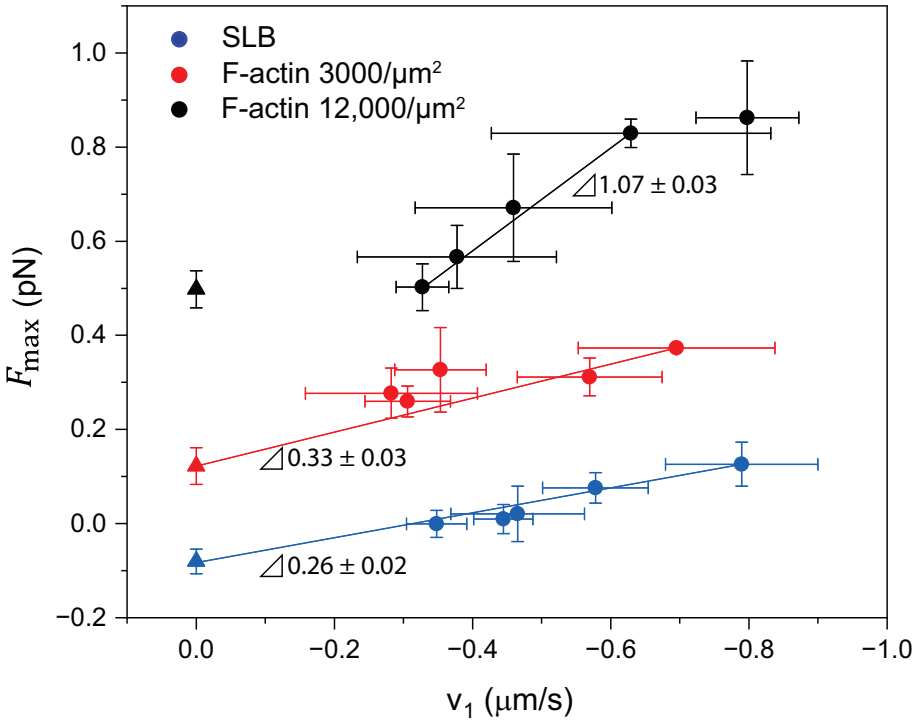

Figure 2.6: Maximum trapping forces on the stationary bead generally scale linearly with the instantaneous velocity v_1, upon closest approach with the moving particle. The instantaneous bead velocities v_1 were determined by time-differentiating the stationary bead displacements. Forces at $v_1 = 0$ are the equilibrium interactions between the particles, taken to be the "quasi-static" limit.

During the approach process, the translating colloid diverts fluid from the interfacial gap between it and stationary particle, generating viscous drag forces. When the interfacial gap thickness is much smaller than the particle radius, the pressure difference between the interface and the surrounding bulk medium increases significantly to expel fluid from the thin film. Reynolds considered the asymptotic limit of a sphere approaching a planar surface and determined that the hydrodynamic force scales sensitively with the aspect ratio between the gap size ϵ and the particle diameter d_c.[40] Equivalently, here we consider the two particles asymptotically approaching the symmetry plane between them, i.e. $\epsilon \equiv (H - d_c)/d_c \ll 1$, such that, to leading order, the lubrication force due to the squeezing motion is given by $F^H \sim 3\pi\eta d_c v \epsilon^{-1} + O(\ln(\epsilon))$.[41]

In Fig. 2.6 we compare the measurements of F_{max} with the instantaneous velocities of the stationary bead v_1 along the direction of tweezer motion, computed from the displacement time-trajectories. The slope of the force-velocity data provides the hydrodynamic resistance. Upon closest approach ($H - d_c \approx 400$nm), the stationary particle moves away from the incoming bead due to the hydrodynamic force (see Supp. Video 7). When the moving particle stops translating, the stationary bead reverses its motion. This momentary configuration of the beads is convenient to analyze, as the moving particle is now held in place ($\mathbf{v_2} = \mathbf{0}$) while the stationary particle moves towards the laser focus at an instantaneous velocity $\mathbf{v_1}$. In general, there are additional resistances due to the coupling between the forces and rotations. For example, a torque-free particle can simply rotate in response to local shearing by the fluid flow, effectively reducing the translational resistance. However, in the thin-gap limit, the leading-order resistance due to the force-rotation coupling scales as $\ln(\epsilon)$.[42] Therefore, we expect the force response on the stationary colloid to behave as

$$\mathbf{F}_1^{ext} \sim \zeta_c \epsilon^{-1} \mathbf{v}_1 + O(\ln(\epsilon)), \tag{2.4}$$

$\zeta_c = 3\pi\eta d_c$ is the colloidal drag coefficient. We calculated $\mathbf{F}_1^{ext} \approx 0.39\text{pN}/\mu\text{m/s}$ and find that experimentally, the bare particles is to within order of magnitude of the Reynolds prediction. The overestimation of the theoretical result may be attributed to neglecting the higher-order corrections to the hydrodynamic force between approaching spheres with and without rotations. By balancing the lubrication force with the optical tweezer force, we predict a short and constant relaxation time $\tau_{SLB} = 3\pi\eta d_c^2/(2\kappa_t(H - d_c)) \approx 1\text{s}$, in agreement with our experimental observations (Fig. 2.5b).

Effect of end-grafted F-actin on hydrodynamic resistance

The addition of F-actin on the lipid bilayer surface increases the hydrodynamic resistance to solvent flow during bead approach (Fig. 2.6). We rationalize this enhancement in the observed resistance by considering the increased viscous dissipation inside the polymer layer. Whereas the solvent flows unimpeded out of the interfacial volume for two bare beads, introducing the polymer layers sets up a locally porous medium that inhibits fluid flow. However, because increasing the surface density of F-actin corresponded to a larger interparticle separation at closest approach, the peak force measurements were not taken at small gap separations and straightforward application of lubrication theory will not demonstrate agreement with the experimental data. Should the gap separation be consistent with the compression of the end-grafted F-actin layers, we may refer to existing theories for a prediction of the hydrodynamic force.

Viscous flows through porous media are typically modeled using the Brinkman equation which accounts for the medium permeability by introducing a source term to the Stokes equations.[43] Fredrickson and Pincus applied a lubrication-type analysis of the Brinkman equation to determine the hydrodynamic force between two grafted polymer surfaces.[44] Modelling the local structure within the thin-gap as a semi-dilute polymer solution, they determined the permeability in terms of the equilibrium mean separation

between chains and its dependence on gap separation (i.e., ϵ). While this hydrodynamic force scales as $F^{\mathrm{H}} \sim \epsilon^{-\frac{1}{2}}$, a weaker dependence on the geometric aspect ratio than in the Reynolds result, the magnitude of the lubrication force is enhanced through incorporation of a polymer hydrodynamic screening length, ξ_{H}. This enhancement is consistent with the intuition that the polymer layer impedes fluid flow and is qualitatively observed through surface force measurements.[45, 36] Such an analysis would be valid on the nonequilibrium process timescales which are slower than that of F-actin reorganization, so that the grafted layer behaves as a "static" mesh whose structure is unperturbed by fluid flow. Otherwise, one would have to self-consistently solve the Stokes equations with a model for the body force that couples to the polymer dynamics [46, 47], which we will leave to future work.

2.5 Discussion

In this paper, we have demonstrated that functionalizing colloidal surfaces with laterally-mobile, end-grafted polymers generates a dynamic pair force which relaxes as a function of colloidal contact times. We observe that timescales of nonequilibrium processes driving colloids into contact non-trivially compete with the timescale of polymer brush reorganization away from the contact interface. Previous work has shown that F-actin in concentrated systems becomes rotationally immobile due to entanglement and hinderance by neighboring filaments.[48] At the surface concentrations probed in our study, the average distance between grafting sites is 10-20nm, versus the actin lengths of $O(\mu\mathrm{m})$). We do not expect surface-bound F-actin to pivot significantly about its anchoring point and relax through rotating away from the contact interface. We believe that slight deformations in the underlying lipid membrane by anchoring sites also cannot enable rotational mobility across the micrometer length scales of the contact interface.[49,

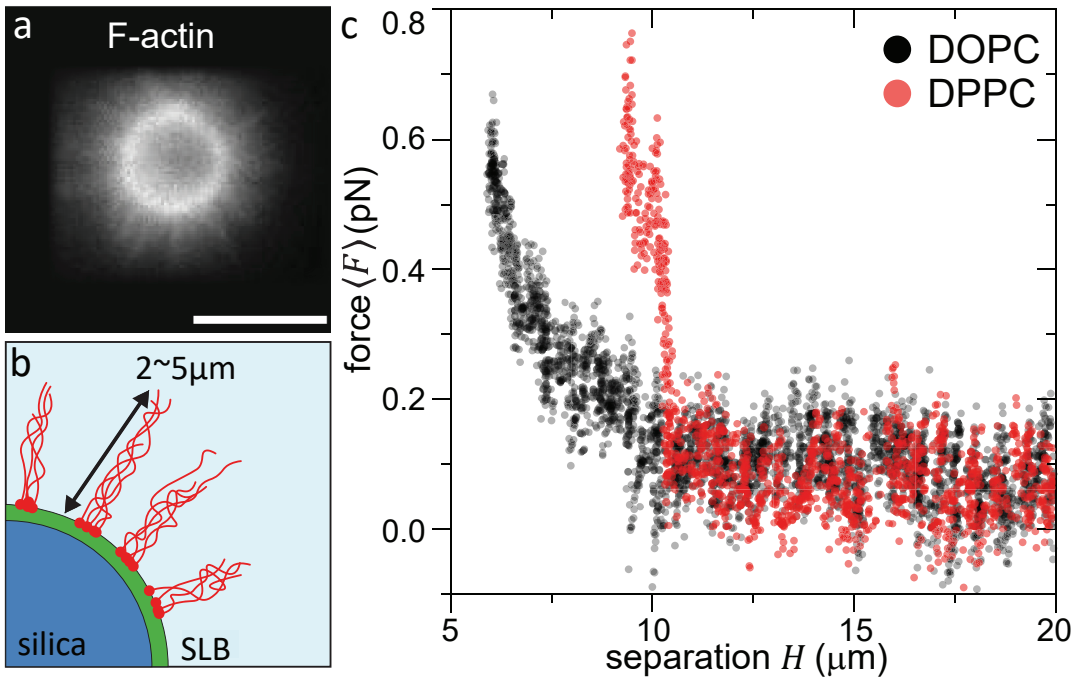

Figure 2.7: Less-mobile surface-grafted F-actin spontaneously organizes into rigid bundles, inducing steep and repulsive interactions which buckle when colloids are brought together. (a) Fluorescence image of end-grafted F-actin bundles coating the colloid whose SLB contains DPPC lipids and 10% DGS-NTA(Ni). All scale bars are 5μm. (b) Schematic of bundled F-actin with a mean bundle length 2μm, whose grafting sites are immobile, non-rotating, and phase-separated on the SLB surface. (c) Effective force changing in colloidal separation H when actin-coated colloids approach at 0.5μm/s. F-actin anchored to less-mobile DPPC SLB (red) mediates sharp force increases and buckling near $H = 10\mu$m, in contrast to monotonic repulsion when anchored to the more-mobile DOPC SLB (black).

50, 51] Additional effects that can influence the net interaction include frictional forces between adsorbed polymer layers,[52, 53, 54, 55] underlying lipid-membrane deformations due to anchoring proteins,[49, 51, 50] and fluid-mediated forces within polymer layers.[56, 44, 47] While a more accurate model that accounts for these interactions is left to future work, we have obtained proficient agreement between our Smoluchowski theory with BD simulations and OT experiments. We believe our simple framework captures the essential nonequilibrium physics of polymer-mediated forces and relaxation at colloidal contacts.

We conclude this work by observing that surface chemistry and composition may be

leveraged to engineer different types of contact-time dependent interactions. As a demonstration, we synthesize F-actin-coated colloids whose bilayers contain 1,2-dipalmitoyl-sn-glycero-3-phosphocholine (DPPC), which forms more rigid membranes compared to DOPC lipids.[57] Interestingly, the DPPC membrane organizes F-actin into rigid, protruding bundles with immobile and non-rotating grafting sites (Fig. 2.7a,b, Supp. Video 8). We surmise that micro-phase separation on the bead surface [58] induces gelsolin to form small patches, thereby organizing F-actin into bundles.

In Fig. 2.7c, we perform OT experiments to compare the effective colloidal force between DOPC and DPPC membrane conditions as a function of colloidal separation at a fixed approach speed (0.5μm/s). Unlike DOPC colloids, we observed sharp force increases and buckling when F-actin bundles on DPPC colloids begin to overlap, $H = 10\mu$m (Fig. 2.7c). Unlike the DOPC systems, the force profiles associated with F-actin on DPPC colloids do not demonstrate significant relaxation at velocities between $v = 0.5 - 10\mu\text{m}/s$. We hypothesize that the surface diffusion of F-actin on DPPC bilayers is significantly impeded by stiff bundle formation. Mechanistic understanding of the force transmission between bundle-forming F-actin layers is left for future work.

More generally, our conceptual framework of contact-time dependent interactions is applicable to systems beyond pair interactions of lipid-coated particles. For example, the interactions of a third colloid to a dimer would depend on surface rearrangement of mobile species. By extending to N-particle interactions, we can engineer the kinetics and morphology of multi-body assemblies. Our framework is also applicable to multi-component interfaces with adhesive linkers and repulsive brushes, analogous to ligand-receptor binding at crowded cell-cell junctions, and allows us to dynamic tune between repulsive and attractive interactions. More recently, explicit considerations of surface-mobile binding sites and their binding dynamics has been shown to influence colloidal self-assembly.[59, 60] Understanding contact-time dependent pair interactions may assist

the programmable design of higher-order structures in similar systems. The timescale competition between hydrodynamic shear and dynamic pair interactions may also impact particle suspension rheology.[61] Finally, our framework may help understand other complex dynamic interfaces such as surfactant-laden emulsions,[62, 63] colloids coated by polymers with adsorption and desorption rates,[64, 65] cell surfaces where proteins undergo lateral rearrangement upon cell-cell contact,[17] and uptake of macromolecules on membranes with characteristic wrapping times.[66]

2.6 Supplemental

2.6.1 Theoretical framework and simulations

In this section, we model nonequilibrium distribution of polymers with laterally-mobile grafting sites on the surface of two colloids when they are brought into contact. We consider their probability distribution through a Smoluchowski equation and model the relaxation of interfacial polymers via monomer diffusion. Finally, we calculate the instantaneous, polymer-mediated force exerted between the colloidal pair at close contact.

Smoluchowski Equation

We consider two colloids of size d_c in a Newtonian fluid with viscosity η, where one is located at the origin and the other at relative position $\mathbf{r}$. The colloidal surfaces are each coated by semi-rigid polymer brushes of polymerization M and surface density n_ρ that are able to diffuse laterally across the surfaces. The conditional probability distribution $P_N(\mathbf{h}_1, ..., \mathbf{h}_N, t; \mathbf{r})$ of finding N monomer particles at relative position $\mathbf{h}_1, ..., \mathbf{h}_N$ for a given colloidal separation $\mathbf{r}$ satisfies the time and space-dependent Smoluchowski

equation:

$$\frac{\partial P_N}{\partial t} + \sum_{i=1}^{N} \nabla_i \cdot \mathbf{j}_i = 0 \tag{2.5}$$

with the flux of α given by:

$$\mathbf{j}_i = -\sum_{j=1}^{N} \mathbf{D}_{ij} P_N \cdot \nabla_j \left(\ln P_N + \frac{V_{\text{tot}}}{k_{\text{B}}T} \right) \tag{2.6}$$

where $V_{\text{tot}}(\mathbf{h}_1, ..., \mathbf{h}_N; \mathbf{r})$ is the total potential energy, and $\mathbf{D}_{ij}$ is the diffusivity. In the absence of hydrodynamic interactions, the monomer diffusivity follows the Stokes-Einstein-Sutherland relation $\mathbf{D}_{ij} = \mathbf{I}_{ij} k_{\text{B}}T/\zeta_i$.

Eq. 2.5 is integrated over N-1 monomer degrees of freedom to recover Eq.(1) - (2) in the main text. In doing so, we have neglected higher order moments that, in general, involve expanding the conditional probability by fixing more particles in place, similar to a BBGKY hierarchy.[67] Such a closure is valid when the monomers are semidilute, is which generally taken to be at volume fractions under 30%.[68] The governing equation satisfies monomer mass conservation $\int \rho d\mathbf{h} = 1$ and no flux at colloid-monomer contact. Note that the total potential energy is replaced with a mean-field potential V which accounts for interactions between the monomer and the two colloids. We next discuss the polymer brush model used to approximate V.

Particle Interactions

The equilibrium monomer number density at position z above the surface in a polymer brush is approximated as a smooth, gaussian profile:

$$n_{\text{eq}}(z) \approx n_\rho e^{-(z^2 - h_0^2)/h_0^2} \tag{2.7}$$

where h_0 is the mean brush height. Beyond $z = h_0$, the monomer is heavily penalized by the entropic elasticity of the polymer chain. Note that $h_0 \sim 9\mu$m is set using the simulations.

From the equilibrium monomer distribution, the mean field pair potential between the monomer and the reference colloid can be defined as

$$V_{\text{single colloid}}(z) = -k_{\text{B}}T\ln(n_{\text{eq}}(z)/n_{\text{eq}}(0)). \tag{2.8}$$

We now approximate the potential of the monomer around two colloidal particles by summing the Boltzmann distributions of the monomers around each colloid at equilibrium:

$$V = -\ln(n_{\text{eq}}(||\mathbf{h}||) + n_{\text{eq}}(||\mathbf{h}-\mathbf{r}||)) \tag{2.9}$$

Under this definition, we recover the equilibrium distributions of polymer density around both colloids when in the limit of non-overlapping brushes, $H \gg 2h_0 + 2d_{\text{c}}$. We further note that the intrinsic hard sphere collisions between colloids and monomers $V_{\text{HS}} = \Theta(||\mathbf{h}||)+\Theta(||\mathbf{h}-\mathbf{r}||)$ do not explicitly enter into the potential but is instead incorporated as the no flux boundaries discussed previously.

Given the pair interaction potential V, the effective polymer mediated force on the reference colloid directly follows as $\langle\mathbf{F}\rangle = n_\rho M \int \rho\nabla_{\mathbf{r}} V d\mathbf{h} + n_\rho M \oint \rho\mathbf{n}_1 dS_1$, where the first term is the elastic force and the second term represents the osmotic force resulting from increased hard sphere collisions at contact. We define $F = \mathbf{F}\cdot\mathbf{e}_{\mathbf{x}}$ as the force magnitude along the colloidal line of centers. At equilibrium, this polymer mediated force is weaker than the potential derived by Dolan and Edwards for compressed polymer brushes whose grafting sites are immobile [34] because (1) our model neglects forces resulting from chain compression and (2) laterally-mobile polymers can exclude from the contact interface.

Colloid Approach Speed

Up until now, we have defined an evolution equation for the monomer when colloidal particles are fixed in space, governed by thermal diffusion and interparticle forces. In order to consider the nonequilibrium dynamics as the colloidal system relaxes, we require an appropriate nonequilibrium starting configuration of monomer density ρ. We hypothesize the starting monomer configuration is modulated by the speed at which colloids are brought into contact. The interfacial concentration of monomers on opposing colloidal surfaces should increase proportionally to the speed at which colloids are compressed, $\rho \sim \mathrm{Pe}\rho_{\mathrm{eq}}$, where we have defined a Péclet number $\mathrm{Pe} = v\sigma/D_\rho$ for the relative timescale for colloids to compress the polymer brushes versus the diffusive motion of the monomers. Note that $\rho(\mathbf{h}, t = 0|\mathbf{r})$ is normalized to satisfy mass conservation over all $\mathbf{h}$.

Fluid-Mediated Effects between Colloidal Particles

To determine the hydrodynamic force in the friction-dominated limit, one must solve the Stokes equations in the incompressible solvent

$$\nabla^2\mathbf{u} - \boldsymbol{\nabla}p = \mathbf{f}, \tag{2.10}$$

$$\boldsymbol{\nabla}\cdot\mathbf{u} = 0, \tag{2.11}$$

where the local velocity field $\mathbf{u}$ is driven by any combination of moving boundaries (e.g., the beads in motion), dynamic pressure gradients $\boldsymbol{\nabla}p$, or body forces $\mathbf{f}$. As the Stokes equations are linear in velocity, so, too, are the hydrodynamic forces. That is, $F^{\mathrm{H}} \sim \zeta_{\mathrm{c}}v$, where ζ_{c} is a drag coefficient. For an isolated, translating sphere, this relationship is Stokes' law, $F^{\mathrm{H}} = -3\pi\eta d_{\mathrm{c}}v$. However, the form of ζ_c becomes increasingly complicated in the presence of nearby particles, as their rigid boundaries interfere with the long-ranged flow disturbances induced by any one bead. Then, the total hydrodynamic force

and torque on a bead is a linear combination of all fluid-mediated resistances to particle translation and rotation.

2.6.2 Brownian Dynamics Simulations

Two colloids of size $d_{\mathrm{c}} = 4\sigma$ in a solvent of viscosity η are coated by standard Kremer-Grest bead-spring polymers [25]. The simulation length scale is $\sigma = 1\mu$m and the dimensions of the periodic simulation box are $L_{\mathrm{y}} = L_{\mathrm{z}} = 33\sigma, L_{\mathrm{x}} = 65\sigma$. We coarse-grain polymer segments into beads of diameter $d_\rho = 0.8\mu$m with 17 beads per chain. Results shown in Fig. 3 of the main text are obtained for a surface coverage $\phi = n_\rho(d_\rho^2/4d_{\mathrm{c}}^2) = 0.15$. To accurately model F-actin and compare with experimental results in Fig. 5, we choose surface coverages of $\phi = 0.15 - 0.43$ to match actin surface-densities of $\phi_{\text{F-actin}} = \pi(d_{\text{F-actin}}/2)^2\rho_{\text{F-actin}} \approx 0.11 - 0.46$ where the F-actin monomer size is $d_{\text{F-actin}} = 7$nm (see Supp. Video 3). For all simulations, we choose a time step size $\Delta t = (2 \times 10^{-}5)(\sigma^2/D_\rho)$ and sample the simulation every 10^3 time steps. We simulate 600-2000 coarse-grained polymer beads for 20-30 independent realizations to obtain representative statistics of the nonequilibrium approach and relaxation processes. Due to the coarse-graining of polymer segments as beads of diameter d_ρ, our simulation results capture relaxation beyond the Brownian timescale of the bead $t \sim d_\rho^2/D_\rho$ and does not account for fluctuations at smaller length and timescales. Simulations are performed using HOOMD-Blue, a GPU-accelerated simulation package.

Recognizing that the momentum relaxation timescale is much faster than the diffusive timescale in our system, the trajectory of each polymer bead in time t follows the overdamped Langevin equation of motion:

$$\frac{\Delta \mathbf{x}_i}{\Delta t} = (\underbrace{\mathbf{F}_i^{\mathrm{P}}}_{\text{interactions}} + \underbrace{\mathbf{F}_i^{\mathrm{R}}}_{\text{Brownian}})/\zeta \tag{2.12}$$

where $\mathbf{x}_i$ is the position of particle i, and $\zeta = 3\pi\eta d_\rho$ is the drag coefficient. Note that the Stokes-Einstein-Sutherland diffusivity of the polymer bead is defined as $D_\rho = k_\mathrm{B}T/\zeta$. In accordance with fluctuation dissipation, the implicit solvent induces a stochastic force satisfying $\langle \mathbf{F}_i^\mathrm{B} \rangle = 0$ and $\langle \mathbf{F}_i^\mathrm{B}(0)\mathbf{F}_i^\mathrm{B}(t) \rangle = 2k_\mathrm{B}T(\zeta_i)\mathbf{I}\delta(t)$. Unlike the polymer beads which undergo stochastic motion, the colloidal cores either move with deterministic motion towards each other at some fixed speed (during the approach step) or are fixed in space and cannot undergo any translation (during the relaxation step).

Particle interactions

All non-bonded particle pairs interact through a Weeks-Chandler-Anderson (WCA) hard sphere-like potential with parameters $\epsilon = \alpha = k_\mathrm{B}T$. Adjacent polymer beads in a chain to interact through a Finite-Extensible-Nonlinear-Elastic (FENE) potential with equilibrium bond parameter $r_0 = 1.5\sigma$ and attraction strength $k_\mathrm{FENE} = 30k_\mathrm{B}T$. Additionally, we employ a harmonic potential penalizing the angle θ between two adjacent bonds, $V_\mathrm{ang} = (1 - cos(\theta - \pi))l_\rho/\sigma$ where the persistence length is $l_\rho = 13\sigma$. To graft polymers onto the colloidal surface, we constrain the bead corresponding to the polymer grafting site between two, concentric spherical walls, such that the grafting site may still translate laterally but cannot detach from the surface.

Approach protocol

At the start of the simulation, polymer chains are first allowed to equilibrate at an initial colloidal separation $H = 30\sigma$ where the brushes are non-overlapping. During the approach process, colloid and polymer bead positions are incrementally updated to move closer by $\Delta H_\mathrm{increm} = 0.005\sigma - 0.08\sigma$ every $\Delta t_\mathrm{increm} = 10^2 - 10^3$ time steps to bring colloids together to different separation distances $30\sigma < H < d_\mathrm{c}$ (see Supp. video 1). ΔH and t_increm are adjusted to fix the colloid approach velocity v (see Supp. video

2). Finally, polymers are allowed to relax from their nonequilibrium configurations for $10^6 - 10^7$ time steps as colloids are held fixed at separation H. During the approach and relaxation steps, the polymer-mediated force on the colloids $\langle F \rangle = \sum_i F_i^P$ is computed every $10^2 - 10^3$ time steps.

2.6.3 Experimental methods

The main text already contains a description of our experimental methods; in this section, we provide additional experimental detail on optical tweezer set-up and particle fabrication.

Optical laser tweezers setup

Colloidal particles were manipulated using optical laser tweezers (Tweez 305, Aresis Ltd, Slovenia) with a continuous infrared laser (wavelength: 1064nm, maximum power: 5W) equipped on an inverted fluorescence microscope (Ti2-Eclipse, Nikon) using oil immersion Apo 100x objective lens (Numerical Aperture(NA) 1.45, Nikon). As an excitation light source, Lumencor SpectraX Multi-Line LED Light Source (Lumencor, Inc) was used at two different wavelengths (488nm and 647nm). A multi-wave emission filter (515/30, 680/42; Semrock, IDEX Health and Science) spectrally filtered the fluorescent lights. Videos were acquired by CMOS camera, (Photometrics Prime 95, Teledyne Photometrics) with 100 frames per second(fps) for force measurements, and 15 fps for other videos. CMOS and microscope were operated using Micromanager 1.4 on ImageJ. Trap positions were regulated by importing time-trajectory Matlab scripts to Tweez 305 software with 25mW/particle as a set value, not a measured power on the objective.

Preparation of observation cell

The observation cell described in main text Fig. 2a was constructed on a 170±5μm thickness high precision coverslip (Marienfeld) as a glass substrate, with a 5mm thick Polydimethylsiloxane (PDMS, Sylgard 184, Dow), with a 6mm hole as a wall on the glass substrate. To prevent colloids from sticking to the glass substrate, the observation cell was coated with Poly(l-lysine)-graft-5k poly(ethylene glycol) (PLL-g-PEG, Nanosoft BIotechnology LCC.)[**turlier2016equilibrium**]. The passivation coating on the glass was treated by spreading 30μL of 0.1 mg/mL PLL-g-PEG aqueous solution to piranha-cleaned glasses. After 30 min, the treatment solution was discarded from the cell. The remaining unbound PLL-g-PEG was washed by pipetting fresh Milli-Q (MQ) water vigorously. This washing process was repeated more than 5 times using fresh MQ water for every washing cycle.

Preparation of F-actin grafted colloid

Colloids coated with surface-mobile polymer were fabricated by grafting filamentous actin (F-actin) on supported lipid bilayer (SLB) coated silica microbeads (Fig. 2b-d, Fig. 7a-b). 4μm diameter silica microbeads, $d_c = 4\mu$m, were purchased from Bangs Laboratories and cleaned by piranha solution, a 3:2 mixture of sulfuric acid and hydrogen peroxide, through bath sonicatation for 30 min. Then, the cleaned bead slurry was washed with MQ water by re-dispersing and sedimenting using a centrifuge, 10,000 x g for 3min. Chemicals used in this experiment were purchased from Sigma-Aldrich if there are no notations.

	Lipids			
Sample name	DGS-NTA(Ni) [%]	DOPC [%]	DPPC [%]	DOPE-Atto488 [%]
10% Ni-NTA	10	89	-	1
1% Ni-NTA	1	98	-	1
SLB only	0	99	-	1
DPPC	10	-	89	1

Table 2.1: Compositions of lipid for each SUV sample

Small unilamellar vesicle (SUV) synthesis

To modify the surface properties (i.e. actin density, and mobility), small unilamellar vesicles (SUVs) were designed for each experiment. We perform tip-sonication to form SUVs from the lipid solution [**barakat2023enhanced**]. Lipids 1,2-dioleoyl-sn-glycero-3-phos-phocholine (DOPC), 1,2-dipalmitoyl-sn-glycero-3-phosphocholine (DPPC), and 1,2-dioleoyl-sn-glycero-3-[(N-(5-amino-1- carboxypentyl)iminodiacetic acid)succinyl] (DGS-NTA(Ni), Ni-NTA), were purchased from Avanti Polar Lipids. A fluorescence lipid, Atto 488-1,2-dioleoyl-sn-glycero-3-phosphoethanolamine (DOPE-Atto488), was purchased from ATTO-TEC GmbH. Lipid solutions were mixed at specific molecular ratios in a disposable glass culture tube. All residual solvents were evaporated from the solution using a vacuum chamber for 30min. After 30min, the dried lipid film was rehydrated in MQ water to 0.2mg/mL for 10min. Before tip sonication, the rehydrated solution was vortexed and transferred to a 1.5mL tube. The solution was then sonicated for 3min (1s/2s, on/off cycle) with a 20% of the maximum power of a tip-sonicator (Branson SFX250 Sonifier). Finally, 10x MOPS buffer was added to balance the osmotic pressure across the SLB, with a final concentration of 50mM MOPS pH 7.4 and 100mM NaCl. The compositions of SUVs for corresponding samples are described in Table 2.1.

Formation of supported lipid bilayer (SLB) on silica beads

The SLB was formed on glass beads by incubating 10μL of silica particle solution and an excess amount (50μL) of composition-controlled SUVs solution for 15 minutes at room temperature. To fabricate DPPC-containing SLB, we melt DPPC lipids in a convection oven at 40°C in a convection oven for 2min. Free SUVs were washed with HEPES buffer (50mM HEPES pH 7.4, 100mM NaCl) by gently removing the supernatant and adding fresh HEPES buffer without disturbing the lipid-coated particle sediment. During the last two washes, F-buffer was used instead of HEPES to exchange the buffer conditions for the next step. The F-buffer composition is 50mM Tris pH 7.5, 2mM $MgCl_2$, 0.2mM $CaCl_2$, 25mM KCl, 0.5mM adenosine 5'-triphosphate (ATP), and 1mM dithiothreitol (DTT).

Grafting F-actin on SLB

We polymerized F-actin directly on the SLB-coated silica bead described in main text (Fig. 2b, Fig. 7b). SLB-coated beads, 100nM 6x-histidine tagged gelsolin (6x-His-Gel, HPG6, Cytoskeleton, Inc.), 20μM monomeric actin (G-actin, purified by following the method with modification [**spudich1971regulation**]), 18μM phalloidin(Invitrogen), and 2μM 647-dyed phalloidin(Alexa Fluor Plus 647 Phalloidin, Invitrogen) were added to F-buffer in the following steps. We first mix 6x-His-Gel with SLB-coated particles and then wait for 2 min for Histidine-Nickel binding to occur. The Histidine of 6x-His-Gel is directly anchored to the Ni^+-site of DGS-NTA(Ni) on the SLB, and Gelsolin grabs onto the end of F-actin. After 45min, the polymerization reaction was quenched by diluting the solution concentration 20 times using HEPES buffer. We gently pipetted to mix the solution because F-actin is fragile to breaking. After waiting 15min for particle sedimentation, unreacted reactants were washed without resuspending the particle sediment

by discarding the supernatant through gentle pipetting. Fresh HEPES buffer was then injected. The actin-grafted beads were used after repeating the washing process more than 5 times.

Characterization of grafting actin density

To obtain the surface density of F-actin on the SLB at various DGS-NTA(Ni) concentrations, we compare against standard fluorescence beads (Quantum Alexa Fluor 647 MESF, Bangs Laboratories), which have precise sizes and known numbers of fluorescent dyes on the surface. The dye densities on reference beads are calculated by dividing the number of dyes by the surface area, $\rho_{\mathrm{dye,\ ref}} = \frac{N_{\mathrm{dye}}}{4\pi R^2}$. To construct a calibration line, the standard beads were dispersed in the 8-well chambered coverglass system ($170\pm5\mu$m, Cellvis) and imaged with constant camera values, 16-bit depth, 500ms of exposure time, and 10% of maximum power (wavelength centered at: 647nm).

From the images, the maximum brightness of the particles was plotted against surface number density of the dye (Fig. S2.8). We perform a linear regression, $I = \alpha \cdot \rho_{\mathrm{dye}} + I_0$, using 5 different standard beads, where I is an intensity of fluorescence signal, α is the slope of the linear fit, ρ_{dye} is a number density of the dye [dyes/μm^2], and I_0 is the background noise of the fluorescence image. Actin-grafted colloids were prepared with a logarithmic scale of DGS-NTA(Ni) concentration in the SLB (0.01, 0.1, 1, and 10%). The fluorescence intensity of F-actin grafting samples was measured from 647 nm existing fluorescence images with the same conditions as standard beads. Number densities of the dye were then converted to F-actin grafting densities by multiplying the molar ratio of total phalloidin to dyed phalloidin, $N_{\mathrm{total}}/N_{\mathrm{dyed}} = 10$, since binding one G-actin to the filament requires one phalloidin for stabilization[**dancker1975interaction**].

Surface grafting densities on reference beads were $\rho_{\mathrm{dye,\ ref}}$; 0-3,441 dyes/$\mu$m^2 (Fig. S2.8). The linear regression parameters are, $\alpha = 4.6\mu\mathrm{m}^2$, $I_0 = 135.5$. The brightness of

fabricated actin grafting beads was also measured with 5 different logarithmic scale DGS-NTA(Ni) concentrations. From the measured intensities, the dye densities were derived using the following equation, $\rho_{\text{F-actin}} = \frac{N_{\text{total}}}{N_{\text{dyed}}}\rho_{\text{dye}} = 10(I - I_0)/\alpha$. So, the number densities of F-actin are $\rho_{\text{F-actin, 10\%}} = 12,293 \pm 1,030$ filaments/μm^2, $\rho_{\text{F-actin, 1\%}} = 3,211 \pm 568$ filaments/μm^2. We hypothesize one reason why the actin surface density does not increase linearly with DGS-NTA(Ni) concentration is because short F-actin filaments tend to crowd the SLB surface at higher concentrations, preventing additional anchoring.

Characterization of grafting actin length

The length of grafting F-actin on the 10% Ni-NTA membrane was measured from high-contrast fluorescence images. Images and videos were acquired by 50ms of exposure time, 10% of 647nm excitation laser powers. The range of F-actin length was roughly 2-20μm with a mean of 5μm. (Fig. S 2.9, and Supp. Video 4) We note that the dimness of the long filaments is attributed to rapid photo-bleaching by the laser. The DPPC membrane has a different length distribution of 2-5μm with a mean of 3μm. (Fig. 7a, and Supp. Video 7)

Force measurement

As outlined in the main text, force measurements between two colloids were conducted over an approach process followed by relaxation. (Fig. 2e, Supp. Video 5, 6) The two traps are initialized at long separation, 35μm, where opposing F-actin filaments are non-interacting. The left particle is held at a stationary trapping position to measure forces while the right particle moves towards the stationary colloid with a constant speed during the approach process ($t < 0$). At $t = 0$, the moving trap has held a position and immediately started a relaxation process. Time-position data was imported from Matlab

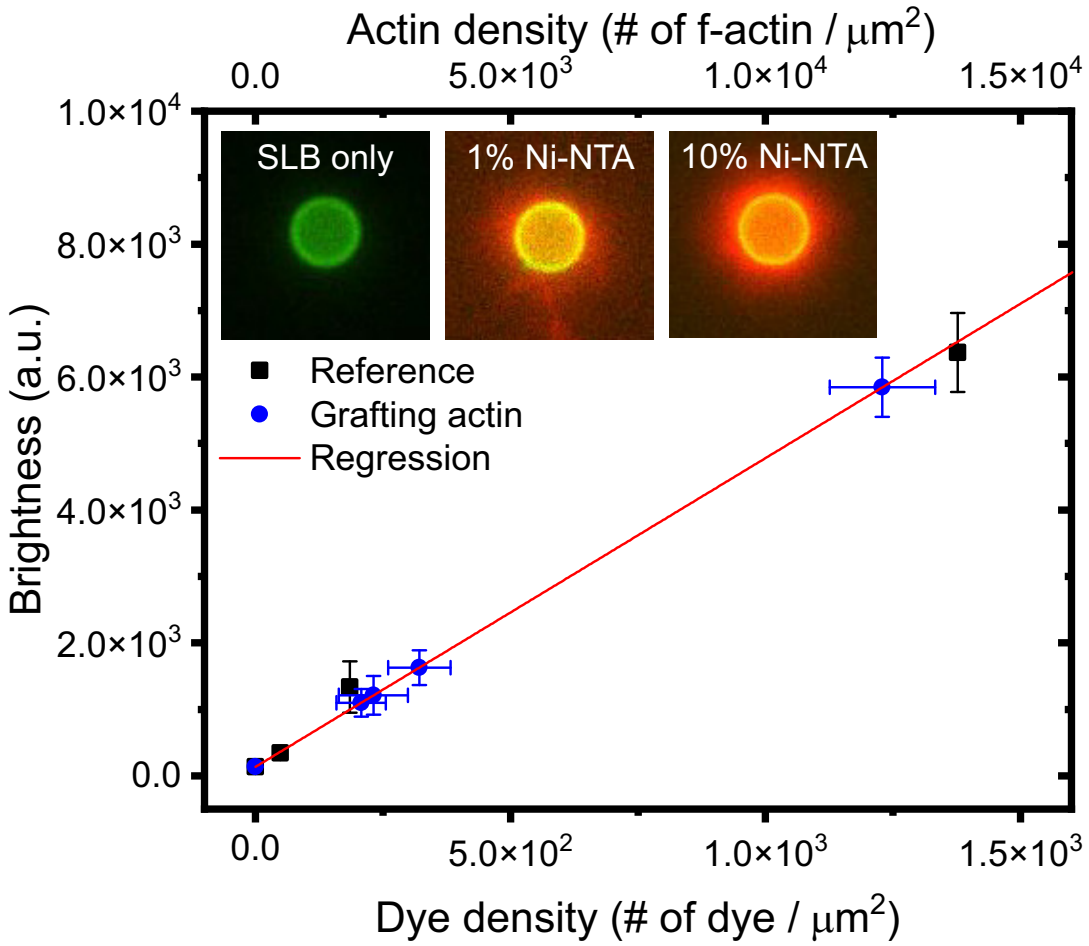

Figure 2.8: Brightness changing in the dye density of standard particles and surface grafted actin. Inset images are corresponding pictures that have 0, 1, and 10% DGS-NTA(Ni) lipids on SLB. Red and green colors in the inset images are represented by F-actin and SLB respectively. Black squares are representing the fluorescence intensity of reference beads. The red line is the linear regression fit of the standard beads. The blue circles are measured data of the fabricated actin grafted colloids.

to Tweeze 305 software. We measured dynamic interactions for 5 different approach speeds, 0.5, 1, 2, 5, and 10μm/s. Forces were calculated from the following equation, $F = \kappa_t \cdot dx$, where κ_t is a trap stiffness of the optical trap, and dx is a particle displacement from the trapping focus. During force measurements, photo-bleaching was suppressed by adding an oxygen scavenger into the medium. The oxygen-removing solution consists of 600nM of glucose oxidase from Aspergillus niger, 30nM of catalase from bovine liver, and

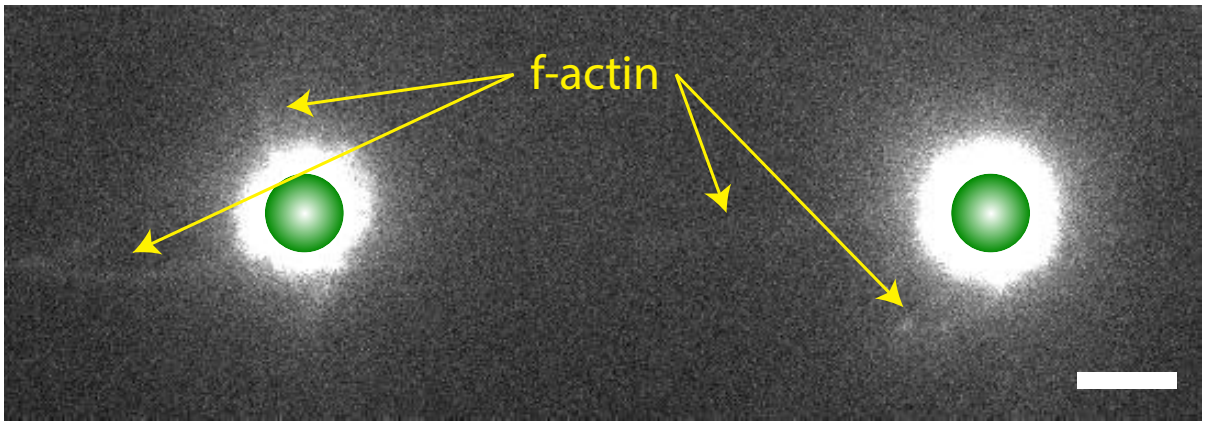

Figure 2.9: Fluorescence image of long actin filaments grafted on the 1% DGS-NTA(Ni) SLB by increasing brightness and contrast. The scale bar is 5 μm. See also Supp. Video 4.

10mM glucose.

Calibration of trap stiffness

To compute the trap stiffness κ_{t}, we note that F-actin surface concentration influenced the thermal vibrations of the stationary trap. To account for this, we constract a probability distribution from more than 4,000 positions of the trapped bead. The radial displacement, dr, from the laser focus was then fit with Boltzmann distribution, $P(dr) = \frac{\kappa_{\mathrm{t}}}{2\pi}\exp(-\kappa_{\mathrm{t}} dr^2/2k_{\mathrm{B}}T)$. From the probability distribution curve, we obtained a range of trap stiffness, $\kappa_{\mathrm{t}} : 0.5 - 0.7pN/\mu$m.

Defining equilibrium state

To characterize the force relaxation as the system approaches equilibrium, we define a relaxation time τ_{R} for the peak force to decay 90% toward the equilibrium value (Fig. 4). In other words, $F(t = \tau_{\mathrm{R}}) = F_{\mathrm{max}} - 0.9(F_{\mathrm{max}} - F_{\mathrm{eq}})$, where F_{max} is a maximum peak force at $t = 0$, and F_{eq} is the equilibrium force at long times, $t \gg \tau_{\mathrm{R}}$. The equilibrium force is calculated by averaging over the range 15sec $< t <$ 20sec when the force has

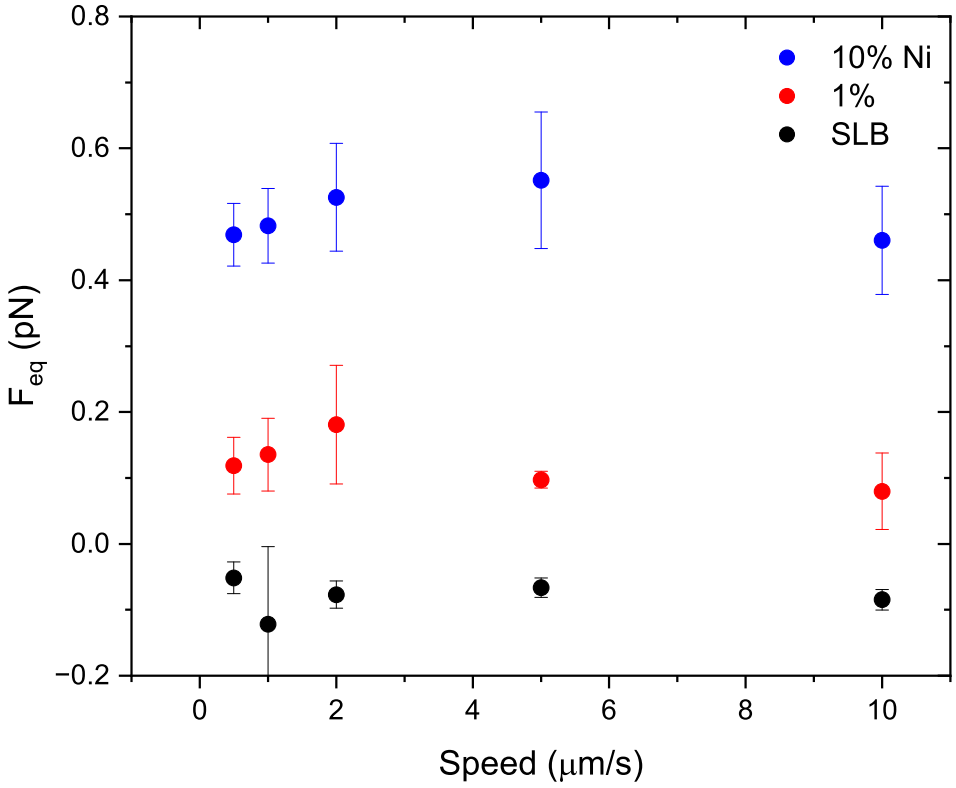

Figure 2.10: Measured equilibrium forces, F_{eq}, after finishing relaxation processes, $t > \tau_{\mathrm{R}}$. 10% Ni-NTA, 1% Ni-NTA, and SLB only are corresponding to blue, red, and black circles. The particle having the same grafting density makes similar equilibrium forces, not depending on the approach process.

fully decayed. We observe that the equilibrium force is independent of approach speed and increases for higher F-actin surface densities (Fig. S2.10). We note that SLB-only colloids have negative forces because of van-der Waals type attractions.

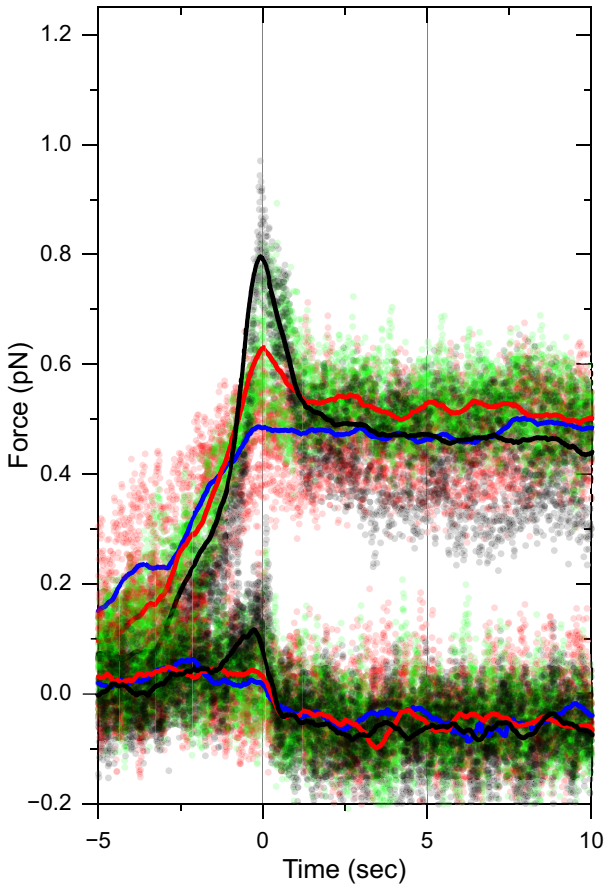

Figure 2.11: F-actin grafted on lipid bilayer-coated silica colloids generates contact–time dependent interactions between colloids. Plot shows force as a function of time on beads with F-actin surface density $n_{\text{actin}} \approx 12,000/\mu\text{m}^2$ (top curves) and a separate measurement for bilayer-only control (bottom curves). Solid lines are time-average curves with approach speeds of 0.5 μm/s (blue), 2μm/s (red), and 10μm/s (black), averaged over five pairs. Dots are corresponding original data Times $t < 0$ correspond to the approach step and $t \geq 0$ represent times when the colloids are at close contact.

Bibliography

[1] W. B. Russel, D. A. Saville, and W. R. Schowalter. *Colloidal Dispersions*. Cambridge University Press, Dec. 1989.

[2] A. Paul Alivisatos et al. "Organization of 'nanocrystal molecules' using DNA". In: *Nature 1996 382:6592* 382.6592 (1996), pp. 609–611.

[3] P. J. Santos, T. C. Cheung, and R. J. Macfarlane. "Assembling Ordered Crystals with Disperse Building Blocks." In: *Nano Lett.* 19 (2019), pp. 5774–5780.

[4] Gang Chen et al. "Regioselective surface encoding of nanoparticles for programmable self-assembly". In: *Nature Materials* (2018).

[5] Chad A. Mirkin et al. "A DNA-based method for rationally assembling nanoparticles into macroscopic materials". In: *Nature 1996 382:6592* 382.6592 (1996), pp. 607–609.

[6] Paul L. Biancaniello, Anthony J. Kim, and John C. Crocker. "Colloidal Interactions and Self-Assembly Using DNA Hybridization". In: *Physical Review Letters* 5 (Feb. 2005), p. 058302.

[7] Pinar Akcora et al. "Anisotropic self assembly of spherical polymer grafted nanoparticles". In: *Nature Materials* 8.4 (Mar. 2009), pp. 354–359.

[8] Stefano Angioletti-Uberti, Bortolo M. Mognetti, and Daan Frenkel. "Theory and simulation of DNA-coated colloids: a guide for rational design". In: *Physical Chemistry Chemical Physics* 18.9 (Feb. 2016), pp. 6373–6393.

[9] Federica Loverso, Sergei A. Egorov, and Kurt Binder. "Interaction between polymer brush-coated spherical nanoparticles: Effect of solvent quality". In: *Macromolecules* 45.21 (Nov. 2012), pp. 8892–8902.

[10] S A Egorov. "Interactions between polymer brushes in solvents of variable quality: A density functional theory study". In: *Journal of Chemical Physics* 129.6 (2008), p. 64901.

[11] J Vermant and M J Solomon. "Flow-induced structure in colloidal suspensions". In: *Journal of Physics: Condensed Matter* 17.4 (Feb. 2005), R187–R216.

[12] P. Segrè et al. "Glasslike Kinetic Arrest at the Colloidal-Gelation Transition". In: *Physical Review Letters* 86.26 (June 2001), pp. 6042–6045.

[13] Francesco Bonacci et al. "Contact and macroscopic ageing in colloidal suspensions". In: *Nature Materials* 19.7 (July 2020), pp. 775–780.

[14] Francesco Bonacci et al. "Yield stress aging in attractive colloidal suspensions". In: *Physical Review Letters* 128.1 (2022), p. 018003.

[15] John R. Melrose and Robin C. Ball. "Continuous shear thickening transitions in model concentrated colloids—The role of interparticle forces". In: *Journal of Rheology* 48.5 (Sept. 2004), pp. 937–960.

[16] John R. Melrose and Robin C. Ball. ""Contact networks" in continuously shear thickening colloids". In: *Journal of Rheology* 48.5 (Sept. 2004), pp. 961–978.

[17] Monks CR et al. "Three-dimensional segregation of supramolecular activation clusters in T cells". In: *Nature* 395 (1998), pp. 82–86.

[18] Simon J. Davis and P. Anton van der Merwe. “The kinetic-segregation model: TCR triggering and beyond”. In: *Nature Immunology 2006 7:8* 7.8 (2006), pp. 803–809.

[19] Aditya S. Khair and John F. Brady. “On the motion of two particles translating with equal velocities through a colloidal dispersion”. In: *Proceedings of the Royal Society A: Mathematical, Physical and Engineering Sciences* 463.2077 (2007), pp. 223–240.

[20] J. Dzubiella, H. Löwen, and C. N. Likos. “Depletion Forces in Nonequilibrium”. In: *Physical Review Letters* 91.24 (Dec. 2003), p. 248301.

[21] Matthias Krüger and Markus Rauscher. “Colloid-colloid and colloid-wall interactions in driven suspensions”. In: *The Journal of Chemical Physics* 127.3 (July 2007), p. 034905.

[22] Benjamin E. Dolata and Roseanna N. Zia. “Non-equilibrium pair interactions in colloidalÂ dispersions”. In: *Journal of Fluid Mechanics* 836 (2018), pp. 694–739.

[23] Frédéric Hecht and F Hecht. “New development in freefem++”. In: *Journal of Numerical Mathematics* 20.0 (2012), pp. 1–14.

[24] Joshua A. Anderson, Jens Glaser, and Sharon C. Glotzer. “HOOMD-blue: A Python package for high-performance molecular dynamics and hard particle Monte Carlo simulations”. In: *Computational Materials Science* 173 (Feb. 2020), p. 109363.

[25] Kurt Kremer and Gary S Grest. “Dynamics of entangled linear polymer melts: A molecular-dynamics simulation”. In: *The Journal of Chemical Physics* 92.8 (1990), pp. 5057–5086.

[26] J. C. Crocker et al. “Entropic Attraction and Repulsion in Binary Colloids Probed with a Line Optical Tweezer”. In: *Physical Review Letters* 82.21 (May 1999), pp. 4352–4355.

[27] Edward T Castellana and Paul S Cremer. "Solid supported lipid bilayers: From biophysical studies to sensor design". In: *Surface Science Reports* 61.10 (2006), pp. 429–444.

[28] David Sept et al. "Annealing accounts for the length of actin filaments formed by spontaneous polymerization". In: *Biophysical journal* 77.6 (1999), pp. 2911–2919.

[29] Mireille MAE Claessens et al. "Actin-binding proteins sensitively mediate F-actin bundle stiffness". In: *Nature materials* 5.9 (2006), pp. 748–753.

[30] Coraline Brangbour et al. "Force-velocity measurements of a few growing actin filaments". In: *PLoS biology* 9.4 (2011), e1000613.

[31] James W. Swan et al. "Multi-scale kinetics of a field-directed colloidal phase transition". In: *Proceedings of the National Academy of Sciences* 109.40 (Oct. 2012), pp. 16023–16028.

[32] Zachary M. Sherman and James W. Swan. "Dynamic, Directed Self-Assembly of Nanoparticles via Toggled Interactions". In: *ACS Nano* 10.5 (2016), pp. 5260–5271.

[33] M. Tagliazucchi and I. Szleifer. "Dynamics of dissipative self-assembly of particles interacting through oscillatory forces". In: *Faraday Discussions* 186 (2016), pp. 399–418.

[34] A. K. Dolan and S. F. Edwards. "Theory of the stabilization of colloids by adsorbed polymer". In: *Proceedings of the Royal Society of London. A. Mathematical and Physical Sciences* 337.1611 (Apr. 1974), pp. 509–516.

[35] S. T. Milner. "Polymer Brushes". In: *Science* 251.4996 (Feb. 1991), pp. 905–914.

[36] Jacob N Israelachvili. *Intermolecular and surface forces*. Academic press, 2011.

[37] P A Janmey et al. “Structure and mobility of actin filaments as measured by quasielastic light scattering, viscometry, and electron microscopy.” In: *Journal of Biological Chemistry* 261.18 (June 1986), pp. 8357–8362.

[38] L. Gary Leal. *Advanced Transport Phenomena*. Cambridge University Press, June 2007.

[39] J Happel and H Brenner. *Low Reynolds number hydrodynamics: with special applications to particulate media*. en. Springer Science & Business Media, Dec. 2012.

[40] Osborne Reynolds. “Iv. on the theory of lubrication and its application to mr. Beauchamp Tower’s experiments, including an experimental determination of the viscosity of olive oil”. In: *Philosophical Transactions of the Royal Society of London* 177 (1886), pp. 157–234.

[41] D. J. Jeffrey. “Low-Reynolds-number flow between converging spheres”. In: *Mathematika* 29.1 (1982), pp. 58–66.

[42] M. E. O’Neill and K. Stewartson. “On the slow motion of a sphere parallel to a nearby plane wall”. In: *Journal of Fluid Mechanics* 27.4 (1967), pp. 705–724.

[43] H. C. Brinkman. “A calculation of the viscous force exerted by a flowing fluid on a dense swarm of particles”. In: *Flow, Turbulence and Combustion* 1.1 (Dec. 1949), pp. 23–34.

[44] Glenn H. Fredrickson and Philip Pincus. “”Squeezed Sponge””. In: *Langmuir* 7 (1991), pp. 786–795.

[45] Jacob Klein. “Forces between mica surfaces bearing adsorbed macromolecules in liquid media”. In: *Journal of the Chemical Society, Faraday Transactions 1: Physical Chemistry in Condensed Phases* 79.1 (1983), p. 99.

[46] Patrick S. Doyle, Eric S. Shaqfeh, and Alice P. Gast. "Rheology of polymer brushes: A Brownian dynamics study". In: *Macromolecules* 31.16 (1998), pp. 5474–5486.

[47] Patrick S. Doyle, Eric S. G. Shaqfeh, and Alice P. Gast. "Rheology of "Wet" Polymer Brushes via Brownian Dynamics Simulation: Steady vs Oscillatory Shear". In: *Phys. Rev. Lett.* 78 (6 Feb. 1997), pp. 1182–1185.

[48] William H. Sawyer et al. "Rotational Dynamics of Actin". In: *Biochemistry* 27.20 (Oct. 1988), pp. 7733–7740.

[49] Michael F. Brown. "Curvature forces in membrane lipid-protein interactions". In: *Biochemistry* 51.49 (Dec. 2012), pp. 9782–9795.

[50] Carlos D. Alas and Christoph A. Haselwandter. "Dependence of protein-induced lipid bilayer deformations on protein shape". In: *Physical Review E* 107.2 (Feb. 2023), p. 024403.

[51] Jérémie Rossy, Yuanqing Ma, and Katharina Gaus. "The organisation of the cell membrane: do proteins rule lipids?" In: *Current Opinion in Chemical Biology* 20 (June 2014), pp. 54–59.

[52] Daniel J. Beltran-Villegas, Tara D. Edwards, and Michael A. Bevan. "Self Consistent Colloidal Energy and Diffusivity Landscapes in Macromolecular Solutions". In: *Langmuir* 29.40 (Oct. 2013), pp. 12337–12341.

[53] Julia C. Swavola, Tara D. Edwards, and Michael A. Bevan. "Direct Measurement of Macromolecule-Coated Colloid–Mucus Interactions". In: *Langmuir* 31.33 (Aug. 2015), pp. 9076–9085.

[54] Romain Mari et al. "Shear thickening, frictionless and frictional rheologies in non-Brownian suspensions". In: *Journal of Rheology* 58.6 (2014), pp. 1693–1724.

[55] Neil Y. C. Lin et al. “Hydrodynamic and Contact Contributions to Continuous Shear Thickening in Colloidal Suspensions”. In: *Physical Review Letters* 115.22 (Nov. 2015), p. 228304.

[56] Jacob Klein et al. “Lubrication forces between surfaces bearing polymer brushes”. In: *Macromolecules* 26.21 (Oct. 1993), pp. 5552–5560.

[57] W. Rawicz et al. “Effect of Chain Length and Unsaturation on Elasticity of Lipid Bilayers”. In: *Biophysical Journal* 79.1 (July 2000), pp. 328–339.

[58] Dong Chen and Maria M Santore. “Three dimensional (temperature–tension–composition) phase map of mixed DOPC–DPPC vesicles: Two solid phases and a fluid phase coexist on three intersecting planes”. In: *Biochimica et Biophysica Acta (BBA)-Biomembranes* 1838.11 (2014), pp. 2788–2797.

[59] Angus McMullen et al. “Self-assembly of emulsion droplets through programmable folding”. In: *Nature* 610.7932 (Oct. 2022), pp. 502–506.

[60] Gaurav Mitra et al. “A coarse-grained simulation model for colloidal self-assembly via explicit mobile binders”. In: *Soft Matter* 19.23 (2023), pp. 4223–4236.

[61] Norman J. Wagner and William B. Russel. “Light scattering measurements of a hard-sphere suspension under shear”. In: *Physics of Fluids A: Fluid Dynamics* 2.4 (Apr. 1990), pp. 491–502.

[62] Vittorio Cristini, J. Bławzdziewicz, and Michael Loewenberg. “Near-contact motion of surfactant-covered spherical drops”. In: *Journal of Fluid Mechanics* 366 (July 1998), pp. 259–287.

[63] Allan K. Chesters and Ivan B. Bazhlekov. “Effect of insoluble surfactants on drainage and rupture of a film between drops interacting under a constant force”. In: *Journal of Colloid and Interface Science* 230.2 (Oct. 2000), pp. 229–243.

[64] P.A. Pincus, C.J. Sandroff, and T.A. Witten. "Polymer adsorption on colloidal particles". In: *Journal de Physique* 45.4 (1984), pp. 725–729.

[65] E Pefferkorn and A Elaissari. "Adsorption—desorption processes in charged polymer/colloid systems; structural relaxation of adsorbed macromolecules". In: *Journal of Colloid and Interface Science* 138.1 (Aug. 1990), pp. 187–194.

[66] Andre E. Nel et al. "Understanding biophysicochemical interactions at the nano–bio interface". In: *Nature Materials* 8.7 (July 2009), pp. 543–557.

[67] Todd M. Squires and John F. Brady. "A simple paradigm for active and nonlinear microrheology". In: *Physics of Fluids* 17.7 (2005), pp. 1–21.

[68] B. Cichocki and B. U. Felderhof. "Influence of hydrodynamic interactions on self-diffusion and stress relaxation in a semidilute suspension of hard spheres". In: *Physica A: Statistical Mechanics and its Applications* 198 (3-4 1993).

Chapter 3

Anisotropic self assembly and multibody effects

1. This chapter includes content from our submitted manuscript:

   [1] Y. Xu, P. Jandhyala, and S. C. Takatori. "Dynamic surfactants for colloidal self assembly."

   Y.X. participated in the conception of the project, conducted simulations, analyzed the data, and participated in the writing of the manuscript.

3.1 Introduction

In colloidal self assembly, the shape of particle building blocks may be engineered to achieve specific interparticle interactions and pack into well-defined, complex geometries. Understanding the interplay between particle shape and structures is essential for designing advanced colloidal materials with tailored properties. In general, spherical colloids with isotropic attractive interactions associate into a limited set of structures with space-efficient unit cells, such as HCP and FCC, once the interaction strength exceeds

the energy of thermal fluctuations.[1] For anisotropic colloids that interact directionally along different axes, the phase diagram contains more open and diverse morphologies that are inaccessible by spherical colloids with isotropic interactions.[2, 3] For example, patchy DNA-coated colloids may assemble into strings and sheets by limiting the patch coordination number or valency.[4, 5, 6, 7, 8, 9, 10] Elongated, rod-like colloids promote multi-body alignment and stacking, favoring the formation of aligned liquid crystalline phases and colloidal membranes.[11, 12] As another example, recent works have shown that shape-complementary colloidal pairs with cavities and internal voids may be exploited for lock-and-key self assembly mechanisms.[4, 13]

While anisotropic colloids formed through irreversible chemical and physical modifications have been well studied, colloids that can reversibly reconfigure their isotropic-to-anisotropic interactions offer new avenues for self assembly. Uniformly grafted nanoparticles can form anisotropic assemblies such as sheets and strings, although the physical mechanisms for this behavior have not been identified.[14] Colloids with dynamic shapes could exhibit adaptive behaviors such as structure reconfiguration or initiation of specific assembly pathways on demand, thereby avoiding kinetic traps that lead to uncontrolled aggregation and structural defects. To achieve such dynamic interactions, we have demonstrated in a previous paper the capability to engineer colloidal particles with surface-mobile, sterically-hindering polymer brushes.[15] Surface-mobile polymers enable a dynamic, contact time-dependent pair interaction which may be regulated by nonequilibrium forces. Other groups have shown that colloids coated by surface-mobile binders such as DNA-linkers are able to reversibly form adhesive patches, enabling multi-stage self assembly approaches. [16, 17, 9, 18] By harnessing the inherent responsiveness of these dynamic particles, we aim to engineer colloids with surface-tunable properties that are responsive to changes in their environment.

In this paper, we use Brownian Dynamics (BD) simulations and liquid state theory

to study the self assembly of colloids coated with surface-mobile polymers that act as "dynamic surfactants" (Fig. 5.1a-b). Multibody effects drive the reorganization of local surface polymers such that intrinsically isotropic colloids may reversibly adopt anisotropic patches upon assembly into higher order structures. By controlling density, attraction strength, and polymer surface coverage, we observed a rich self assembly phase space that is inaccessible by colloids with purely isotropic interactions, including vesicles, bilayers, and strings. We find that surface-mobile polymers are analogous to amphiphilic surfactants, where a critical packing parameter relating the head and tail shapes predicts the formation of micelles and bilayers.[19]

3.2 Methods

3.2.1 Simulation protocol

As shown in Fig. 5.1b, we perform Brownian Dynamics (BD) simulations of colloids of radius $R_c = \sigma$ coated by surface-mobile polymers and suspended in an implicit Newtonian solvent of viscosity η. We briefly summarize the protocol for tethering polymer chains onto colloidal surfaces, as documented previously.[15] Surface-mobile polymers are modeled using a semi-flexible Kremer-Grest bead-spring model, where the bead diameter is $d_p = 0.7\sigma$. Each polymer chain comprises n polymer beads and each colloid comprises m monomers.[20] In Fig. 5.1c, one end bead of the polymer is constrained on the colloidal surface via a stiff harmonic bond such that it may freely diffuse tangentially but cannot detach from the surface. All non-bonded particle pairs interact through a Weeks-Chandler-Anderson (WCA) hard sphere-like potential. To study self assembly, we introduce a short-range attraction between the colloidal cores via a Yukawa potential with magnitude $-a$, screening length $\kappa = 1$, and truncation at $r_{cut} = 3R_c$.

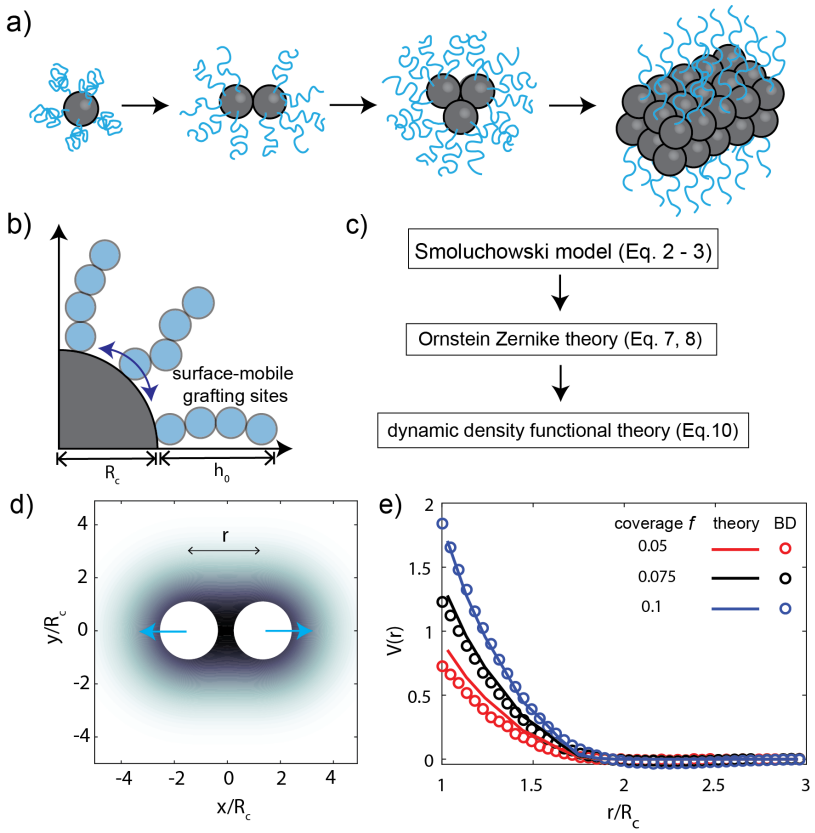

Figure 3.1: Multi-body interactions between attractive colloids coated with "dynamic surfactants" induce anisotropic assemblies. A) Cartoon showing progression of self assembly from single colloids (gray) coated by surface-mobile polymers (blue). Polymers exclude out of the contact interfaces to minimize steric interactions, resulting in anisotropic growth of superstructures. B) Schematic of end-grafted polymers whose grafting sites are free to diffuse laterally along the surfaces, with average brush height h_0 coating the colloid of radius R_c. C) Flow diagram of our theory that couples the polymer conformations to colloidal phase behavior. D) Cross-sectional plot showing the solution to Eqs. 3.2-3.3 for polymer distribution ρ for a pair of colloids separated at distance r. E) Potential of mean force from Eq. 3.6 as a function of r with Brownian dynamics (BD) simulation results (markers) and theoretical predictions (line) for three different surface coverages. BD data is obtained through a Boltzmann inversion of a semi-dilute suspension.

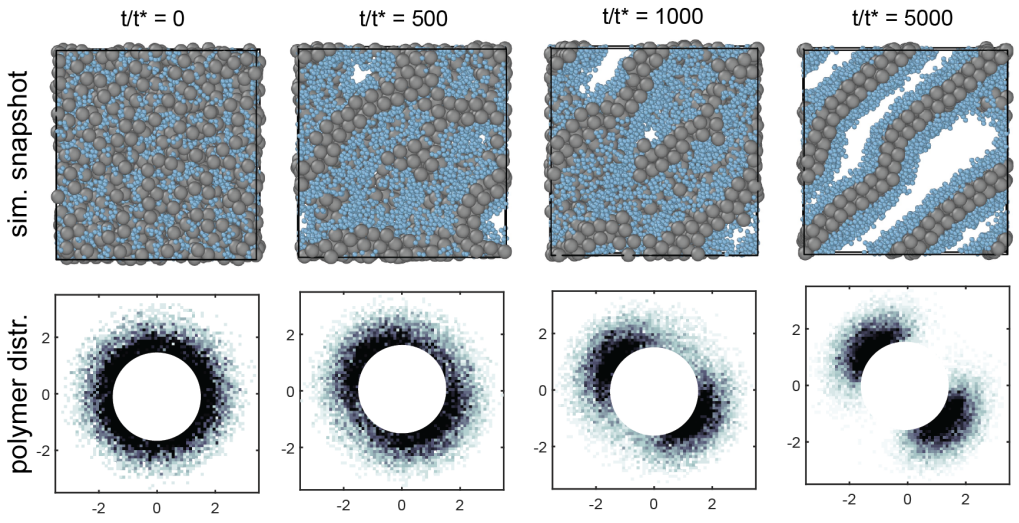

Figure 3.2: Macroscopic colloidal self assembly is coupled to surface rearrangements of the dynamic surfactants. The BD snapshots of polymer-coated colloids (top row) and corresponding averaged polymer distributions viewed along one direction (bottom row) are shown as a function of increasing simulation time (left to right). At short times $t/t^* \leq 500$, colloids associate to form an intermediate string phase and do not exhibit global structure. The corresponding average polymer distribution remains uniformly distributed in a corona around the colloids. At longer times, the colloidal assemblies rearrange to form a lamellar phase consisting of bilayer sheets that stack together. Polymers visibly segregate to above or below the colloidal sheet to minimize the steric overlap at colloid-colloid contact sites. Colloidal packing fraction is $\phi = 0.25$, surface coverage is $f = 0.05$, chain length is $m = 2$, and reduced temperature is $k_{\mathrm{B}}TR_{\mathrm{c}}/a = 0.24$. The characteristic Brownian timescale of the colloid is $t^* = 4R_{\mathrm{c}}^2/D_{\mathrm{c}}$.

All particles in the simulation follow the overdamped Langevin equations of motion:

$$\zeta \frac{\Delta \mathbf{x}_i}{\Delta t} = \underbrace{\mathbf{F}_i^{\mathrm{P}}}_{\text{interaction}} + \underbrace{\mathbf{F}_i^{\mathrm{R}}}_{\text{thermal}} \tag{3.1}$$

with contributions from interparticle interactions and thermal forces that satisfy fluctuation dissipation. In Eq. 4.18, ζ is the drag coefficient following the Stokes-Einstein-Sutherland relation. For all simulations, we choose a time step $\Delta t = (2\times10^{-4})R_{\mathrm{c}}^2/D_{\mathrm{c}}$ and sample the simulation every 10^5 time steps. The characteristic timescale $t^* = 4R_{\mathrm{c}}^2/D_{\mathrm{c}}$ describes the Brownian timescale of the colloid to diffuse the distance of its diameter. To obtain representative statistics, we simulate $N_{\mathrm{c}} = 1000 - 1200$ colloidal particles for 8×10^8 time steps. Due to the coarse-graining of polymer segments, our simulation results capture relaxation beyond the Brownian timescale of the polymer bead $t \sim d_{\mathrm{p}}^2/D_{\mathrm{p}}$ and do not account for fluctuations at smaller length and timescales. Simulations are performed in a 3-dimensional box of volume L^3, where L is varied between 20σ and 60σ to produce the desired packing fraction, using HOOMD-Blue, a GPU-accelerated Python package.[21]

3.2.2 Theoretical model

To complement our BD simulations, we develop a theoretical framework to understand how interactions facilitated by surface-mobile polymers influence macroscopic colloidal phase behavior. As outlined in Fig. 5.1c, we use a field-based Smoluchowski theory to model polymers and extract a potential of mean force experienced by pairs of colloids. We then compute the correlation functions in the bulk fluid using a standard liquid state approach.[22] Finally, we apply dynamic density functional theory (DDFT) to predict the phase behavior and stability of the system.

The analytical theory to capture the effective colloidal interaction mediated by surface-

bound polymers has been documented [15]. Assuming that the surface polymers relax quickly relative to the timescale at which colloids self-assemble, the probability density $\rho(\mathbf{h}, t)$ of finding a polymer bead at position $\mathbf{h}$ satisfies the steady state Smoluchowski equation:

$$0 = -\nabla \cdot \mathbf{j}(\mathbf{h}) \tag{3.2}$$

where the nondimensional polymer flux contains thermal, entropic elasticity, and excluded volume contributions:

$$\mathbf{j}(\mathbf{h}) = -\nabla\rho(\mathbf{h}) - \rho(\mathbf{h})\nabla\frac{U_{\mathrm{el}}(\mathbf{h})}{k_{\mathrm{B}}T} - \rho(\mathbf{h})\nabla\frac{U_{\mathrm{excl}}(\mathbf{h})}{k_{\mathrm{B}}T}. \tag{3.3}$$

In Eq. 3.2 - 3.3, we have nondimensionalized time by t^* and all distances by d_{p}.

The excluded volume contribution is given by a nonlinear term:

$$\frac{U_{\mathrm{excl}}(\mathbf{h})}{k_{\mathrm{B}}T} = B_2 \int \rho(\mathbf{h})\rho(\mathbf{h} - \mathbf{h}')d\mathbf{h}' \tag{3.4}$$

where B_2 is the excluded volume parameter. Using well-established polymer brush theory, we assume that the entropic elasticity of the polymer brush around a single colloid can be described by a harmonic potential of the form $U_{\mathrm{el}} \sim \frac{r^2-(R_{\mathrm{c}}+\frac{d_{\mathrm{p}}}{2})^2}{n^2 d_{\mathrm{p}}^2}$ which penalizes polymer beads from being strongly stretched [23, 24]. We approximate the external potential for polymer beads around two colloids by inverting the sum of two Boltzmann distributions about each colloid:

$$\frac{U_{\mathrm{el}}(\mathbf{h})}{k_{\mathrm{B}}T} = -\log\left[e^{-\frac{r_1^2-(R_{\mathrm{c}}+\frac{d_{\mathrm{p}}}{2})^2}{n^2 d_{\mathrm{p}}^2}} + e^{-\frac{r_2^2-(R_{\mathrm{c}}+\frac{d_{\mathrm{p}}}{2})^2}{n^2 d_{\mathrm{p}}^2}}\right]. \tag{3.5}$$

where $r_1(\mathbf{h}), r_2(\mathbf{h})$ are the distances from each of the colloid centers. Furthermore, the system obeys mass conservation $\int \rho dr^3 = nm$ and satisfies no flux boundary conditions

on the colloidal contact interfaces S_1, S_2 as well as zero density at $r \to \infty$. Equations 3.2-3.3 are numerically evaluated using the finite element software package FreeFEM++ for an arbitrarily-large 3-dimensional volume which includes both colloidal particles and the two polymer brush domains [25]. In Fig. 5.1d, we show the solution ρ for a given colloidal separation of $r/R_c = 1.5$. The higher density of polymers at the interface results in a repulsive force that pushes the colloids apart.

From the polymer distribution ρ, we may compute a potential of mean force $V(r)$ for two colloids, separated at r, to overcome the osmotic force exerted by polymers along the colloidal pair's line of centers [26]. Since we only account for hard-sphere interactions, this potential reduces to a simple form:

$$\frac{V(r)}{k_B T} = \int_{\infty}^{r} \oint_{\partial S} \rho(r') d\mathbf{S} dr' \tag{3.6}$$

where $\mathbf{S}$ is the contact surface between the polymers and the colloid.

In Fig. 5.1e, we present $V(r)$ as a function of the separation r for three different surface coverages f. The BD simulations are obtained through Boltzmann inversion of the pair distribution function in a dilute system without attraction. This calculation is analogous to integrating the force experienced by a single colloid at equilibrium when separated from another colloid at distance r. In Fig. 5.1e, we observe that the theoretical prediction agrees well with BD results for all surface coverages, but slightly overestimates the near-field repulsion at $1 \leq r/R_c \leq 1.5$. This overestimate is attributed to the inaccuracy of the brush potential in describing the polymers at such dilute densities, where it is expected that the surface-tethered polymers behave in a mushroom regime as opposed to brush regime. Due to the mass conservation constraint, the potential of mean force is proportional to the number of polymer chains m and consequentially the surface coverage f.

3.2.3 Dynamic Density Functional Theory

In order to predict the phase behavior of our colloids with dynamic surfactants, we turn towards spinodal decomposition theory.[27, 28] First, we use liquid state theory to extract equilibrium correlation functions for our inhomogenous system. The equilibrium structural correlations are well described by the Ornstein-Zernike equation,

$$h(r) = c_0(r) + \psi_0 \int c_0(r - r')h(r')dr' \tag{3.7}$$

where ψ_0 is the average number density, $h(r) = g(r) - 1$ is the total correlation function, and $c_0(r)$ is the direct correlation function between polymer-coated colloids without attraction. To solve Eq. 3.7 for the two unknown functions h and c_0, we require a closure relation. For simplicity, we choose the hypernetted chain (HNC) closure:

$$h(r) = e^{-\beta V(r)+h(r)-c_0(r)} - 1. \tag{3.8}$$

To evaluate Eq. 3.7, we use fast Fourier transforms (FFT) and choose 1024 grid points with a domain size of $L = 20\pi$. We use a standard Picard iteration scheme to evaluate the equations, [29, 30] and converge solutions until we reach a tolerance of 10^{-14}. Note that the potential of mean force $V(r)$ does not contain the attractive component and is purely the polymer-mediated repulsion.

We next invoke the random phase approximation and assume that the direct correlation function $c(r)$ of the corresponding equilibrium fluid with attraction is well described by:

$$c(r) = c_0(r; \psi_0) + \beta v_{\text{Yukawa}}(r). \tag{3.9}$$

With the full $c(r)$, we are now in a position to write down the dynamic density

functional theory (DDFT) equation for colloidal particles: [31, 32]

$$\frac{\partial\psi(\mathbf{r},t)}{\partial t} = \nabla\left[\psi(\mathbf{r},t)\nabla\frac{\delta F[\psi(\mathbf{r},t)]}{\delta\psi(\mathbf{r},t)}\right] \tag{3.10}$$

where the Helmholtz free energy functional $F[\psi(\mathbf{r},t)]$ is given by:

$$F[\psi(\mathbf{r},t)] = F_{\mathrm{id}}[\psi(\mathbf{r},t)] + F_{\mathrm{ex}}[\psi(\mathbf{r},t)]. \tag{3.11}$$

In Eq. 3.11 the first term represents the ideal gas entropic contribution and the second term is the excess free energy that models interactions with other colloids in the fluid. The DDFT approach relies on the adiabatic approximation which assumes that the nonequilibrium system evolves based on equilibrium density correlations, [22] such that the excess free energy may be expressed in terms of the direct correlation function:

$$\beta\frac{\delta F_{\mathrm{ex}}[\psi(\mathbf{r})]}{\delta\psi(\mathbf{r})} = -c(\mathbf{r}). \tag{3.12}$$

3.3 Results

3.3.1 "Dynamic surfactant" rearrangements

We first consider the temporal evolution of the colloidal structure and local polymer configurations. Simulations of colloids with isotropic attractive interactions and repulsive surface-mobile polymers were performed at packing fraction $\phi = \frac{N_c\pi 4R_c^3}{3L^3} = 0.25$, fractional surface coverage $f = A_p/A_c = 0.05$ where $A_c = \pi R_c^2$ is the colloid surface area, $A_p = m\pi R_g^2$ is the estimated colloidal surface area covered by polymers, and $R_g = nd_p^2/6$ is the radius of gyration of the linear chain.[33] In Fig. 5.2, we present both the simulation snapshot and heat maps of the corresponding polymer distribution around individual col-

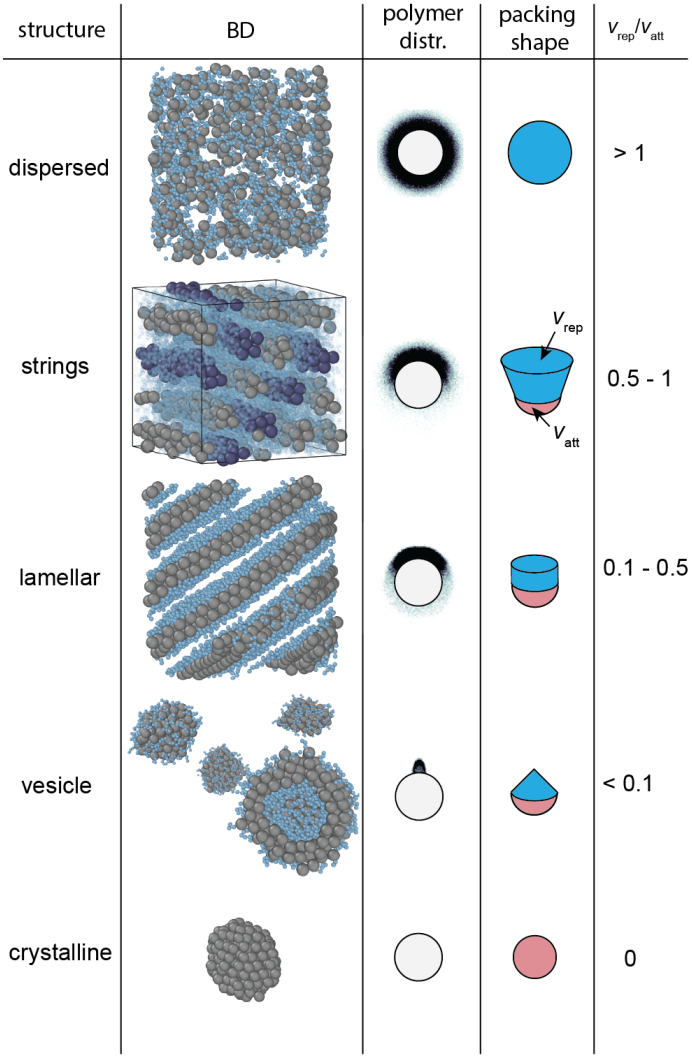

Table 3.1: Colloids with dynamic surfactants assemble into anisotropic structures. Second column is the snapshot from BD simulations, third column is the local average polymer distribution from simulations, and fourth column is a cartoon of the packing shape of the colloidal building block, with the attractive core in red and the sterically-hindering polymer layer in blue. Last column indicates the packing parameter which is a ratio of the excluded volume by the polymer beads $v_{\mathrm{rep}} = nm\pi d_{\mathrm{p}}^3/6$ and the volume of the attractive core $v_{\mathrm{att}} = \pi 4R_{\mathrm{c}}^3/3$. The reduced temperature is $k_{\mathrm{B}}TR_{\mathrm{c}}/a = 0.2$ for all structures.

loids, averaged over the entire suspension and viewed along one direction. The suspension begins from a homogeneous, dispersed state at $t/t^* = 0$ where polymer chains appear spatially uniform and evenly distributed around the colloids, resulting in isotropic interactions. At intermediate times, the colloids spontaneously self assemble into string-like aggregates that are 2-3 particles wide to minimize their free energy while maximizing polymer entropic degrees of freedom.

At late stages of the assembly process, $t/t^* \geq 1000$, we observe a transition from string-like structures to a lamellar phase, consisting of bilayer colloidal sheets stacked together. Correspondingly, surface polymers segregate into two distinct poles and expose the colloid-colloid contact areas, consistent with the multi-step assembly pathway hypothesized in Fig. 5.1a. The resulting anisotropy is an entropic effect unique to our dynamic surfactants in contrast to traditional polymer-coated particles where the grafting sites are fixed in place. The bilayer structure resembles prior work on patchy particles, despite the fact that the surface-mobile polymers assume isotropic distributions on an isolated colloid.[34, 35] The polymer densities at the poles experience up to a $4x$ increase, which acts to swell the polymer brushes and limit colloidal assembly along the perpendicular direction to the bilayer. Additionally, the presence of the polymer brush exerts a lateral osmotic pressure which stabilizes the bilayer against collapse, similar to how incorporation of polymer-grafted lipids increases the bending rigidity and elastic modulus of lipid bilayers.[36] Note that while in simulations the polymers exclude to either above or below the bilayer, Fig. 5.2 shows polymer density at both hemispheres due to averaging.

3.3.2 Critical polymer packing determines structure

We have shown in the previous section that macroscopic colloidal assembly is dynamically coupled to microscopic polymer conformations. To quantitatively understand this relationship, we investigate the steady state structures achievable through tuning the polymer surface coverage. Here, the steric hindrance imposed by the polymers may be quantified by a critical packing parameter, which is a ratio of the polymer excluded volume $v_{\mathrm{rep}} = nm\pi d_{\mathrm{p}}^3/6$ and the volume of the attractive core $v_{\mathrm{att}} = 4\pi R_{\mathrm{c}}^3/3$. By varying $v_{\mathrm{rep}}/v_{\mathrm{att}}$, a quantity which is intrinsic to the polymer properties, we hypothesize that the morphology of the steady state structure may be precisely tuned.

We present resulting superstructures as a function of the critical packing parameter in an organized chart in Table 3.1. When no polymers are present, i.e. $v_{\mathrm{rep}}/v_{\mathrm{att}} = 0$, the colloids form equilibrium HCP crystals at lower packing fractions or kinetically arrest into gel-like aggregates at higher concentrations.[37, 38] When surface-mobile polymers are present, different structures arise due to changes in the polymer distribution. For $v_{\mathrm{rep}}/v_{\mathrm{att}} < 0.1$, we observe formation of vesicle-like structures, where two leaflets of colloids form a spherical shell and polymers are excluded to either the inner or outer surfaces. We hypothesize that the vesicle state is possible at low $v_{\mathrm{rep}}/v_{\mathrm{att}}$ because the small amount of polymers present on the surface enforces an anisotropic packing shape and prevents collapse into a tighter structure. Provided that the reduced temperature is sufficiently high, the vesicle is formed from an initial, fluctuating bilayer that spontaneously acquires sufficient membrane curvature. Note that sufficiently large simulation boxes are required to observe vesicles as opposed to the system-spanning, lamellar structures.[39]

At higher $0.1 < v_{\mathrm{rep}}/v_{\mathrm{att}} < 0.5$, the steric polymer interactions increase the bending energy of the bilayer, such that the lamellar phase becomes preferred over vesicle-type structures.[36] By controlling the strength of the cohesive attraction, the lamellar phase

either undergoes spatial fluctuations at higher reduced temperatures or remains rigid as a crystalline layer at lower reduced temperatures. The orientational ordering and bilayer fluctuations in these simulations qualitatively resemble that of lipid membranes [40, 41, 42, 39] but do not require angle-dependent simulation potentials or hydrophobic and hydrophilic interactions. We note that to form these structures, the polymers must be able to cylindrically pack onto one hemisphere of the colloidal core, as indicated by the polymer distribution. At packing parameters $v_{\mathrm{rep}}/v_{\mathrm{att}}$ approaching unity, the bilayers undergo a 2D to 1D phase transition to form coiled, string-like phases that span the simulation box. We hypothesize that this transition occurs because the polymer entropic contributions exceeds that of the cohesive enthaplic forces which stabilize the bilayer. Finally, when v_{rep} exceeds v_{att}, the steric repulsion is strong enough to overcome the underlying attractive forces at a pairwise level, resulting in uniform shielding of the underlying attractive interactions and recovery of the dispersed state. The packing parameter-based argument has similarities with the geometric packing theory for aggregation of amphiphilic surfactants, where a dimensionless packing parameter relating the head and tail group shapes predicts formation of micelles and bilayers.[19]

3.3.3 Self assembly phase diagram

To gain further insight on how parameters such as temperature and polymer coverage regulate self assembly, we develop a simple theoretical model using a mean-field DDFT theory, which has been successfully used to model spinodal decomposition of simple colloidal fluids.[31] DDFT has also been applied to colloids interacting via long-ranged interactions to form repulsive crystals.[43] Under the DDFT framework, one obtains the following linear stability result for the growth rate of instabilities perturbed about a

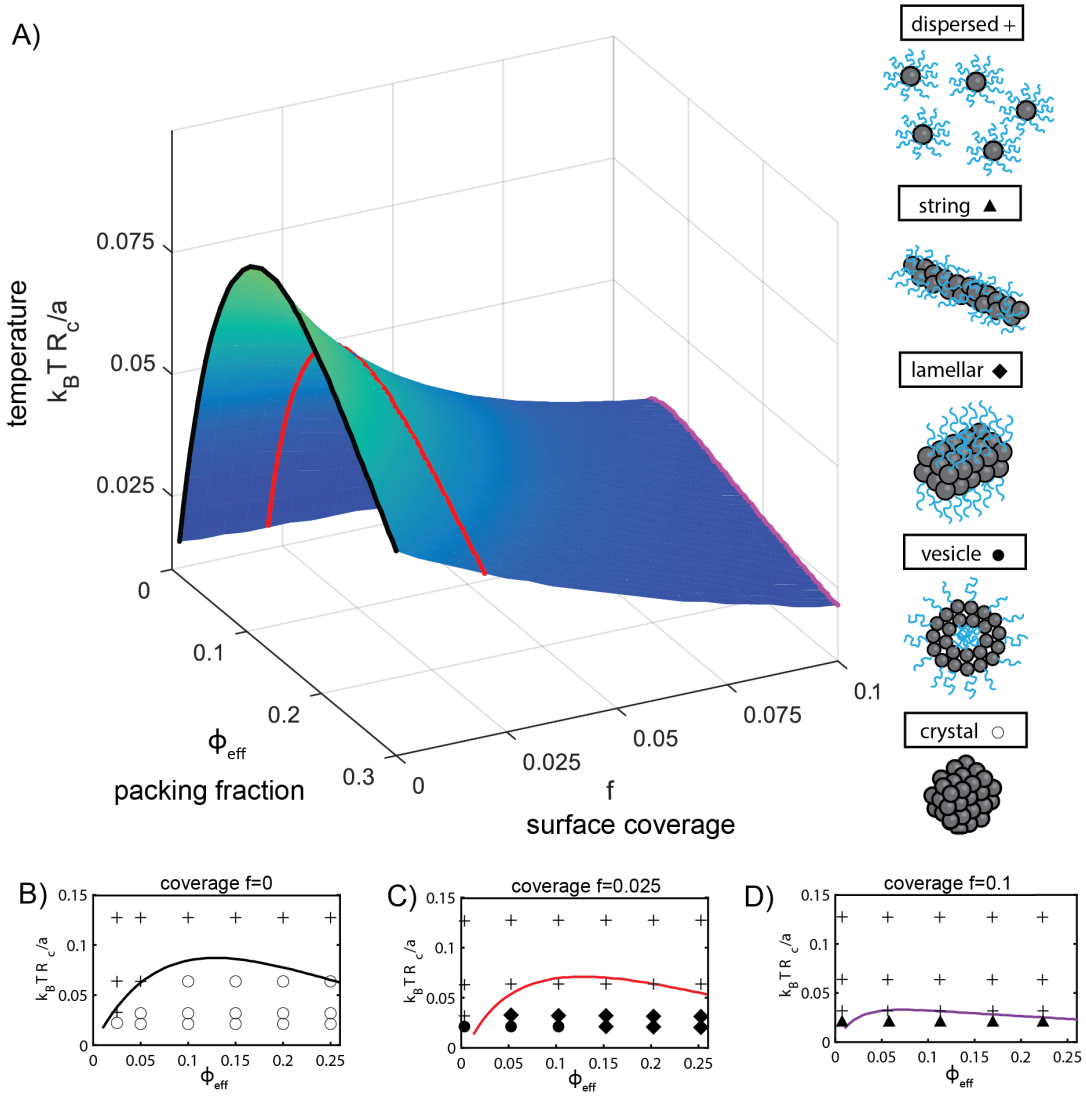

Figure 3.3: Phase diagram of sticky colloids coated with surface-mobile polymers acting as dynamic surfactants. A) Three-dimensional spinodal curve demonstrating phase behavior with varying temperature, effective colloid packing fraction, and surface polymer coverage. Color gradient varies with reduced temperature as a guide for the eye. Cross-sectional plots for bare colloids (B) $f = 0$ (black) and fixed surface coverage of (C) $f = 0.025$ (red), (D) $f = 0.1$ (purple). Solutions to our theory Eq. 3.7 are shown in solid lines and BD simulation state points are shown in markers.

uniform suspension of density, ψ_0 :

$$\omega = -D_c k^2 \left(1 - \psi_0 \frac{\hat{c}(k)}{k_B T}\right), \tag{3.13}$$

where $\hat{c}(k)$ is the Fourier transform of the direct correlation function $c(r)$, which is related to the excess free energy in Eq. 3.11.[31] When the real part of the growth rate ω is negative for all wavenumbers k, the system is linearly stable against fluctuations. In contrast, if the real part of ω is positive, phase separation via spinodal decomposition is predicted to occur at a wavenumber dominated by a critical value k_{max}.

In Fig. 5.3a, we present the spinodal curve as a function of the reduced temperature, effective packing fraction, and surface polymer coverage. Because the presence of polymers slightly increases the 3D crowding, we report the effective packing fraction $\phi_{eff} = \phi + N_c mn \frac{\pi d_p^3}{6L^3}$ which corrects for the volume of the polymer beads. Above the spinodal, the system is linearly stable against small fluctuations and exists as a homogenous suspension. When quenched to a low reduced temperature below the spinodal, the system undergoes spontaneous phase separation. We chose to vary the number of polymers on the colloidal surface m to sweep different surface coverages f in the simulations and keep the chain length n constant. Cross-sections at constant surface coverages f are presented in Fig. 5.3 b-d for better visualization, where we validate our theoretical results with BD data. The dispersed phase corresponds to only a single peak in the radial distribution function $g(r)$, while all other phases are classified based on their morphologies which has been tabulated in Table 3.1.

When no polymers are present ($f = 0$), we recover exactly the Archer and Evans result for the phase diagram, as shown in Fig. 5.3b.[31] The BD simulations exhibit either dispersed suspensions or tight, crystalline structures, and quantitatively agree with our theoretical result. As f increases, the polymers more effectively screen the

attraction, and the spinodal becomes suppressed. At surface coverages of $f = 0.025$, we observe formation of vesicles in larger simulation boxes ($\phi_{\text{eff}} \leq 0.1$) and lamellar phases in smaller boxes ($\phi_{\text{eff}} > 0.1$). At the highest surface coverages $f = 0.1$, we observed only the dispersed state and the string-like phase. While morphologies observed previously in Table 3.1 exactly correspond to regions in the spinodal, our theory is designed to predict the initial instability and onset of self assembly, not the late-time evolution into higher-order morphologies. We attribute this limitation to the linear stability analysis, which only considers small disturbances to the homogeneous fluid. Additionally, by inputing only the dilute, two-body interactions $V(r)$ which are isotropic, we are unable to capture the anisotropic interactions that generate the higher order assemblies, as shown in Fig. 5.2 and Table 3.1.

In conclusion, we have demonstrated that sticky colloids coated with surface-mobile polymers exhibit rich self assembled morphologies due to coupling between macroscopic structure and microscopic polymer rearrangements. We observed that surface-mobile polymers behave as "dynamic surfactants" that reorganize and promote anisotropic assembly of vesicle, lamellar, and string phases. A critical geometric packing parameter describing the polymer free volume precisely governs structure formation, much like the theory for self assembly of amphiphilic surfactants. Furthermore, our analytical theory describes the coupling between the reduced temperature and surface coverage required to observe self assembly via a phase-separation mechanism. In contrast to traditional polymer-grafted particles whose polymer grafting sites are chemically fixed, surface mobility enables isotropic colloids to acquire different shapes during the assembly progress, which is particularly important in nonequilibrium settings. Further work in this area could leverage nonequilibrium effects such as fluid flow to control the rate at which self assembly occurs, which may enable dynamic structural reconfiguration. Hydrodynamic interactions also influence colloidal pair distributions as well as phase separation of col-

loidal gels.[44] Surface mobile groups on emulsions and droplets have been shown to display interesting folding mechanisms during self assembly, which could be leveraged as well. [45, 18]

Bibliography

[1] S. C. Glotzer, M. J. Solomon, and N. A. Kotov. "Self-assembly: From nanoscale to microscale colloids". In: *AIChE Journal* 50 (12 Dec. 2004), pp. 2978–2985.

[2] Stefano Sacanna and David J. Pine. "Shape-anisotropic colloids: Building blocks for complex assemblies". In: *Current Opinion in Colloid Interface Science* 16 (2 Apr. 2011), pp. 96–105.

[3] Vinothan N. Manoharan. "Colloidal matter: Packing, geometry, and entropy". In: *Science* 349 (6251 Aug. 2015).

[4] Stefano Sacanna et al. "Shaping colloids for self-assembly". In: *Nature Communications* 4.1 (Apr. 2013), p. 1688.

[5] Greg van Anders et al. "Entropically Patchy Particles: Engineering Valence through Shape Entropy". In: *ACS Nano* 8 (1 Jan. 2014), pp. 931–940.

[6] Gang Chen et al. "Regioselective surface encoding of nanoparticles for programmable self-assembly". In: *Nature Materials* 18 (2 Feb. 2019), pp. 169–174.

[7] Yufeng Wang et al. "Colloids with valence and specific directional bonding". In: *Nature* 491 (7422 Nov. 2012), pp. 51–55.

[8] Tianran Zhang et al. "Programming Self-Assembled Materials With DNA-Coated Colloids". In: *Frontiers in Physics* 0 (July 2021), p. 330.

[9] Stefano Angioletti-Uberti et al. "Mobile linkers on DNA-coated colloids: Valency without patches". In: *Physical Review Letters* 113.12 (Sept. 2014), p. 128303.

[10] Flavio Romano, Eduardo Sanz, and Francesco Sciortino. "Crystallization of tetrahedral patchy particles in silico". In: *The Journal of Chemical Physics* 134.17 (May 2011).

[11] Lars Onsager. "The effects of shape on interaction of colloidal particles". In: *Annals of the New York Academy of Sciences* 51.4 (May 1949), pp. 627–659.

[12] Edward Barry and Zvonimir Dogic. "Entropy driven self-assembly of nonamphiphilic colloidal membranes". In: *Proceedings of the National Academy of Sciences* 107.23 (June 2010), pp. 10348–10353.

[13] Giorgio Cinacchi and Jeroen S. van Duijneveldt. "Phase Behavior of Contact Lens-Like Particles: Entropy-Driven Competition between IsotropicNematic Phase Separation and Clustering". In: *The Journal of Physical Chemistry Letters* 1.4 (Feb. 2010), pp. 787–791.

[14] Pinar Akcora et al. "Anisotropic self assembly of spherical polymer grafted nanoparticles". In: *Nature Materials* 8.4 (Mar. 2009), pp. 354–359.

[15] Yaxin Xu et al. "Dynamic interfaces for contact-time control of colloidal interactions". In: *Soft Matter* 19.30 (2023), pp. 5692–5700.

[16] Mirjam E. Leunissen et al. "Switchable self protected attractions in DNA functionalized colloids". In: *Nature Materials* 8.7 (2009), pp. 590–595.

[17] Stef A.J. Van Der Meulen and Mirjam E. Leunissen. "Solid colloids with surface-mobile DNA linkers". In: *Journal of the American Chemical Society* 135.40 (Oct. 2013), pp. 15129–15134.

[18] Gaurav Mitra et al. “A coarse-grained simulation model for colloidal self-assembly via explicit mobile binders”. In: *Soft Matter* 19.23 (2023), pp. 4223–4236.

[19] Jacob N. Israelachvili. “Intermolecular and Surface Forces, Third Edition”. In: *Intermolecular and Surface Forces, Third Edition* (2010), pp. 1–674.

[20] Kurt Kremer and Gary S Grest. “Dynamics of entangled linear polymer melts: A molecular-dynamics simulation”. In: *The Journal of Chemical Physics* 92.8 (1990), pp. 5057–5086.

[21] Joshua A. Anderson, Jens Glaser, and Sharon C. Glotzer. “HOOMD-blue: A Python package for high-performance molecular dynamics and hard particle Monte Carlo simulations”. In: *Computational Materials Science* 173 (Feb. 2020), p. 109363.

[22] Jean Pierre Hansen and I. R. McDonald. *Theory of Simple Liquids: With Applications to Soft Matter: Fourth Edition*. Elsevier, 2013, pp. 1–619.

[23] P. G. de Gennes. *Polymers at an interface; a simplified view*. 1987.

[24] S. T. Milner. “Polymer Brushes”. In: *Science* 251.4996 (Feb. 1991), pp. 905–914.

[25] Frédéric Hecht and F Hecht. “New development in freefem++”. In: *Journal of Numerical Mathematics* 20.0 (2012), pp. 1–14.

[26] Federica Loverso, Sergei A. Egorov, and Kurt Binder. “Interaction between polymer brush-coated spherical nanoparticles: Effect of solvent quality”. In: *Macromolecules* 45.21 (Nov. 2012), pp. 8892–8902.

[27] C. Caccamo and G. Giunta. “Microscopic theoretical description of phase stability in hard sphere yukawa mixtures”. In: *Molecular Physics* 78.1 (Jan. 1993), pp. 83–93.

[28] Nathan A. Mahynski and Athanassios Z. Panagiotopoulos. "Grafted nanoparticles as soft patchy colloids: Self-assembly versus phase separation". In: *The Journal of Chemical Physics* 142.7 (Feb. 2015).

[29] F. J. Rogers. "A HNC study of asymmetrically charged hard spheres". In: *The Journal of Chemical Physics* 73.12 (Dec. 1980), pp. 6272–6278.

[30] Forrest J. Rogers and David A. Young. "New, thermodynamically consistent, integral equation for simple fluids". In: *Physical Review A* 30.2 (Aug. 1984), pp. 999–1007.

[31] A. J. Archer and R. Evans. "Dynamical density functional theory and its application to spinodal decomposition". In: *The Journal of Chemical Physics* 121.9 (Aug. 2004), p. 4246.

[32] Umberto Marini Bettolo Marconi and Pedro Tarazona. "Dynamic density functional theory of fluids". In: *The Journal of Chemical Physics* 110.16 (Apr. 1999), p. 8032.

[33] Masao Doi, Sam F Edwards, and Samuel Frederick Edwards. *The theory of polymer dynamics*. Vol. 73. oxford university press, 1988.

[34] William L. Miller and Angelo Cacciuto. "Hierarchical self-assembly of asymmetric amphiphatic spherical colloidal particles". In: *Physical Review E* 80.2 (Aug. 2009), p. 021404.

[35] Zdeněk Preisler et al. "Equilibrium phases of one-patch colloids with short-range attractions". In: *Soft Matter* 10.28 (2014), pp. 5121–5128.

[36] Kalina Hristova and David Needham. "The Influence of Polymer-Grafted Lipids on the Physical Properties of Lipid Bilayers: A Theoretical Study". In: *Journal of Colloid and Interface Science* 168.2 (Dec. 1994), pp. 302–314.

[37] P. Segrè et al. “Glasslike Kinetic Arrest at the Colloidal-Gelation Transition”. In: *Physical Review Letters* 86.26 (June 2001), pp. 6042–6045.

[38] Roseanna N Zia, Benjamin J Landrum, and William B Russel. “A micro-mechanical study of coarsening and rheology of colloidal gels: Cage building, cage hopping, and Smoluchowski’s ratchet”. In: *Citation: Journal of Rheology* 58 (2014), p. 1121.

[39] Ira R. Cooke and Markus Deserno. “Solvent-free model for self-assembling fluid bilayer membranes: Stabilization of the fluid phase based on broad attractive tail potentials”. In: *The Journal of Chemical Physics* 123.22 (Dec. 2005).

[40] Hongyan Yuan et al. “One-particle-thick, solvent-free, coarse-grained model for biological and biomimetic fluid membranes”. In: *Physical Review E - Statistical, Nonlinear, and Soft Matter Physics* 82.1 (2010).

[41] Hiroshi Noguchi. “Solvent-free coarse-grained lipid model for large-scale simulations”. In: *The Journal of Chemical Physics* 134.5 (Feb. 2011).

[42] Hayato Shiba and Hiroshi Noguchi. “Estimation of the bending rigidity and spontaneous curvature of fluid membranes in simulations”. In: *Physical Review E* 84.3 (Sept. 2011), p. 031926.

[43] Sven Van Teeffelen, Christos N. Likos, and Hartmut Löwen. “Colloidal crystal growth at externally imposed nucleation clusters”. In: *Physical Review Letters* 100.10 (Mar. 2008), p. 108302.

[44] Michio Tateno and Hajime Tanaka. “Power-law coarsening in network-forming phase separation governed by mechanical relaxation”. In: *Nature Communications* 12.1 (Feb. 2021), p. 912.

[45] Angus McMullen et al. “Self-assembly of emulsion droplets through programmable folding”. In: *Nature* 610.7932 (Oct. 2022), pp. 502–506.

Chapter 4

Nonequilibrium depletion interactions in microrheology

1. This chapter includes content from our previously published article:

   [1] Y. Xu and S. C. Takatori. "Nonequilibrium interactions between multi-scale colloids regulate the suspension microstructure and rheology". *Soft Matter* 2023, **19**, 8531-8541 doi: 10.1039/D3SM00947E.

   Y.X. participated in the conception of the project, conducted simulations, analyzed the data, and participated in the writing of the manuscript.

4.1 Introduction

When a colloidal suspension is driven out of equilibrium by body forces or hydrodynamic flows, interactions between the individual particles can couple with convective forces to induce microstructural reorganizations and relaxations across large time and length scales.[1, 2] As a result of these structural changes, colloidal suspensions can exhibit non-Newtonian behaviors such as shear thinning,[3, 4] shear thickening,[5, 6, 7, 8,

9, 10, 11] and viscoelasticity.[12, 13] As such, developing a relationship between interparticle interactions and suspension-level transport is a crucial goal for understanding many natural systems and soft materials.

Particle interactions in colloidal systems typically result from the local distribution of small molecules, polymers, or ions near the surfaces of the colloids. Particularly, adding non-adsorbing polymer coils to a colloidal suspension induces an entropic depletion force, responsible for a rich variety of phase phenomena including flocculation,[14] liquid-liquid phase separation,[15] and nucleation and crystallization.[16] Established by Asakura, Oosawa (AO), and Vrij, [17, 18] depletion forces at equilibrium result from depletants preferentially excluding from the vicinity of the larger colloids to induce an entropic attraction between colloidal pairs that scales with the thermal energy $k_{\mathrm{B}}T$ and the depletant concentration, n_{b}. Equilibrium-based models of the depletion potential have also been broadly applied to suspensions driven out of thermodynamic equilibrium as an approximation of the interparticle interactions. In biology, AO-type depletion potentials have been proposed as a model for reversible aggregation of red blood cells.[19, 20, 21] In synthetic systems, equilibrium depletion potentials are used to predict the rheology of colloid-polymer mixtures[22] and in simulating depletant-induced gelation processes.[23] [24, 25, 26, 27] The key underlying assumption is that there exists a separation of timescales between the slow rearrangement of large colloidal particles and the rapid equilibration of the small polymeric depletant bath, $\tau_{\mathrm{c}} \gg \tau_{\mathrm{b}}$, such that the depletant distributions behave quasi-statically under any nonequilibrium process which disturbs the colloidal-scale microstructure.

However, when the flow velocity is comparable to the thermal Brownian velocity of the depletants, the depletants no longer assume an equilibrium Boltzmann distribution around the colloids and the classic AO depletion potential is no longer an accurate model for colloidal interactions. For example, Dzubiella and coworkers have shown theoretically

that two fixed colloids in a drifting depletant bath exhibit anisotropic, flow-dependent depletion forces,[28] which have also been confirmed by Sriram and Furst through optical trapping experiments.[29] As a separate example, Xu and Choi et al. recently demonstrated that polymer-coated colloids exhibit dynamic pairwise forces which slowly relax over time when colloids are driven towards each other at speeds comparable to polymer surface diffusion.[30] While such nonequilibrium effects are important in dictating the macroscopic behavior of driven suspensions, developing models for out-of-equilibrium particle interactions remains a challenge. Previous work has primarily focused on bath particle organization around fixed colloids, while colloids in a free suspension are able to undergo motion under various forces such as Brownian diffusion and advection.[31, 32] It is still unclear how the local polymer distributions and timescales couple to suspension-level processes. We hypothesize that a competition between the depletant timescales τ_{b} and colloidal process timescales τ_{c} in nonequilibrium systems ultimately controls the suspension microstructure and rheology.

In this work, we use Smoluchowski theory and Brownian dynamics (BD) simulations to develop a multiscale framework for studying nonequilibrium interactions among colloids driven out of equilibrium. As a specific case study, we focus on the nonlinear microrheology of a bidisperse suspension of colloids and depletants. We show that the nonequilibrium colloidal microstructure and viscosity cannot generally be predicted by a naive application of an AO-type depletion potential. To the best of our knowledge, this work is the first full micro-mechanical consideration of a nonequilibium, multi-phase suspension that does not rely on any standard, equilibrium-based approximations.

The remainder of this work is organised as follows. In Section 2 we describe the model suspension and use the Smoluchowski framework to derive governing equations for the colloidal microstructure and viscosity. In Section 3 we present our results and analysis. Finally, we discuss the implications of our work in Section 4.

4.2 Methods

4.2.1 Model Preliminaries

Our theoretical framework is general to any imposed hydrodynamic flow, but we chose to focus here on a nonlinear microrheology problem to make comparisons with existing work. As depicted in Fig. 4.1, we consider a 2-dimensional system of two interacting colloidal particles suspended in a bath of smaller, ideal depletant particles in a Newtonian solvent with viscosity η and temperature T. Assuming the polymeric depletant behaves as a random walk chain that can be mapped onto a hard sphere, we choose the particle radii of the colloids and depletants as $d_\mathrm{c} = 5\sigma$ and $d_\mathrm{b} = 1\sigma$, respectively. We assume that the depletants are ideal and mutually uncorrelated but can interact with the larger colloidal particles. In constant-velocity nonlinear microrheology, we consider the behavior when one colloid particle (the "probe") is driven in the positive-x direction through the suspension at a probe velocity, $\mathbf{U}_1 = U_\mathrm{c}\mathbf{e}_x$, while all other particles move through Brownian motion and are quiescent. As the probe is pulled through the suspension, it experiences viscous drag forces from the Newtonian solvent and also from random collisions with suspended particles. Under these effects, the imposed velocity is related to an average force felt by the probe $\langle \mathbf{U}_\mathrm{c} \rangle = \mu_\mathrm{p}\mathbf{F}_1$ where μ_p is the mobility of the probe. This is contrasted with passive microrheology, where the probe itself undergoes Brownian fluctuations, and with constant-force nonlinear microrheology, where the probe is pulled at a fixed force and moves under a velocity that has been averaged over collisions with all remaining particles.

Neglecting hydrodynamic interactions, the viscous drag experienced by the depletants, ζ_b, and by the quiescent colloid, ζ_c, is related through a drag parameter, $\alpha = \zeta_\mathrm{c}/\zeta_\mathrm{b}$. Under the Stokes-Einstein-Sutherland (SES) relation for particle diffusion coefficients, $D_\mathrm{c,b} = k_\mathrm{B}T/\zeta_\mathrm{c,b}$, the relative drag parameter reduces to a ratio between the particle sizes,

$\alpha = d_c/d_b = 5$.[2] To thoroughly explore the relationship between diffusive timescales and microstructure, we consider the general case where the frictional drag coefficients may deviate from the SES relation. For example, if particles are embedded in a more complex environment, such as a hydrogel network, α may additionally depend on parameters such as mesh size and mesh stiffness.[33, 34, 35, 36] To reduce the number of parameters, we define a Péclet number $\mathrm{Pe}_c = U_c d_b/D_c$ relating the driving velocity to the speed at which the colloid diffuses in space. In general, the Péclet number Pe indicates the relative importance of external forcing to the thermal, restorative forces of the material. Since there are two particle species in the system, a second Pećlet number, $\mathrm{Pe}_b = U_c d_b/D_b$ relates the driving velocity to the speed at which the polymeric depletant diffuses. We note that these two nondimensional quantities are exactly related through the drag parameter, $\mathrm{Pe}_b = \mathrm{Pe}_c/\alpha$.

We now explain the micro-mechanical framework for this bidisperse suspension below.

4.2.2 Smoluchowski Framework

In colloidal suspensions, the microstructural response to nonequilibrium perturbation determines the rheological response of the material. The time-dependent distribution of particles in a suspension obeys the Smoluchowski equation, which balances fluxes of advection, interparticle forces, and Brownian diffusion. [37, 38, 3, 13, 39, 1] We have labeled all quantities with respect to the probe with the subscript $i = 1$, the quiescent colloid with $i = 2$, and the bath depletant with $i = 3$, respectively. The three-particle distribution P_3 of the probe, the quiescent colloid, and a depletant particle is given by:

$$\frac{\partial P_3}{\partial t} + \nabla \cdot \langle \mathbf{j}_2 - \mathbf{j}_1 \rangle_3 + \nabla_{\mathbf{h}} \cdot \langle \mathbf{j}_3 - \mathbf{j}_1 \rangle_3 = 0. \tag{4.1}$$

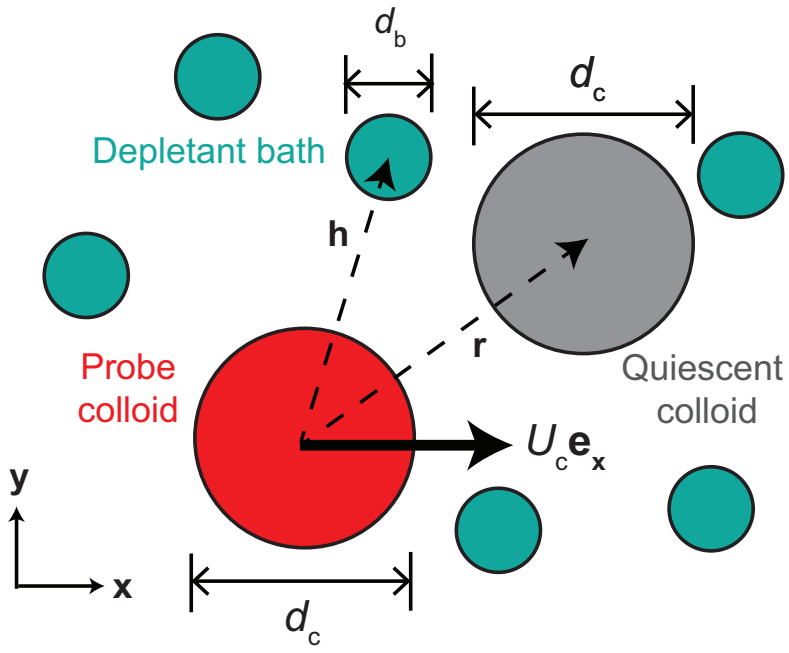

Figure 4.1: Schematic of a bidisperse model system depicting one probe colloid (red) and one quiescent colloid (gray) with size d_c suspended in a dilute bath of smaller bath particles (blue) with size d_b. The probe is driven at constant velocity U_c in the positive x-direction. The coordinates ($\mathbf{h}$, $\mathbf{r}$) denote the positions of a depletant and the quiescent colloid relative to the probe, respectively.

In Eq. 4.1, $\mathbf{j}_1$ is the probe flux, which is deterministic when driven at constant velocity, $\mathbf{j}_2$ is the flux of the quiescent colloid, and $\mathbf{j}_3$ is the flux of the bath depletant. The brackets $\langle ... \rangle_3$ represent a statistical average over the degrees of freedom of $N-1$ depletant particles. The relative flux of the quiescent colloid $\langle \mathbf{j}_2 - \mathbf{j}_1 \rangle$ is:

$$\langle \mathbf{j}_2 - \mathbf{j}_1 \rangle_3 = -\alpha^{-1} \left[\mathrm{Pe_c} P_3 \mathbf{e}_x + P_3 \nabla (V_{21} + V_{32})/(k_\mathrm{B}T) + \nabla P_3 \right], \tag{4.2}$$

and the relative flux of the depletant $\langle \mathbf{j}_3 - \mathbf{j}_1 \rangle$ is:

$$\langle \mathbf{j}_3 - \mathbf{j}_1 \rangle_3 = -\alpha^{-1} \mathrm{Pe_c} P_3 \mathbf{e}_x - P_3 \nabla_\mathbf{h} (V_{31} + V_{32})/(k_\mathrm{B}T) - \nabla_\mathbf{h} P_3. \tag{4.3}$$

The terms on the right hand side of Eq. 4.2and Eq. 4.3 represent contributions from advection due to probe motion, interparticle forces derived from probe-colloid (V_{12}), probe-depletant (V_{13}), and colloid-depletant (V_{23}) pair potentials, and thermal motion, respectively. We have rescaled all distances by the depletant size d_b, energies by the thermal energy $k_\mathrm{B}T$, and time by the Brownian timescale of the depletant particle, $\tau_\mathrm{c}^\mathrm{Brownian} = d_\mathrm{b}^2/D_\mathrm{b}$. In general, the Smoluchowski equation for P_3 depends on higher order moments that involve the conditional distributions of the remaining $N-1$ particles. To render the equation tractable, in writing down Eq. 4.1-4.3, we have opted for a closure relation which neglects those higher order contributions. A more detailed derivation of these equations from a general Smoluchowski equation is provided in the Supplementary. All derivatives and gradients with respect to the colloidal position are defined as $\nabla \equiv \nabla_\mathbf{r}$ for notation simplicity.

The three particle probability may be defined in terms of conditional probabilities, $P_3 = P_1 P_{1|1}(\mathbf{r}, t) P_{1|2}(\mathbf{h}, t|\mathbf{r})$. Here, $P_{1|1}(\mathbf{r}, t)$ is the probability of finding the quiescent colloid at position $\mathbf{r}$ and $P_{1|2}(\mathbf{h}, t|\mathbf{r})$ is the probability of finding a depletant particle at

$\mathbf{h}$ given that the quiescent colloid is at $\mathbf{r}$. These conditional probabilities are related to physical quantities by $P_{1|1}(\mathbf{r},t) = n_c g(\mathbf{r},t)$ and $P_{1|2}(\mathbf{h},t|\mathbf{r}) = n_b \rho(\mathbf{h},t|\mathbf{r})$ where g is the colloidal pair distribution function and ρ is the local depletant structure about the colloidal pair in a particular configuration. We observe that the colloid pair distribution satisfies mass conservation, $n_c \int g(\mathbf{r},t) d\mathbf{r} = 1$. Additionally, because hard particles cannot overlap, Eq.4.1 satisfies no-flux boundary conditions at hard-disk contact distances, $\mathbf{n}_h \cdot \langle \mathbf{j}_3 - \mathbf{j}_1 \rangle_3 = 0$ at $h = d_{cb} = (d_c + d_b)/2$ and $\mathbf{n}_r \cdot \langle \mathbf{j}_2 - \mathbf{j}_1 \rangle_3 = 0$ at $r = d_c$. At infinitely large separations, the depletants and colloid are uniformly distributed and uncorrelated, $g, \rho \to 1$ for $r, h \to \infty$.

The integration of Eq. 4.1 over the last depletant degree of freedom results in a two-body Smoluchowski equation:

$$\frac{\partial g(\mathbf{r},t)}{\partial t} + \nabla \cdot \langle \mathbf{j}_2 - \mathbf{j}_1 \rangle_2 = 0 \tag{4.4}$$

where the average colloidal flux is:

$$\begin{aligned} \langle \mathbf{j}_2 - \mathbf{j}_1 \rangle_2 = &-\mathrm{Pe}_c \alpha^{-1} \mathbf{e}_\mathbf{x} g - \alpha^{-1} \\ &\left[\nabla g + g \nabla V_{12}/(k_B T) + g n_b \int \rho \nabla V_{23}/(k_B T) d\mathbf{h} \right]. \end{aligned} \tag{4.5}$$

The contributions on the RHS of the average colloidal flux are advection, Brownian, colloid-probe interactions, and an average bath-mediated colloid-probe interaction. We observe that Eq. 4.4- 4.5 are standard, pair-level equations which have been used extensively and successfully to model distributions of mono-disperse colloidal suspensions. The main focus of our present work is the last term in Eq. 4.5. In most prior works, ρ is not explicitly solved for and the last term in Eq. 4.5 is instead approximated by an equilibrium pair potential such as DLVO theory or Asakura-Oosawa depletion interactions

even while the system is driven out of equilibrium, as we will briefly describe in the next section.

4.2.3 Asakura-Oosawa (AO) Model

The Smoluchowski equation we have previously laid out constitutes a framework in which the bath flux is explicitly considered when deriving the suspension microstructure. The microstructural deformation becomes a function of both the nonequilibrium driving strength and the relative rate of diffusive transport between the colloid and the bath, $g(\mathbf{r}, t; \mathrm{Pe}_\mathrm{c}, \alpha)$. To validate our framework and demonstrate its advantages in nonequilibrium settings, we will compare our approach to a conventional treatment which uses an equilibrium depletion potential. In this treatment, rather than considering the nonequilibrated local bath distribution ρ, we impose a quasi-static, attractive pair potential between the colloid and the probe, such that their relative motion is governed by a two-body Smoluchowski equation:

$$\frac{\partial g(\mathbf{r}, t)}{\partial t} + \nabla \cdot \langle \mathbf{j}_2 - \mathbf{j}_1 \rangle_2 = 0 \tag{4.6}$$

where the relative translational flux is given by:

$$\langle \mathbf{j}_2 - \mathbf{j}_1 \rangle = -\mathrm{Pe}_\mathrm{c} g \mathbf{e}_x - g \nabla V_\mathrm{AO}/(k_\mathrm{B}T) - \nabla g. \tag{4.7}$$

Observe that Eq. 4.7 is identical to Eq. 4.5 if the pairwise forces obtained from the equilibrium approximations satisfy $\nabla V_\mathrm{AO} = \nabla V_{12}/(k_\mathrm{B}T) + n_\mathrm{b} \int \rho \nabla V_{23}/(k_\mathrm{B}T) d\mathbf{h}$. Physically, this means that the AO potential is equivalent to a local bath distribution which instantaneously equilibrates about the two larger colloids.

At equilibrium, the structure of a homogeneous mixture gives the effective depletion

potential, which in two dimensions is given by:[40, 41]

$$V_{AO}/(k_{\mathrm{B}}T) = -\, n_{\mathrm{b}} d_{\mathrm{b}}^2 \frac{(1+a)^2}{2} \left[\cos^{-1}\left(\frac{r}{(1+a)d_{\mathrm{b}}}\right) - \left(\frac{1}{1+a}\frac{r}{d_{\mathrm{b}}}\right)\sqrt{1-\left(\frac{1}{1+a}\frac{r}{d_{\mathrm{b}}}\right)^2} \right] \tag{4.8}$$

where $a = d_{\mathrm{c}}/d_{\mathrm{b}}$. Similar to Eq. 4.1, Eq.4.6 satisfies no-flux boundary conditions $\mathbf{n}\cdot\langle \mathbf{j}_2 - \mathbf{j}_1\rangle_3 = 0$ at contact $r = d_{\mathrm{c}}$ and uniform distributions far away, $g \to 1$ for $r \to \infty$. Under Eq. 4.6- 4.7, the microstructural deformations do not depend on depletant transport and are purely functions of the probe driving strength, $g(\mathbf{r}, t; \mathrm{Pe}_{\mathrm{c}})$. This simple theory serves as a check of our framework at equilibrium, and we will now consider its utility out of equilibrium.

4.2.4 Regular Perturbation

In general, Eqs. 4.1- 4.3 are difficult to evaluate numerically because the equation depends on both the bath and colloidal degrees of freedom. However, if the depletant diffuses much faster than the colloid in the suspension, then the drag parameter α is much greater than 1. In this limit, we can solve Eq. 4.1 using a regular perturbation expansion $\rho \approx \rho_0 + \alpha^{-1}\rho_1 + \mathcal{O}(\alpha^{-2})$ and $g \approx g_0 + \alpha^{-1} g_1 + \mathcal{O}(\alpha^{-2})$ (see Supplemental). This is analogous to a multiple-timescale approach, where the effective depletion force at equilibrium may be obtained by expanding the time variable in terms of the "fast" timescale of the depletants.[42, 43, 44] Physically, the regular perturbation implies that the probe is driven at strengths comparable to thermal fluctuations of the depletant (i.e. the linear response limit). Note that the driving strength is not necessarily weak relative to colloidal diffusion, which allows us to measure the nonlinear microrheology of the colloidal suspension.

Using regular perturbation, we evaluate Eq. 4.1- 4.3 at steady state and find that the leading order depletant distribution is a Boltzmann distribution $\rho_0 \sim e^{-(V_{23}+V_{13})/k_{\mathrm{B}}T}$, consistent with our assumption that the fastest timescale in the system is depletant diffusion. The leading order colloidal distribution obeys:

$$\nabla \cdot \left[\mathrm{Pe_c} g_0 \mathbf{e_x} + \nabla g_0 + g_0 \nabla V_{12}/(k_{\mathrm{B}}T) - g_0 n_{\mathrm{b}} \int \rho_0 \nabla V_{23}/(k_{\mathrm{B}}T) d\mathbf{h} \right] = 0. \tag{4.9}$$

The first three terms on the left-hand side of Eq. 4.9 are identical to Squires and Brady for a monodisperse bath,[39] while the last term is a potential of mean force between the probe and colloid due to the presence of depletants. We have further derived the governing equations for the $\mathcal{O}(\alpha^{-1})$ contribution in the Supplementary. All equations are numerically evaluated for an arbitrarily large 2-dimensional area using FreeFEM++, an open-source finite element package.[45]

4.2.5 Viscosity Calculation

When driven at a constant velocity $\mathbf{U}_{\mathrm{c}}$ through the suspension, the probe experiences both a Newtonian drag due to the solvent and an additional, effective drag due to interactions with other particles. For arbitrary pairwise interactions, it may be shown that the average force felt by the probe is given by:

$$\langle \mathbf{F}_1 \rangle = 3\pi\eta d_{\mathrm{c}} \mathbf{U}_1 + n_{\mathrm{c}} \int g \nabla V_{12} d\mathbf{r} + n_{\mathrm{c}} n_{\mathrm{b}} \int g \int \rho \nabla_{\mathbf{h}} V_{13} d\mathbf{h} d\mathbf{r}. \tag{4.10}$$

The additional viscosity due to particle interactions may be related to Stokesian-type drag, $\langle \mathbf{F}_1 \rangle = 3\pi\eta_{\mathrm{eff}} d_{\mathrm{c}} \mathbf{U}_{\mathrm{c}}$. One may compute the effective viscosity increment $\Delta\eta_{\mathrm{eff}} =$

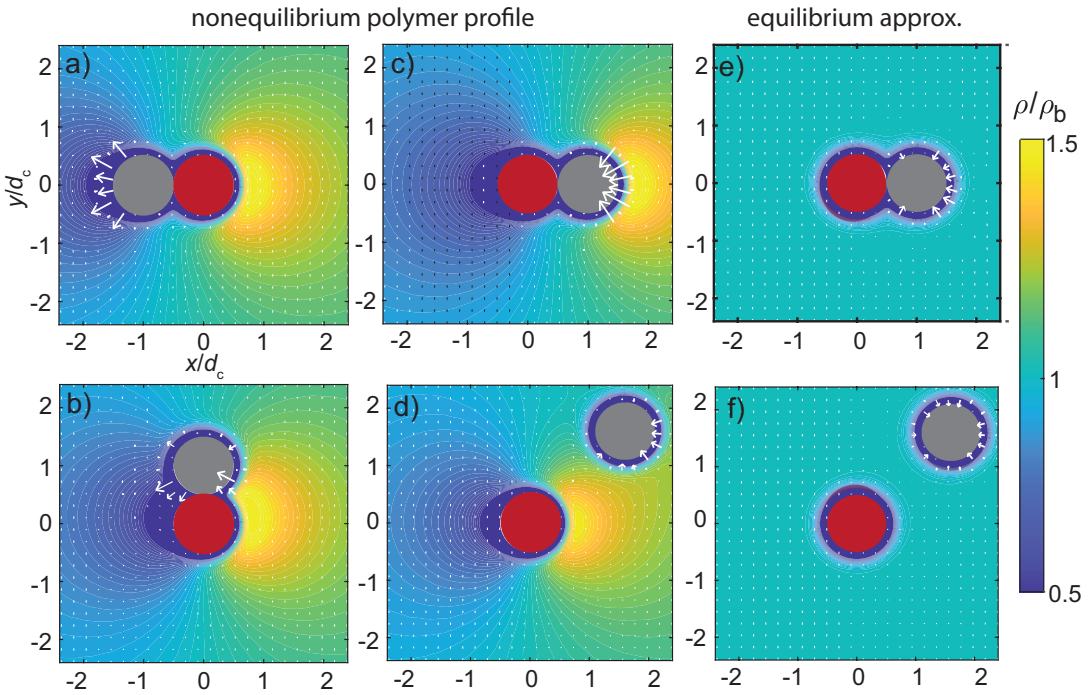

Figure 4.2: Local depletant density transmits an effective nonequilibrium force between the quiescent colloid and the driven probe. Perturbation solutions of Eq. 4.1 for the steady-state conditional depletant density $\rho(\mathbf{h}|\mathbf{r})$ are shown given that the quiescent colloid (gray) is spatially fixed at a position (a) behind, (b) alongside, (c) in front of, and (d) far from the probe (red). The quiescent colloid disrupts the depletant dipole organization when in vicinity of the probe. White arrows indicate the the local, nonequilibrium force field on the quiescent colloid, weighted by the local polymer density, $\rho\nabla_{\mathbf{h}}V^{\mathrm{tot}}$. The drag parameter is $\alpha = \zeta_c/\zeta_d = 5$ and driving force is $\mathrm{Pe}_c = 10$. For contrast, equilibrium distributions ρ_{eq} are shown when the quiescent colloid is (e) close to and (f) far from the probe, where excluded area overlap results in a classic 2D depletion force. Comparison of panels (e)-(f) with panels (c)-(d) show dramatic differences in the distribution of the depletants around the colloids, demonstrating the inaccuracies of applying the equilibrium AO depletion potential in nonequilibrium processes.

$\eta_{\mathrm{eff}} - \eta$, which is given by:

$$\frac{\Delta\eta_{\mathrm{eff}}}{\eta} = \frac{n_c}{3\pi\eta d_c U_1}\int g\nabla V_{12}d\mathbf{r} + \frac{n_c n_b}{3\pi\eta d_c U_1}\int g\int \rho\nabla_{\mathbf{h}}V_{13}d\mathbf{h}d\mathbf{r}. \tag{4.11}$$

The first term on the right-hand side of Eq. 4.11 exactly matches the result arrived at by Squires and Brady for a monodisperse suspension, except that, in this case, the pair

distribution g is modified by depletant motion.[39] The second term contributes an $\mathcal{O}(n_\mathrm{b})$ effect and accounts for contributions arising from hard-disk collisions with the depletant particles. One may rationalize this depletant concentration dependence by considering that the AO interaction potential also scales with n_b. We note that our multi-scale model naturally redices to the AO pair interaction in the limit of rapidly-equilibrating depletants.

In the next section, we detail our simulation protocol and our choice of particle pair interactions.

4.2.6 Brownian Dynamics Simulations

To validate our Smoluchowski theory, we perform 2-dimensional BD simulations of the aforementioned viscous suspension of two colloidal particles suspended in a bath of smaller depletants. In the simulation, one probe colloid moves deterministically with constant velocity $U_\mathrm{c}\mathbf{e}_x$ such that in the reference frame of the probe, the quiescent colloid and depletants follow the overdamped Langevin equation of motion:

$$\frac{\Delta r_i}{\Delta t} = \zeta^*_{\mathrm{c,b}}\Big(\underbrace{\nabla_i V^{\mathrm{tot}}}_{\text{interactions}} + \underbrace{\mathbf{F}^{\mathrm{B}}_i}_{\text{Brownian}} \Big) - \underbrace{\mathrm{Pe}_\mathrm{b}\mathbf{e}_x}_{\text{advection}} \tag{4.12}$$

where $\gamma^*_{\mathrm{c,b}} = \zeta_{\mathrm{c,b}}/\zeta_\mathrm{c}$ is the non-dimensional drag of the corresponding depletant or colloid. Here, we have nondimensionalized time by the diffusive timescale of the depletants $d_\mathrm{b}^2/D_\mathrm{b}$, positions by the depletant size d_b, and all forces by $k_\mathrm{B}T/d_\mathrm{b}$. The implicit solvent induces a stochastic force $\mathbf{F}^{\mathrm{B}}_i$ satisfying zero mean and variance consistent with the fluctuation-dissipation theorem. In all simulations, we have chosen a time step, $\Delta t = 10^{-4}$.

All interparticle forces are derived from a global potential:

$$V^{\mathrm{tot}} = \sum_{\mathrm{i}} \sum_{\mathrm{j}} V_{\mathrm{ij}}(r_{\mathrm{ij}}) \tag{4.13}$$

where V_{ij} is the pairwise potential between particles i and j at separation r_{ij}. As mentioned earlier, we neglect any depletant-depletant interactions and assume that they are ideal. To model the short-ranged repulsion between particles, we impose the Weeks-Chandler-Anderson (WCA) potential between all remaining particles pairs:[46]

$$V_{ij}(r_{ij}) = \begin{cases} 4\epsilon \left[\left(\frac{d}{r}\right)^{12} - \left(\frac{d}{r}\right)^{6} \right] + \epsilon & (r \leq 2^{\frac{1}{6}} d) \\ 0 & (r > 2^{\frac{1}{6}} d) \end{cases} \tag{4.14}$$

where d is the hard-disk contact distance, either d_{c} for probe-colloid pair interactions V_{12} or d_{cb} for colloid-depletant and probe-depletant interactions ($V_{12}, V_{2j\neq 1,2}$), and ϵ is set as the thermal energy scale.

From the simulations, we compute the average drag force on the probe due to collisions with the quiescent colloid ($i = 2$) and with the depletants ($i = 3, ..., N + 2$),

$$\langle \mathbf{F}_1 \rangle = -\frac{1}{2} \sum_{i=2}^{N+2} \nabla_i \left(\frac{V^{\mathrm{tot}}(r_{1i})}{k_{\mathrm{B}} T} \right). \tag{4.15}$$

which is related to the effective viscosity, as shown earlier.

All simulations are performed in a periodic box with dimensions $L_x \times L_y$. For weak driving ($\mathrm{Pe_c} \leq 1$), we choose $L_x = 22\sigma$ and $L_y = 18\sigma$. Under moderate driving ($\mathrm{Pe_c} > 1$), a trailing wake begins to form behind the microrheological probe. Therefore, we have increased the x-dimension in those simulations to $L_x = 180\sigma$ to ensure that results are not biased by finite size effects. Based on box dimensions, we have chosen the number of bath particles to maintain a high bulk density of ideal depletants, $n_{\mathrm{b}} =$

$0.63 d_{\mathrm{b}}^{-2}$. To obtain sufficient statistics, we simulate 30-100 independent realizations and sample statistics for up to $10,000$ depletant Brownian timescales and $200-2000$ colloidal Brownian timescales to ensure steady state spatial distributions. All simulations are performed using HOOMD-blue, a GPU-accelerated simulation package.[47]

4.3 Results

4.3.1 Nonequilibrium Depletant Microstructure

To understand how the depletant bath modifies colloidal interactions out of equilibrium, we first consider the micro-scale depletant structure around the colloidal pair. For an ideal, monodisperse suspension, it is well known that bath particles at steady state adopt a symmetric diffusive dipole, $\rho(h,\theta) = 1 + \mathrm{Pe_b}\cos(\theta)/(2h^2)$, where bath particles accumulate in front of the probe and deplete from the back.[39] In Fig. 4.2, we solve Eq. 4.1 using the regular perturbation approach and present contour plots of the local depletant distribution ρ at a moderate driving strength $\mathrm{Pe_c} = 1$ and $\alpha = d_{\mathrm{c}}/d_{\mathrm{b}} = 5$, corresponding to the SES limit. In the presence of the second quiescent colloid, the depletant structure exhibit significant deviations from the monodisperse limit when the colloid is in the viscinity of the probe. When the quiescent colloid is upstream of the probe (where it spends a nontrivial amount of time), the depletants accumulate about the quiescent colloid (Fig. 4.2c). On the other hand, when the quiescent colloid is located downstream, depletants exclude behind the quiescent colloid (Fig. 4.2a). In both cases, the quiescent colloid effectively "shields" the probe, mitigating the retardation felt by the probe from collisions with the bath. When colloids are separated far apart (Fig. 4.2d), the dipole is recovered and the depletant density around the colloid is generally undisturbed. These near-field deviations have not been previously predicted by equilibrium-based assump-

tions such as dynamic superpositioning approximation (DSA), which do not preserve the internal force transmissions between the particles [48].

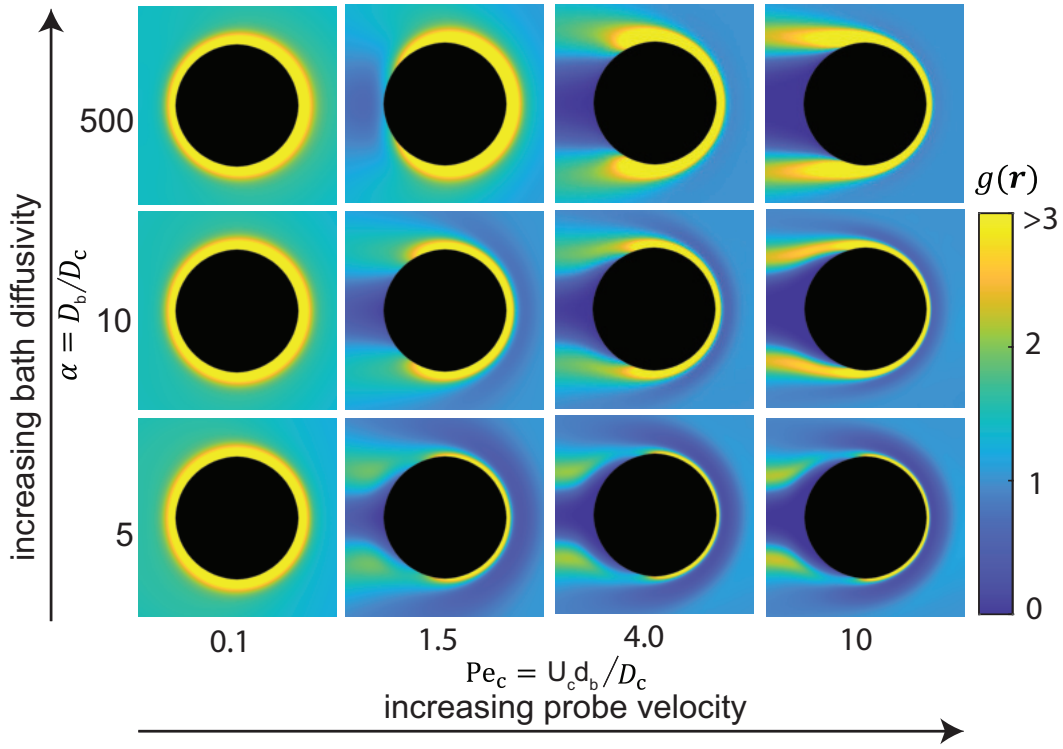

Figure 4.3: Competition between depletant and colloidal timescales governs the steady-state colloidal microstructure out of equilibrium. Contour plots for the colloidal pair distribution $g(r)$, obtained from numerically solving the steady-state solution to Eq. 4.1, are shown for a range of depletant diffusivities α and probe velocities $\mathrm{Pe_c}$. The colloidal distribution at low-$\mathrm{Pe_c}$ is uniformly isotropic while a boundary layer and trailing wake develops at higher $\mathrm{Pe_c}$. An upstream ring of depleted density develops at higher $\mathrm{Pe_c}$ and low α due to nonequilibrium depletant interactions.

In Fig. 4.2e-f, we verify our theory at equilibrium by showing that the depletant microstructure follows a Boltzmann-like distribution, where the depletant density is unity except inside the excluded volume shells around each colloid. While the net depletion force at equilibrium points along the centers-of-mass axis between the probe and the colloid, the nonequilibrium depletion force is generally anisotropic and acts along the direction of probe motion (Fig. 4.2a-d). Given their strength and anisotropy, we expect that these nonequilibrium forces will significantly impact the colloidal microstructure.

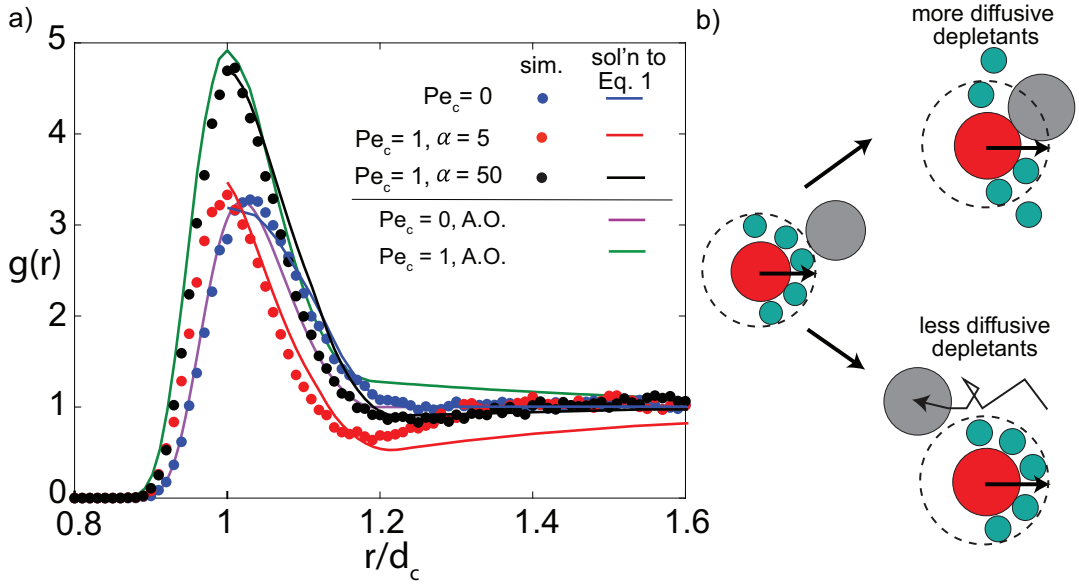

Figure 4.4: Depletant diffusivity modulates a short-range attraction and longer-range repulsion between colloidal pairs out of equilibrium. (a) The steady colloidal pair distribution function $g(r)$ upstream of the microrheological probe is plotted as a function of the center-center separation between the colloids. Filled markers are BD simulations for the equilibrium suspension (blue) and the nonequilibrium suspension ($\mathrm{Pe_c} = 1$) in a less diffusive (red) and more diffusive (black) depletant bath. Solid curves are solutions to Eq. 4.1. The Asakura-Oosawa approximation is also plotted for $\mathrm{Pe}_c = 0$ (purple) and $\mathrm{Pe}_c = 1$ (green). Numerical solutions are truncated at Eq. 4.1 $\mathrm{r/d}_c$ where we have imposed a no flux condition. (b) Proposed mechanism of how depletant diffusivity modulates colloidal microstructure. Given their spatial diffusivity, depletants either quickly relax and move away to allow colloids to come into contact (top) or form a boundary layer that shields the probe (bottom).

Our results demonstrate that the distribution of depletants is no longer Boltzmann in the presence of forcing, and that the nonequilibrium distributions of the depletants play a key role in dictating the effective forces on the colloids. As we discuss in further detail below, the equilibrium AO potential cannot be used in general to accurately predict the colloidal distributions driven out of equilibrium.

4.3.2 Colloidal Microstructure

Given the local, flow-dependent organization of depletant particles, we now consider how the colloidal scale microstructure is modified by these nonequilibrium depletion interactions. In Fig. 4.3, we show contour plots for the steady colloidal pair distribution function $g(r)$ for a range of depletant diffusivities α and probe driving strengths $\mathrm{Pe_c}$. Surprisingly, we find that the moderate to high Pe behavior is sensitive to the diffusivity of the bath. In a monodisperse suspension under strong shear, one expects microstructural deformations to collapse to a convection-diffusion boundary layer of width $d_\mathrm{c}\mathrm{Pe_c}^{-1}$ at sufficiently high $\mathrm{Pe_c}$. For a bidisperse suspension, while the boundary layer is recovered in the limit of very diffusive depletants, an upstream ring of essentially no colloidal density with width d_b appears for lower values of α. This is indicative of repulsive interactions between the colloid and probe beyond their hard sphere-like interaction. In a previous study, this repulsion has been attributed to the interactions facilitated by depletants, but the mechanism by how this occurred was not clear.[48] When the probe velocity is comparable to the depletant timescale, the depletant-mediated nonequilibrium force tends to push the colloid away from the leading probe front and towards the back. (Supplementary Fig. 1) Due to the local dipolar distribution of depletants, this nonequilibrium depletion force tends to be stronger and longer-ranged than the equilibrium force, which disappears once $|\mathbf{r}| > d_\mathrm{c} + d_\mathrm{b}$.

Additionally, we observe that the low-$\mathrm{Pe_c}$ behavior is isotropically enriched, indicative of an isotropic attractive depletion potential.

To quantitatively consider the colloidal microstructure at moderate $\mathrm{Pe_c}$, we perform BD simulations and average over a representative cross-section of $g(r)$ along the upstream direction. In Fig. 4.4a, we show both the equilibrium distribution and a nonequilibrium distribution at a driving velocity $\mathrm{Pe_c} = 1$ for low ($\alpha = 5$) and high ($\alpha = 50$) depletant diffusivities. We plot our BD simulations, theoretical solutions to Eq. 4.1-Eq. 4.3, and results using the equilibrium approximation with an AO depletion potential (Eq. 4.6-Eq. 4.8). Overall, BD simulations show good agreement with the theoretical solutions. The equilibrium $g(r)$ enriches at contact $r/d_c = 1$ due to AO-type depletion interactions and is independent of α. This is consistent with the intuition that the equilibrium distribution is only dependent on the potential energy landscape and is insensitive to transport properties such as diffusivity. We note that the hard sphere contact distance limits our multi-scale solutions to $r/d_c \geq 1$.

Interestingly, two distinct characteristics arise when the probe is driven. First, when depletants diffuse much faster than the colloid ($\alpha = 50$), the peak in $g(r)$ at $r/d_c = 1$ increases by roughly 60% due to advection-driven accumulation along the upstream direction. On the other hand, when the depletants are diffusing at similar speeds as the colloidal particle ($\alpha = 5$), the enrichment at contact is significantly dampened. The AO theory accurately predicts the former but has no way of accounting for the latter. We rationalize that because the AO model assumes a quasi-equilibrium distribution of bath particles, it therefore relies on having a large separation of timescales, or large α. Secondly, while one would expect uniform attraction (i.e. $g(r) \geq 1$ for all r) for depletion interactions, we find that the suspension shows a slight decrease near $r/d_c \sim 1.2$ when the bath is less diffusive. This decrease corresponds to the repulsive ring that was qualitatively observed in Fig. 4.3. AO-theory fails to predict the repulsive behavior, which

must be purely a nonequilibrium effect. We verified that deviations of the theoretical results from simulations at $r \geq 1.2$ are attributed to indirect correlations between the ideal depletants, which exist at high number densities in our simulations. We note that this depletant-mediated repulsion is distinct from the pairwise repulsion in colloidal systems coated with interacting, end-tethered polymer brush layers [14]. While the polymer brush system results in a entropic repulsion at equilibrium, the depletant-mediated pair interaction is purely attractive at equilibrium and the repulsion is a nonequilibrium effect associated with the intrinsic depletant timescale.

In Fig. 4.4b, we propose one mechanism by which the competition of diffusive timescales helps to facilitate this short-range attraction and longer-range repulsion. When the probe is driven at moderate strengths, the particles in suspension accumulate (i.e. spend a non-negligible amount of time) at the upstream surface of the probe. When the colloid is separated from the probe by a layer of smaller bath particles, a more diffusive bath is less perturbed by flow and allows the colloid to make contact with the probe by diffusing away from the interstitial region. As such, an AO-type depletion attraction is maintained because depletants are able to reach local equilibrium. However, when the bath depletants diffuse comparably as fast as the colloid, the depletants accumulate more strongly upstream and therefore requires more work for the colloid to penetrate. In this case, the quiescent colloid effectively "sees" a larger probe of diameter $d_\mathrm{c} + d_\mathrm{b}$.

Finally, using our theoretical framework, we have derived a nonequilibrium potential of mean force between colloidal particles which may be more practical for many-body systems under assumptions of weak driving forces (see Supplemental for detailed derivation). Unlike the equilibrium pairwise interaction V_eq which is equivalent to AO and is purely isotropic, the nonequilibrium pair interaction V_neq depends specifically on the nonequilibrium protocol and may also depend on the relative angle of separation. In Fig. 4.5, we show the nonequilibrium and equilibrium pair interactions along the lead-

ing front of the probe for $\alpha = 10$ and colloid Péclet Number $Pe_c = 0.1$. In agreement with Fig. 4.4, $V_{\rm neq}$ contributes a repulsive barrier peaked at $r/d_{\rm c} = 1.2 = 1 + d_{\rm b}/d_{\rm c}$, corresponding exactly to the hard-sphere contact distance between two colloids plus the diameter of the depletant particle. This further supports our mechanism that depletants help to shield the probe from the quiescent colloid along the leading front. Additionally, this repulsive potential decays slowly due to the long-ranged, dipolar perturbation to the local depletant structure. Finally, because the equilibrium depletion interaction is purely attractive but limited to $r/d_{\rm c} < 1.2$, the net pair interaction demonstrates short-ranged attraction for $r/d_{\rm c} < 1.2$ and long-ranged repulsion at $r/d_{\rm c} > 1.2$.

4.3.3 Microviscosity

Microstructural deformations about the probe are of central importance to the rheology of the suspension. In this section, we will study how the microviscosity responds to the competition between various relaxation timescales in our system. We first consider the depletant contribution to the microviscosity by isolating the second term on the right-hand side of Eq. 4.11, $\Delta\eta_{\rm b}/\eta = k_{\rm B}T(3n_{\rm c}n_{\rm b}\pi\eta d_{\rm c}U_{\rm c})^{-1}\int g\int \nabla_{\mathbf{h}}V_{31}d\mathbf{h}d\mathbf{r}$ which accounts for the direct interactions between the probe and the depletant. Notice that this term has been normalized by $n_{\rm c}$ and $n_{\rm b}$ since it depends on the depletant distribution in the presence of the two colloids. When considering depletant viscosity contributions, the depletant Péclet number, $\mathrm{Pe_b}$, is the relevant nondimensional quantity that measures the driving force relative to depletant Brownian relaxation.

In Fig. 4.6, we plot $\Delta\eta_{\rm b}/\eta$ as a function of $\mathrm{Pe_b}$ for three different depletant ratios. Interestingly, we observe that the depletant microviscosity contribution increases at weak driving and is sensitive to α. When the depletants relax much faster than the colloids ($\alpha = 50$), the probe experiences a lower drag at low shear rates ($\mathrm{Pe_b} \ll 1$), approaching

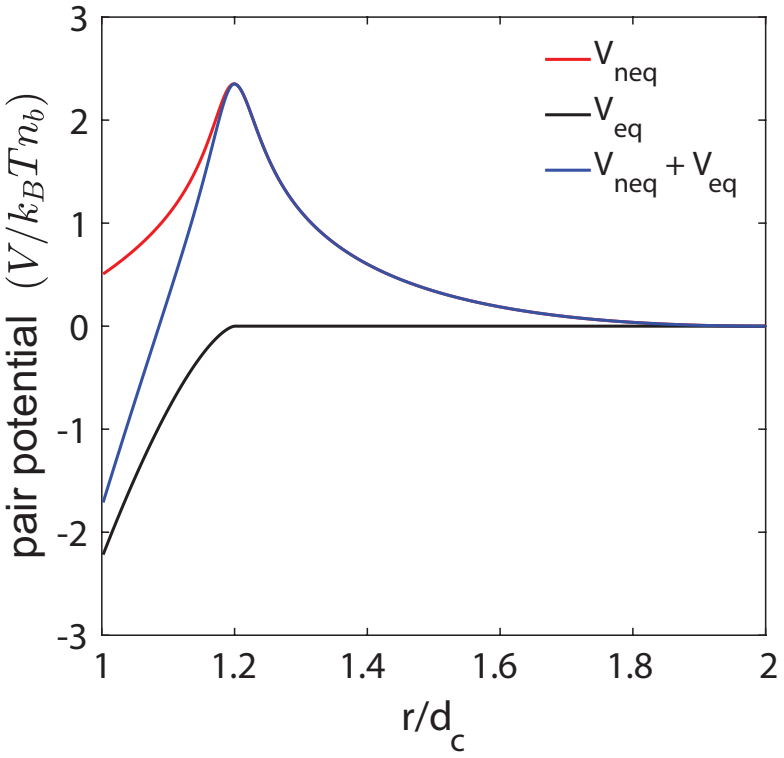

Figure 4.5: Nonequilibrium, depletant-mediated interaction potential between colloidal particles. The nonequilibrium pair potential $V_{\rm neq}$(red), Asakura-Oosawa potential $V_{\rm eq}$ (black), and the net pair interaction (blue) are plotted for large diffusivity ratio $\alpha = 10$ and small colloid Péclet Number $Pe_c = 0.1$.

a linear-response plateau at $\mathrm{Pe_b} \to 0$. As probe velocity increases, the viscosity rises to a maximum before monotonically shear-thinning at moderate to high $\mathrm{Pe_b}$. This is markedly different from the typical shear-thinning behavior of hard sphere suspensions. We offer one explanation for this mild shear thickening effect. When α is large, perturbations to the colloidal structure relax much slower and $g(r)$ adopts a boundary layer of $\mathcal{O}(\mathrm{Pe_c})$ with a width of $\mathcal{O}(\mathrm{Pe_c})$.[39] The accumulation of the colloid upstream of the probe prohibits depletants from contacting the probe, as demonstrated earlier in Fig. 4.2c, and reduces $\Delta\eta_\mathrm{b}/\eta$ at low $\mathrm{Pe_b}$. As $\mathrm{Pe_b}$ increases, the colloid is decreasingly able to screen out the depletants, thereby leading to an increase in the depletant contribution to the microviscosity. On the other hand, when $\alpha = 5$, $\mathrm{Pe_b}$ is comparable to $\mathrm{Pe_c}$, the viscosity remains relatively flat because both colloids and depletants relax on similar timescales. At moderate to high shear, all cases shear thin. Predicting this limit requires solving the coupled set of Eq. 4.1- 4.3 without using regular perturbation, which can only predict a diffusive dipole. Numerical evaluation of those equations are challenging as they require accounting for both colloidal and depletant degrees of freedom simultaneously. Although we do not have a theoretical prediction in this limit, we speculate that the shear thinning behavior is likely similar to that of a monodisperse suspension. At high $\mathrm{Pe_c}$, we observe a prolonged shear decay towards zero in the simulations, which has been previously observed. This shear thinning has been attributed to the inaccuracy of the continuous WCA pair potential in approximating hard spheres in the limit of high probe velocity.[48]. For hard sphere suspensions, it has been previously found that the high shear viscosity flattens toward a finite value as particles accumulate within a convection-diffusion boundary layer of width $\mathrm{Pe_c^{-1}}$, within which the accumulation grows as $O(\mathrm{Pe_c})$.[39].

Finally, we consider the colloidal contribution to the microviscosity by defining $\Delta\eta_\mathrm{c}/\eta = k_\mathrm{B}T(3n_\mathrm{c}\pi\eta d_\mathrm{c}U_\mathrm{c})^{-1}\int g\nabla V_{21}d\mathbf{r}$ from Eq. 4.11. In Fig. 4.7, we plot $\Delta\eta_\mathrm{c}/\eta$ as a function of

the the colloidal Péclet number, $\mathrm{Pe_c}$ for three different drag ratios. Here, we observe a shear thinning behavior throughout and a small increase in the linear response viscosity for decreasing depletant diffusivity. This is consistent with the intuition that reducing bath diffusivity also increases the relaxation time of the colloid and therefore increases the work required to distort the colloidal microstructure. At higher driving strengths, both theory and simulations indicate a shear thinning behavior, which is commonly observed in monodisperse hard-sphere suspensions without hydrodynamic interactions or contact friction. BD simulations at weak driving suffer strongly from thermal noise and are omitted for clarity.

When both contributions are combined, the overall viscosity of the suspension remains shear thinning despite the mild shear-thickening effect of the bath. However, caution should be taken when directly comparing Fig. 4.6- 4.7 for two reasons. First, the x-axis of Fig. 4.7 is offset from Fig. 4.6 by a factor of α due to the definition of the Péclet numbers, $\mathrm{Pe_c} = \alpha \mathrm{Pe_b}$. Second, $\Delta\eta_\mathrm{b}/\eta$ is normalized by the bath density while $\Delta\eta_\mathrm{c}/\eta$, which also contains contributions from the depletants, is not. Therefore, while the viscosity is seemingly dominated by the colloid, in reality the depletants indirectly influence $g(r)$, and $\Delta\eta_\mathrm{c}/\eta$ become a weaker contribution once n_b has been scaled out. Finally, for a fixed depletant area fraction $\phi_\mathrm{b} = n_\mathrm{b}\pi(d_\mathrm{b}/2)^2$, we observed similar qualitative features and note that the microviscosity contributions generally decrease as depletant size increases. (Supplementary Fig. 2) Because the depletant number density n_b must decrease to maintain a constant area fraction, both the equilibrium and nonequilibrium depletant interactions will weaken. Therefore, we hypothesize our analysis holds in the limit of small depletants which are present in high concentration.

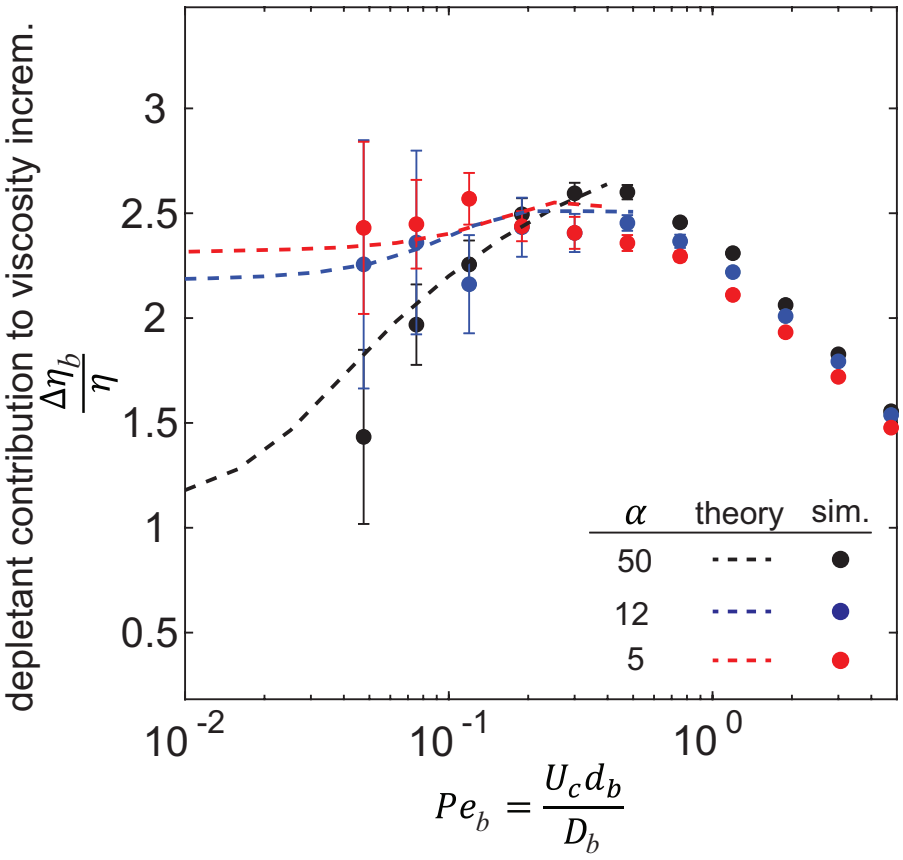

Figure 4.6: Viscosity contribution from depletant bath mildly shear thickens at lower shear and shear thins at higher shear. The depletant bath viscosity is plotted as a function of the depletant Péclet number Pe_b for a varying drag ratios of $\alpha = 5$ (red), $\alpha = 12$ (blue), and $\alpha = 50$ (black). Theory predictions from Eqs. 4.1-4.3 are only shown for $\mathrm{Pe_b} \leq 0.2$, when the regular perturbation expansion is valid.

4.4 Discussion

Understanding the material properties of multicomponent suspensions is important for many applications. In this work, we have developed a framework that accurately predicts the structure and microrheology of a bidisperse suspension of colloids and depletants. We found that the colloidal microstructure is generally sensitive to the bath diffusion timescale and that equilibrium-based approximations toward a depletion pair potential is only reliable in certain limits. While we focus our case study on a dilute suspension with at most pairwise interactions, in denser systems one may opte to apply a

mean-field treatment. For a hard sphere suspension, one may incorporate the mean field external potential, which is derived based on the free energy of the system and depends on higher order virial coefficients, into Eq. 4.1 to account for density effects. [40].

We also qualify our results by observing that beyond a certain flow strength, the polymer may undergo a coil to stretch transition, resulting in stresses that grow nonlinearly with the flow rate.[49] When the deformation time exceeds that of the internal relaxation time of the depletant polymer chain, polymers no longer adopt a random-walk chain and can become elastically stretched. In such cases, the polymeric bath may be better treated as a continuous, viscoelastic fluid instead of hard sphere particles. Previous works have used well-established models such as Giselkus or Oldroyd-B to describe the fluid suspension.[50, 51, 52] In such cases, the fluid disturbances due to the particles alone may give rise to shear thickening effects, in the absence of hydrodynamic interactions or frictional effects.[52] In Brownian Dynamics simulations, one could explicitly model internal chain dynamics by representing the polymer as a Kremer-Grest bead spring model.[53] We leave the detailed analysis of such systems to future work.

Although we have not accounted for hydrodynamic interactions, fluid effects play an important role in modifying the rheology and microstructure of colloidal suspensions.[4, 3] Our theory may accommodate near-field hydrodynamic functions as a first step towards including fluid-mediated interactions. Additionally, effects such as roughness and friction between particle surfaces may contribute to shear thickening at higher flow strengths.[8, 9, 10, 11] We note that our simulations, which measures correlated motion between the probe and anther colloid in a depletant bath, bear similarities with multiparticle microrheology techniques, where the relative motion of multiple probes allows the measurement of collective drift or characterization of material heterogeneities. [54, 55]

We conclude with a discussion of the potential applications of our model. Although

we have provided the simplest case of depletion interactions facilitated by repulsive, hard disks, future work may look into other types of small particles such as ahesive colloids coated by single-stranded DNA[56, 57, 58] or particles stabilized by electrostatic interactions.[14] Furthermore, AO or DLVO potentials are commonly used to model colloidal systems that undergo kinetic arrest and gelation.[24, 26, 27, 59, 60, 61, 62] The micromechanism we have identified in this work may shed light on the limited applicability of static pair interactions in these nonequilibrium systems. Our framework may also be used to predict other material properties. For example, one may measure viscoelasticity by performing oscillatory shear rheology,[63, 64, 65] for which a microscopic theory that accurately predicts the unsteady microstructure and the material moduli of multicomponent suspensions is still lacking. Finally, understanding the interplay between various relaxation timescales in systems of colloidal scale is broadly relevant for a variety of biological systems, including deformable particles[66] and biological cell surfaces where proteins laterally rearrange cell-cell contact.[67]

4.5 Supplemental

4.5.1 Smoluchowski Equation derivation

We begin with a general Smoluchowski equation governing the total probability density $P_{\mathrm{N+2}}(\mathbf{x}_1, ..., \mathbf{x}_{\mathrm{N+2}}, t)$:

$$\frac{\partial P_{\mathrm{N+2}}}{\partial t} + \sum_{i=1}^{\mathrm{N+2}} \nabla_i \cdot \mathbf{j}_i = 0. \tag{4.16}$$

Here, $i = 1$ refers to the probe, $i = 2$ is the quiescent colloid, and $i = 3, ..., N + 2$ are the N depletant particles. We will refer to all particle positions relative to the probe particle, $\mathbf{r}_i = \mathbf{x}_i - \mathbf{x}_1$. Using chain rule, all derivatives are taken with respect to the relative coordinate r_i, and the absolute position of the probe does not matter. The

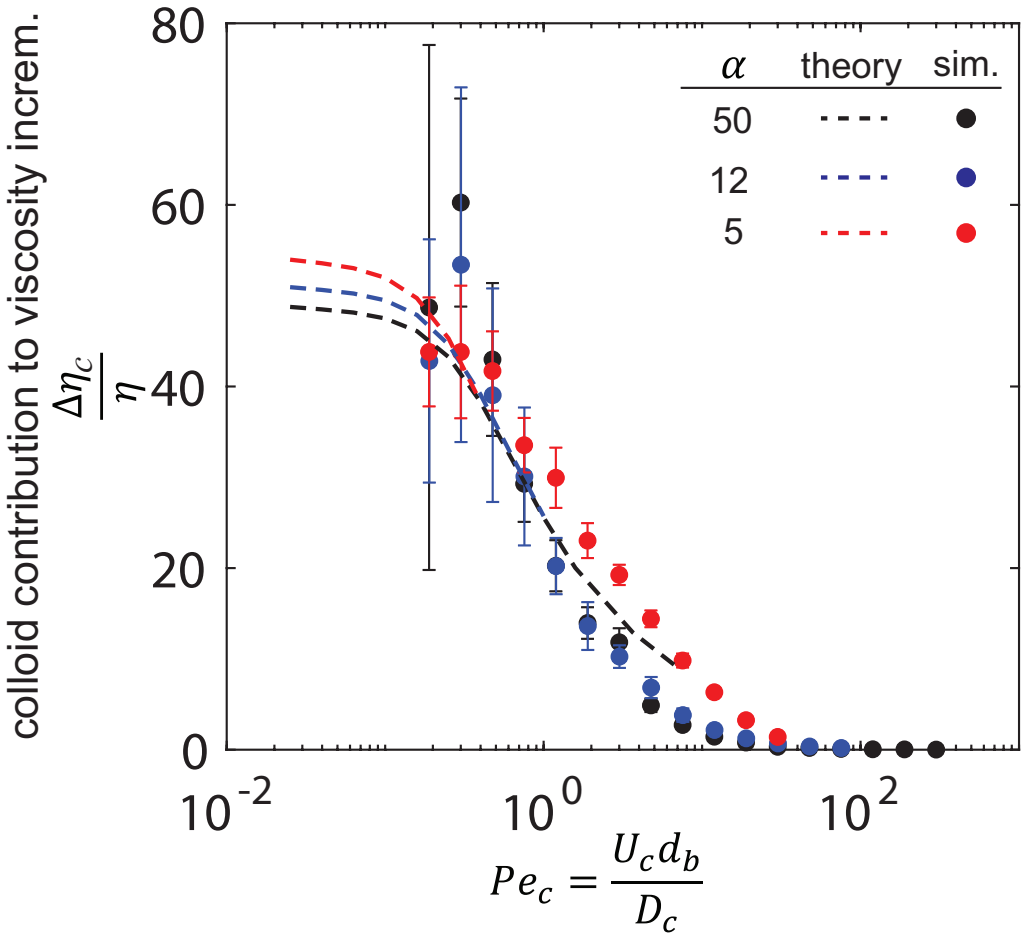

Figure 4.7: Viscosity contribution from quiescent colloid shear thins. The viscosity due to interactions with the quiescent colloid is plotted as a function of the colloidal Péclet number $\mathrm{Pe_c}$ for three drag ratios: $\alpha = 5$ (red), $\alpha = 12$ (blue), and $\alpha = 50$ (black). Theory predictions from Eqs. 4.1- 4.3 are only shown for $\mathrm{Pe_c} \leq \alpha$, when the regular perturbation expansion is valid.

relative particle translational flux is given by $\mathbf{j}_i = (\mathbf{j}_i - \mathbf{j}_1) = \mathbf{U}_i P_{\mathrm{N}}$ where $\mathbf{U}_i$ is the particle velocity.

In a suspension, particles move under the action of external forces $\mathbf{F}^{\mathrm{ext}}$, interparticle forces $\mathbf{F}^{\mathrm{P}}$, and entropic or thermal forces $k_{\mathrm{B}}T\nabla \ln\, P_{\mathrm{N}+2}$, such that the particle velocity may be expressed as:

$$\mathbf{U}_i = \sum_{j=1}^{\mathrm{N}+2} [\mathbf{M}_{ij} \cdot (\mathbf{F}_j^{\mathrm{ext}} + \mathbf{F}_j^{\mathrm{P}}) - \mathbf{D}_{ij} \cdot \nabla_j \ln\, P_N] \tag{4.17}$$

The hydrodynamic mobility tensor, $\mathbf{M}_{ij} = (k_{\mathrm{B}}T)^{-1}\mathbf{D}_{ij}$, couples a force exerted on particle j to the velocity of particle i, where $\mathbf{D}_{ij}$ is the diffusion coefficient. Neglecting hydrodynamic interactions, the diffusivity is isotropic and constant, such that $\mathbf{M}_{ij} = \delta_{ij}\zeta_{ij}^{-1}$. The drag coefficients for colloids and depletants are given by ζ_{c} and ζ_{b}, respectively.

We observe that the many-body probability density P_{N+2} can be re-expressed as a product of conditional probabilities or distributions, $P_1 P_{1|1} P_{1|2} ... P_{1|N+1}$. By definition, $P_{1|n}$ is the conditional probability of finding the $n+1$-th particle given the positions of the previous n particles.

Assuming the depletant particles are statistically homogeneous and indistinguishable, we integrate Eq. 4.16- 4.17 over the $N-1$ depletant particles:

$$\frac{\partial (P_{1\text{—}1} P_{1\text{—}2})}{\partial t} + \nabla \cdot \langle \mathbf{j}_2 - \mathbf{j}_1 \rangle_3 + \nabla_{\mathbf{h}} \cdot \langle \mathbf{j}_3 - \mathbf{j}_1 \rangle_3 = 0 \tag{4.18}$$

where the averaged colloidal and depletant fluxes are given by:

$$\langle \mathbf{j}_2 - \mathbf{j}_1 \rangle_3 = -\mathbf{U}_1 P_{1|1} P_{1|2} + \int \left[\mathbf{M}_{22} P_{\mathrm{N}+1\text{—}1} \cdot \mathbf{F}_2^P - \mathbf{D}_{22} \cdot \nabla P_{\mathrm{N}+1\text{—}1} \right] d\mathbf{r}_4 ... d\mathbf{r}_{\mathrm{N}+2} \tag{4.19}$$

and:

$$\langle \mathbf{j}_3 - \mathbf{j}_1 \rangle_3 = -\mathbf{U}_1 P_{1—1} P_{1—2} + \int \left[\mathbf{M}_{33} P_{\mathrm{N}+1—1} \cdot \mathbf{F}_3^P - \mathbf{D}_{33} \cdot \nabla_{\mathbf{h}} P_{\mathrm{N}+1—1} \right] d\mathbf{r}_4 ... d\mathbf{r}_{\mathrm{N}+2}. \quad (4.20)$$

Note that $P_{1|1}(\mathbf{r}, t)$ is the probability of finding the quiescent colloid at position $\mathbf{r}$ and $P_{1|2}(\mathbf{h}, t|\mathbf{r})$ is the probability of finding a depletant particle at $\mathbf{h}$ given that the quiescent colloid is at $\mathbf{r}$. To be consistent with the main text, we have re-defined the quiescent colloid position as $\mathbf{r} = \mathbf{r}_2$ and the depletant degree of freedom as $\mathbf{h} = \mathbf{r}_3$ for clarity. Furthermore, indices on gradients with respect to $\mathbf{r}$ have been omitted. Note that $P_{\mathrm{N}+2} = P_{\mathrm{N}+1—1} P_1$ and that the absolute position of the probe, P_1, does not matter.

We will now consider the relative colloidal flux. Replacing the interparticle forces with derivatives of the log of the equilibrium Boltzmann distribution, $\mathbf{F}_i^P = -\nabla_i V^{\mathrm{TOT}} \sim k_{\mathrm{B}} T \nabla_i \ln P_{\mathrm{N}+1—1}^{\mathrm{eq}}$, we obtain:

$$\langle \mathbf{j}_2 - \mathbf{j}_1 \rangle_3 = -\mathbf{U}_1 P_{1—1} P_{1—2} + \int \left[\mathbf{D}_{22} \cdot P_{\mathrm{N}+1—1} \nabla \ln \frac{P_{\mathrm{N}+1—1}^{\mathrm{eq}}}{P_{\mathrm{N}+1—1}} \right] d\mathbf{r}_4 ... d\mathbf{r}_{\mathrm{N}+2} \quad (4.21)$$

Substitution of this expansion into Eq. 4.16 results in the BBGKY hierarchy of equations, which quickly becomes analytically intractable for many particles. A closure is sought by diluteness of the bath particles, replacing $(P_{\mathrm{N}+1—1}^{\mathrm{eq}})/(P_{\mathrm{N}+1—1})$ with $(P_{1|1}^{\mathrm{eq}} P_{1|2}^{\mathrm{eq}})/(P_{1|1} P_{1|2})$ as all neglected terms are $O(n_{\mathrm{b}})$. From this, we obtain:

$$\langle \mathbf{j}_2 - \mathbf{j}_1 \rangle_3 = -\mathbf{U}_1 P_{1—1} P_{1—2} + \mathbf{D}_{22} \cdot P_{1—1} P_{1—2} \nabla \ln \left[\frac{P_{1—1}^{\mathrm{eq}} P_{1—2}^{\mathrm{eq}}}{P_{1—1} P_{1—2}} \right]. \quad (4.22)$$

Analogously, the depletant flux becomes:

$$\langle \mathbf{j}_3 - \mathbf{j}_1 \rangle_3 = -\mathbf{U}_1 P_{1—1} P_{1—2} + \mathbf{D}_{33} \cdot P_{1—1} P_{1—2} \nabla_{\mathbf{h}} \ln \left[\frac{P_{1—1}^{\mathrm{eq}} P_{1—2}^{\mathrm{eq}}}{P_{1—1} P_{1—2}} \right]. \quad (4.23)$$

We apply the Boltzmann relation, $P_{1|1}^{\mathrm{eq}} \sim e^{-V_{21}/k_{\mathrm{B}}T}$ and $P_{1|2}^{\mathrm{eq}} \sim e^{-(V_{31}+V_{32})/k_{\mathrm{B}}T}$ where the two-body potentials are defined $V_{21} = V_{21}(\mathbf{r})$, $V_{31} = V_{31}(\mathbf{h})$, and $V_{32} = V_{32}(\mathbf{h}-\mathbf{r})$. The fluxes reduce to:

$$\langle \mathbf{j}_2 - \mathbf{j}_1 \rangle_3 = \\ -\mathbf{U}_1 P_{1—1} P_{1—2} - \mathbf{D}_{22} \cdot [(\nabla P_{1—1} P_{1—2}) + P_{1—1} P_{1—2} \nabla V_{21}/(k_{\mathrm{B}}T) + P_{1—1} P_{1—2} \nabla V_{32}/(k_{\mathrm{B}}T)] \tag{4.24}$$

$$\begin{aligned} \langle \mathbf{j}_3 - \mathbf{j}_1 \rangle_3 &= -\mathbf{U}_1 P_{1—1} P_{1—2} \\ &- \mathbf{D}_{33} \cdot [(\nabla_{\mathbf{h}} P_{1—1} P_{1—2}) + P_{1—1} P_{1—2} \nabla_{\mathbf{h}} V_{31}/(k_{\mathrm{B}}T) + P_{1—1} P_{1—2} \nabla_{\mathbf{h}} V_{32}/(k_{\mathrm{B}}T)] \end{aligned} \tag{4.25}$$

we can relate these conditional probabilities physical quantities by $P_{1|1} = n_{\mathrm{c}} g$ and $P_{1|2} = n_{\mathrm{b}} \rho$ where g is simply the colloidal pair distribution function and ρ may be thought of as the local depletant structure about the colloidal pair.

The particle velocity is given by $\mathbf{U}_1 = U_{\mathrm{c}} \mathbf{e}_{\mathbf{x}}$. We chose to nondimensionalize all distances by the depletant size d_{b}, energy by $k_{\mathrm{B}}T$, and time by the Brownian timescale of the depletant particle, $\tau_{\mathrm{c}}^{b} = d_{\mathrm{b}}^2/D_{\mathrm{b}}$. We recover a final nondimensional Smoluchowski equation, averaged over $N-1$ depletants:

$$\frac{\partial (g\rho)}{\partial t} + \nabla \cdot \langle \mathbf{j}_2 - \mathbf{j}_1 \rangle_3 + \nabla_{\mathbf{h}} \cdot \langle \mathbf{j}_3 - \mathbf{j}_1 \rangle_3 = 0 \tag{4.26}$$

where

$$\langle \mathbf{j}_2 - \mathbf{j}_1 \rangle_3 = -\mathrm{Pe}_{\mathrm{c}} \alpha^{-1} \mathbf{e}_{\mathbf{x}} g\rho - \alpha^{-1} \left[\nabla (g\rho) + g\rho \nabla V_{21}/(k_{\mathrm{B}}T) + g\rho \nabla V_{32}/(k_{\mathrm{B}}T) \right] \tag{4.27}$$

$$\langle \mathbf{j}_3 - \mathbf{j}_1 \rangle_3 = -\mathrm{Pe_c}\alpha^{-1}\mathbf{e_x}g\rho - \left[\nabla_{\mathbf{h}}(g\rho) + g\rho\nabla_{\mathbf{h}}V_{31}/(k_{\mathrm{B}}T) + g\rho\nabla_{\mathbf{h}}V_{32}/(k_{\mathrm{B}}T)\right]. \quad (4.28)$$

We have defined the relative drag ratio $\alpha = D_{\mathrm{b}}/D_{\mathrm{c}}$ and two Péclet Numbers, $\mathrm{Pe_c} = U_{\mathrm{c}}d_{\mathrm{b}}/D_{\mathrm{c}}$ and $\mathrm{Pe_b} = \mathrm{Pe_c}/\alpha = U_{\mathrm{c}}d_{\mathrm{b}}/D_{\mathrm{b}}$ as documented in the main text.

Finally, we may proceed to integrate Eq. 4.26 over the last depletant particle to obtain the governing equation for the quiescent colloid distribution about the probe:

$$\frac{\partial g}{\partial t} + \nabla \cdot \langle \mathbf{j}_2 - \mathbf{j}_1 \rangle_2 = 0 \quad (4.29)$$

where the effective colloidal flux is:

$$\langle \mathbf{j}_2 - \mathbf{j}_1 \rangle_2 = -\mathrm{Pe_c}\alpha^{-1}\mathbf{e_x}g - \alpha^{-1}\left[\nabla g + g\nabla V_{21}/(k_{\mathrm{B}}T) + gn_{\mathrm{b}}\int \rho\nabla V_{32}/(k_{\mathrm{B}}T)d\mathbf{h}\right]. \quad (4.30)$$

Eq. 4.26-4.28 and Eq. 4.29-4.30 are our main results in this section. In particular, this Smoluchowski framework is general to any three-particle system and may be used for a number of different species and particle interactions. In the next section, we proceed to solve these equations using a perturbation expansion approach.

4.5.2 Regular Perturbation Expansion

In the limit where the Brownian timescale of the colloid is very small relative to the Brownian timescale of the smaller depletants ($\alpha \ll 1$), we may perform the following regular perturbation expansion for both the colloidal and depletant structures about the probe.

We expand $g \approx g_0 + \alpha^{-1}g_1 + \alpha^{-2}g_2 + O(\alpha^{-3})$ and $\rho \approx \rho_0 + \alpha^{-1}\rho_1 + \alpha^{-2}\rho_2 + O(\alpha^{-3})$.

Observe that, by mass conservation, we have $n_c \int \rho_0 d\mathbf{h} = 1$, $\int \rho_{i\neq 0} d\mathbf{h} = 0$ and similarly for g.

At steady state, the leading order terms of Eq. 4.26-4.28 become:

$$\nabla_{\mathbf{h}} \cdot [\nabla_{\mathbf{h}} \rho_0 + \rho_0 \nabla_{\mathbf{h}} (V_{31}/(k_B T) + V_{32}/(k_B T))] = 0 \tag{4.31}$$

Which is simply diffusion under an external field. From this, it is clear that the diffusion of depletants, under our assumption that $\alpha \ll 1$, is the fastest process in the system. Solved with no flux boundary conditions at contact and unity at $\mathbf{h} \to \infty$, the solution takes on a simple Boltzmann form, $\rho_0 \sim e^{(-V_{32}-V_{31})/(k_B T)}$.

At $O(\alpha^{-1})$, the g_0 governing equation may be obtained from expanding Eq. 4.29- 4.30 as:

$$\nabla \cdot \left[\mathrm{Pe}_c g_0 \mathbf{e_x} + \nabla g_0 + g_0 \nabla V_{21}/(k_B T) - g_0 n_c \int \rho_0 \nabla V_{32}/(k_B T) d\mathbf{h} \right] = 0. \tag{4.32}$$

The first three terms on the RHS exactly match active microrheology of a probe navigating through a monodisperse bath whereas the last term is the potential-of-mean-force contribution from depletants. Because ρ_0 follows a Boltzmann distribution, we find that $\int n_c \int \rho_0 \nabla V_{32}/(k_B T) d\mathbf{h}$ is analogous to an Asakura-Oosawa type depletion potential.

Additionally, at $O(\alpha^{-1})$, it may be shown through that Eq. 4.26- 4.28 becomes:

$$\nabla \rho_0 \cdot \langle \mathbf{j}_2 - \mathbf{j}_1 \rangle_3^0 + \nabla_{\mathbf{h}} \cdot [\mathrm{Pe}_c \mathbf{e_x} g_0 \rho_0 - g_0 \rho_1 \nabla_{\mathbf{h}} (V_{31} + V_{32}) - g_0 \nabla_{\mathbf{h}} \rho_1] = 0 \tag{4.33}$$

where the $\langle \mathbf{j}_2 - \mathbf{j}_1 \rangle_3^0$ is equal to the terms in the bracket of Eq. 4.32. We observe that the leading order colloidal flux and colloidal microstructure now contribute to the ρ_1 solution, effectively coupling the local depletant motion to the slower colloidal motion.

Finally, once ρ_1 is known, it is then possible to obtain g_1 through the $O(\alpha^{-2})$ expansion

of Eq. 4.29- 4.30:

$$\nabla \cdot \left[\mathrm{Pe_c} g_1 \mathbf{e_x} + \nabla g_1 + g_1 \nabla V_{21}/(k_\mathrm{B}T) - g_1 n_\mathrm{c} \int \rho_1 \nabla V_{32}/(k_\mathrm{B}T) d\mathbf{h} \right] = 0. \tag{4.34}$$

4.5.3 Microviscosity Calculation

We follow the approach of Squires and Brady, beginning with the total drag force experienced by the probe colloid due to external driving, thermal forces, and interactions with the particles in suspension:

$$\mathbf{F}_1 = \mathbf{M}_{11}^{-1} \cdot U_1 \mathbf{e_x} + \sum_{j=1}^{\mathrm{N+2}} \mathbf{M}_{11}^{-1} \cdot (\mathbf{D}_{1j} - \mathbf{D}_{11}) \cdot \nabla_j \ln(P_{\mathrm{N+2}}/P_{\mathrm{N+2}}^{\mathrm{eq}}) \tag{4.35}$$

Neglecting hydrodynamic interactions as we have done before, we have:

$$\mathbf{F}_1 = k_\mathrm{B}T D_{11}^{-1} U_1 \mathbf{e_x} - \sum_{j=2}^{\mathrm{N+2}} k_\mathrm{B}T \nabla_j \ln(P_{\mathrm{N+2}}/P_{\mathrm{N+2}}^{\mathrm{eq}}). \tag{4.36}$$

Similar to the previous section, we use a diluteness closure to replace $P_{N+2}/P_{N+2}^{\mathrm{eq}}$ with $(P_{1|1}P_{1|2})/(P_{1|1}^{\mathrm{eq}}P_{1|2}^{\mathrm{eq}})$. We now perform an average over $N-1$ depletant particles,

$$\langle \mathbf{F}_1 \rangle_3 = \int \mathbf{F}_1 P_{N-1|3} d\mathbf{r}_4 ... d\mathbf{r}_{\mathrm{N+2}} \tag{4.37}$$

which recovers:

$$\langle \mathbf{F}_1 \rangle_3 = k_\mathrm{B}T D_{11}^{-1} U_1 \mathbf{e_x} P_{1|1} P_{1|2} - k_\mathrm{B}T P_{1|1} P_{1|2} \nabla \ln \left[\frac{P_{1|1}P_{1|2}}{P_{1|1}^{\mathrm{eq}} P_{1|2}^{\mathrm{eq}}} \right] - k_\mathrm{B}T P_{1|1} P_{1|2} \nabla_\mathbf{h} \ln \left[\frac{P_{1|1}P_{1|2}}{P_{1|1}^{\mathrm{eq}} P_{1|2}^{\mathrm{eq}}} \right]. \tag{4.38}$$

Substituting the Boltzmann relations, $P^{\rm eq}_{1|1} \sim e^{-V_{21}/k_{\rm B}T}$ and $P^{\rm eq}_{1|2} \sim e^{-(V_{31}+V_{32})/k_{\rm B}T}$, we obtain:

$$\begin{aligned}\langle \mathbf{F}_1 \rangle_3 =& k_{\rm B}T D_{11}^{-1} U_1 \mathbf{e_x} P_{1|1} P_{1|2} - k_{\rm B}T \nabla (P_{1|1} P_{1|2}) + \\ & k_{\rm B}T P_{1|1} P_{1|2} \nabla (V_{21} + V_{32}) - k_{\rm B}T \nabla_{\mathbf{h}} (P_{1|1} P_{1|2}) + k_{\rm B}T P_{1|1} P_{1|2} \nabla_{\mathbf{h}} (V_{31} + V_{32})\end{aligned} \tag{4.39}$$

Integrating over the last depletant and the colloidal degrees of freedom($\int ...d\mathbf{h}d\mathbf{r}$) and noting that $n_{\rm b} \int \rho d\mathbf{h} = 1$, we obtain:

$$\begin{aligned}\langle \mathbf{F}_1 \rangle_1 =& k_{\rm B}T D_{11}^{-1} U_1 \mathbf{e_x} + k_{\rm B}T n_{\rm c} \int g \nabla V_{21} d\mathbf{r} + k_{\rm B}T n_{\rm c} n_\rho \int g \int \rho \nabla V_{32} d\mathbf{h} d\mathbf{r} \\ & + k_{\rm B}T n_{\rm c} n_\rho \int g \int \rho \nabla_{\mathbf{h}} V_{32} d\mathbf{h} d\mathbf{r} + k_{\rm B}T n_{\rm c} n_\rho \int g \int \rho \nabla_{\mathbf{h}} V_{31} d\mathbf{h} d\mathbf{r}\end{aligned} \tag{4.40}$$

Note that the third and fourth terms on the RHS cancel since $\nabla V_{32}(\mathbf{r}-\mathbf{h}) = \nabla_{\mathbf{h}} V_{32}(\mathbf{r}-\mathbf{h})$. Nondimensionalizing forces by $k_{\rm B}T/d_{\rm b}$ and distances by $d_{\rm b}$, we obtain the final form of the force velocity relation for the probe particle:

$$\langle \mathbf{F}_1 \rangle_1 = k_{\rm B}T D_{11}^{-1} d_{\rm b} U_1 \mathbf{e_x} + n_{\rm c} k_{\rm B}T \int g \nabla V_{21} d\mathbf{r} + n_{\rm c} n_\rho k_{\rm B}T \int g \int \rho \nabla_{\mathbf{h}} V_{31} d\mathbf{h} d\mathbf{r} \tag{4.41}$$

Eq. 4.41 is the main result of this section and highlights the $O(n_{\rm b})$ contribution to the drag force of the probe. Using this expression, the effective viscosity η due to particles in suspension may be expressed through a Stokes relation, $\langle \mathbf{F}_1 \rangle_1 = 3\pi \eta_{\rm eff} d_{\rm c} \mathbf{U}_{\rm c}$. We find that the effective viscosity of the suspension is given by:

$$\eta_{\rm eff} = \eta + \frac{n_{\rm c} k_{\rm B}T}{3\pi d_{\rm c} U_{\rm c}} \int g \nabla V_{21} d\mathbf{r} + \frac{n_{\rm c} n_{\rm b} k_{\rm B}T}{3\pi d_{\rm c} U_{\rm c}} \int g \int \rho \nabla_{\rm h} V_{31} d\mathbf{h} d\mathbf{r}. \tag{4.42}$$

From this, the relative microviscosity increment, $\Delta\eta_{\rm eff}/\eta = (\eta_{\rm eff} - \eta)/\eta$ is exactly as given in the main text.

To further elucidate this interaction, we subsitute our perturbation expansion of ρ and group terms in order of their contributions:

$$\eta_{\text{eff}} = \eta + \frac{n_{\text{c}} k_{\text{B}} T}{3\pi d_{\text{c}} U_{\text{c}}} \int g \nabla V_{21} d\mathbf{r} + \frac{n_{\text{c}} n_{\text{b}} k_{\text{B}} T}{3\pi d_{\text{c}} U_{\text{c}}} \int g \int \rho_0 \nabla_{\text{h}} V_{31} d\mathbf{h} d\mathbf{r} + \alpha^{-1} \frac{n_{\text{c}} n_{\text{b}} k_{\text{B}} T}{3\pi d_{\text{c}} U_{\text{c}}} \int g \int \rho_1 \nabla_{\text{h}} V_{31} d\mathbf{h} d\mathbf{r}. \tag{4.43}$$

Note that the second and third terms on the RHS of this equation both contain isotropic forces and are leading order contributions to the microviscosity.

4.5.4 Nonequiilbrium pair potential

We will now show how the Smoluchowski framework enables the calculation of an effective, out-of-equilibrium pair potential between the colloidal particles which may be used in many-body systems. We will consider colloids and depletants as perfect hard-spheres that experience no pairwise interactions ($V_{31}, V_{32} = 0$) except a no-flux condition at contact. To make analytical progress, we assume that the driving force is much weaker relative to the diffusion of the depletant particle, allowing a second perturbation expansion in orders of Pe_{c}:

$$\begin{aligned} \rho_0 &= \rho_{0,0} + \rho_{0,1} \text{Pe}_{\text{c}} + O\left(\text{Pe}_{\text{c}}^2\right) \\ g_0 &= g_{0,0} + g_{0,1} \text{Pe}_{\text{c}} + O\left(\text{Pe}_{\text{c}}^2\right). \end{aligned} \tag{4.44}$$

Following the regular perturbation approach, $\rho_{0,0}$ is given by a Laplace equation with no-flux boundary conditions, which has the trivial solution that $\rho_{0,0}(\mathbf{h}|\mathbf{r}) = 1$ for all $|\mathbf{r}\text{-}\mathbf{h}| \geq (1 + d_{\text{c}}/d_{\text{b}})/2$ and $|\mathbf{h}| \geq (1 + d_{\text{c}}/d_{\text{b}})/2$.

Because advection is weak, the leading order equation for $g_{0,0}$ contains just the diffu-

sive and interparticle contributions:

$$\nabla \cdot \left[\nabla g_{0,0} - g_{0,0} n_{\mathrm{c}} \int \rho_{0,0} \mathbf{e}_{\mathbf{r\text{-}h}} \delta \left(|\mathbf{r\text{-}h}| - \frac{(1 + d_{\mathrm{c}}/d_{\mathrm{b}})}{2} \right) d\mathbf{h} \right] = 0. \tag{4.45}$$

The Dirac delta function originates from the hard sphere potential at contact. From a simple geometric argument, the integral range reduces to integration along the major arc length around two overlapping circles centered at the origin and $\mathbf{r}$, each with radius $1 + \frac{d_{\mathrm{c}}}{d_{\mathrm{b}}}$. The solution to Eq. 4.45 is an isotropic, Boltzmann form $g_{0,0} \sim e^{-V_{\mathrm{eq}}(r)/k_{\mathrm{B}}T}$ where V_{eq} is equivalent to the Asakura-Oosawa potential.

The governing equation for $\rho_{0,1}$ contains advective and diffusive contributions:

$$\nabla_{\mathbf{h}} \cdot [\mathrm{Pe}_{\mathrm{c}} \rho_{0,0} \mathbf{e}_{\mathbf{x}} + \nabla_{\mathrm{h}} \rho_{0,1}] = 0 \tag{4.46}$$

and satisfying no-flux boundary conditions as before. The solution is a simple dipolar distribution that is similar to active microrheology through a monodisperse bath, $\rho_{0,1} = 1 + \mathrm{Pe}_{\mathrm{c}} h_x/(2h^3)$ for all $|\mathbf{r\text{-}h}| \geq (1 + d_{\mathrm{c}}/d_{\mathrm{b}})/2$ and $|\mathbf{h}| \geq (1 + d_{\mathrm{c}}/d_{\mathrm{b}})/2$. From this, we can compute the effective force exerted by the depletants and obtain a potential of mean force by integrating the force to a position r from infinitely-far separation distances. Along the leading front of the probe, we obtain the following simplified form of the nonequilibrium potential between colloidal particles due to interactions with depletant:

$$V_{\mathrm{neq}}(r; Pe, \alpha) = \int_{\infty}^{r} \int_{\theta_1}^{\theta_2} \frac{(1 + \frac{d_{\mathrm{c}}}{d_{\mathrm{b}}}) \left[\left(1 + \frac{d_{\mathrm{c}}}{d_{\mathrm{b}}} \right) cos\theta' - H \right]}{\left[\left((1 + \frac{d_{\mathrm{c}}}{d_{\mathrm{b}}}) cos\theta' - H \right)^2 + \left((1 + \frac{d_{\mathrm{c}}}{d_{\mathrm{b}}}) sin\theta' \right)^2 \right]^{3/2}} d\theta' dH \tag{4.47}$$

where the angles θ_1 and θ_2 are the angles of intersection between the two overlapping circles described earlier. The nonequilibrium potential along the leading front is plotted in Fig. 5 of the main text.

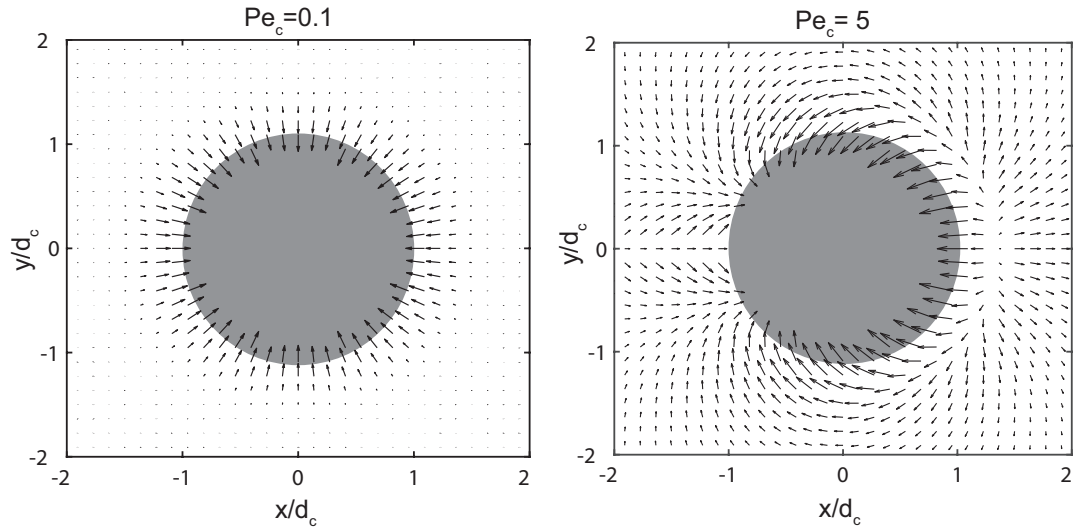

Figure 4.8: Vector plot showing theoretical calculations for the effective force field on the quiescent colloid in units of k_BT/d_b for two different probe driving strengths: $\mathrm{Pe_c} = 0.1$ (left), and $\mathrm{Pe_c} = 5$ (right). The diffusivity ratio is $\alpha = 5$ and the shaded area $|r| < \mathrm{d_c}$ represents the excluded volume due to the hard-sphere colloid-colloid interaction.

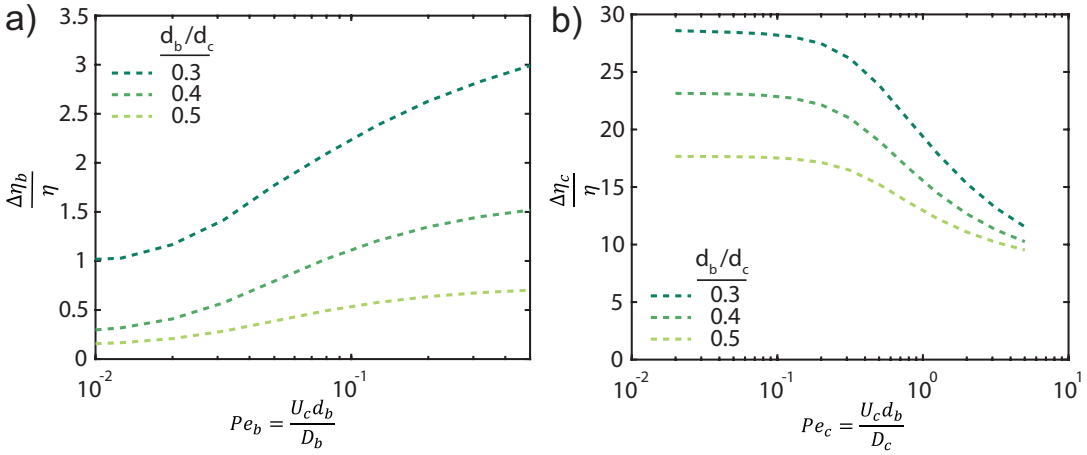

Figure 4.9: Microviscosity increments decrease for increasing depletant sizes. The depletant (a) and colloid (b) contributions to the microviscosity are shown for three different depletant-colloid size ratios.

Bibliography

[1] Jan Mewis and Norman J. Wagner. *Colloidal Suspension Rheology*. Cambridge University Press, Nov. 2011.

[2] Élisabeth Guazzelli, Jeffrey F. Morris, and Sylvie Pic. *A Physical Introduction to Suspension Dynamics*. Cambridge University Press, Nov. 2011.

[3] J. Bergenholtz, J. F. Brady, and M. Vicic. "The non-Newtonian rheology of dilute colloidal suspensions". In: *Journal of Fluid Mechanics* 456 (2002), pp. 239–275.

[4] G. K. Batchelor. "Brownian diffusion of particles with hydrodynamic interaction". In: *Journal of Fluid Mechanics* 74.1 (Mar. 1976), pp. 1–29.

[5] Jonathan Bender and Norman J. Wagner. "Reversible shear thickening in monodisperse and bidisperse colloidal dispersions". In: *Journal of Rheology* 40.5 (Sept. 1996), pp. 899–916.

[6] John R. Melrose and Robin C. Ball. "Continuous shear thickening transitions in model concentrated colloids—The role of interparticle forces". In: *Journal of Rheology* 48.5 (Sept. 2004), pp. 937–960.

[7] John F. Brady and Georges Bossis. "The rheology of concentrated suspensions of spheres in simple shear flow by numerical simulation". In: *Journal of Fluid Mechanics* 155 (June 1985), p. 105.

[8] Romain Mari et al. "Shear thickening, frictionless and frictional rheologies in non-Brownian suspensions". In: *Journal of Rheology* 58.6 (2014), pp. 1693–1724.

[9] Romain Mari et al. "Discontinuous shear thickening in Brownian suspensions by dynamic simulation". In: *Proceedings of the National Academy of Sciences of the United States of America* 112.50 (2015), pp. 15326–15330.

[10] Neil Y. C. Lin et al. "Hydrodynamic and Contact Contributions to Continuous Shear Thickening in Colloidal Suspensions". In: *Phys. Rev. Lett.* 115 (22 2015), p. 228304.

[11] Sidhant Pednekar, Jaehun Chun, and Jeffrey F. Morris. "Simulation of shear thickening in attractive colloidal suspensions". In: *Soft Matter* 13 (9 2017), pp. 1773–1779.

[12] R. A. Lionberger and W. B. Russel. "High frequency modulus of hard sphere colloids." In: *J. Rheol.* 38 (1994), pp. 1885–1908.

[13] Aditya S. Khair and John F. Brady. ""Microviscoelasticity" of colloidal dispersions". In: *Journal of Rheology* 49.6 (Nov. 2005), pp. 1449–1481.

[14] W. B. Russel, D. A. Saville, and W. R. Schowalter. *Colloidal Dispersions*. Cambridge Monographs on Mechanics. Cambridge University Press, 1989.

[15] S. M. Ilett et al. "Phase behavior of a model colloid-polymer mixture". In: *Physical Review E* 51.2 (Feb. 1995), pp. 1344–1352.

[16] A. A. Louis, R. Finken, and J. P. Hansen. "Crystallization and phase separation in nonadditive binary hard-sphere mixtures". In: *Physical Review E* 61.2 (Feb. 2000), R1028–R1031.

[17] Sho Asakura and Fumio Oosawa. “On Interaction between Two Bodies Immersed in a Solution of Macromolecules”. In: *The Journal of Chemical Physics* 22.7 (July 1954), pp. 1255–1256.

[18] A. Vrij. “Polymers at Interfaces and the Interactions in Colloidal Dispersions”. In: *Pure and Applied Chemistry* 48.4 (Jan. 1976), pp. 471–483.

[19] Björn Neu and Herbert J. Meiselman. “Depletion-Mediated Red Blood Cell Aggregation in Polymer Solutions”. In: *Biophysical Journal* 83.5 (Nov. 2002), pp. 2482–2490.

[20] Gerhard M. Artmann and Shu Chien. *Bioengineering in cell and tissue research*. Berlin, Heidelberg: Springer Berlin Heidelberg, 2008, pp. 1–693.

[21] Dmitry A. Fedosov et al. “Predicting human blood viscosity in silico”. In: *Proceedings of the National Academy of Sciences* 108.29 (July 2011), pp. 11772–11777.

[22] Zsigmond Varga and James W. Swan. “Linear viscoelasticity of attractive colloidal dispersions”. In: *Journal of Rheology* 59.5 (Sept. 2015), pp. 1271–1298.

[23] J. Bergenholtz, W. C. K. Poon, and M. Fuchs. “Gelation in Model ColloidPolymer Mixtures”. In: *Langmuir* 19.10 (May 2003), pp. 4493–4503.

[24] Zsigmond Varga et al. “Hydrodynamics control shear-induced pattern formation in attractive suspensions”. In: *Proceedings of the National Academy of Sciences* 116.25 (June 2019), pp. 12193–12198.

[25] Derek E. Huang and Roseanna N. Zia. “Sticky, active microrheology: Part 1. Linear-response”. In: *Journal of Colloid and Interface Science* 554 (Oct. 2019), pp. 580–591.

[26] M. Laurati et al. “Structure, dynamics, and rheology of colloid-polymer mixtures: From liquids to gels”. In: *The Journal of Chemical Physics* 130.13 (Apr. 2009), p. 134907.

[27] Arman Boromand, Safa Jamali, and João M. Maia. “Structural fingerprints of yielding mechanisms in attractive colloidal gels”. In: *Soft Matter* 13.2 (2017), pp. 458–473.

[28] J. Dzubiella, H. Löwen, and C. N. Likos. “Depletion Forces in Nonequilibrium”. In: *Physical Review Letters* 91.24 (Dec. 2003), p. 248301.

[29] Indira Sriram and Eric M. Furst. “Out-of-equilibrium forces between colloids”. In: *Soft Matter* 8.12 (2012), p. 3335.

[30] Yaxin Xu et al. “Dynamic interfaces for contact-time control of colloidal interactions”. In: *Soft Matter* 19.30 (2023), pp. 5692–5700.

[31] Aditya S. Khair and John F. Brady. “On the motion of two particles translating with equal velocities through a colloidal dispersion”. In: *Proceedings of the Royal Society A: Mathematical, Physical and Engineering Sciences* 463.2077 (2007), pp. 223–240.

[32] Benjamin E. Dolata and Roseanna N. Zia. “Non-equilibrium pair interactions in colloidalÂ dispersions”. In: *Journal of Fluid Mechanics* 836 (2018), pp. 694–739.

[33] Andrzej R. Altenberger, Matthew Tirrell, and John S. Dahler. “Hydrodynamic screening and particle dynamics in porous media, semidilute polymer solutions and polymer gels”. In: *The Journal of Chemical Physics* 84.9 (May 1986), pp. 5122–5130.

[34] R. I. Cukier. “Diffusion of Brownian spheres in semidilute polymer solutions”. In: *Macromolecules* 17.2 (Feb. 1984), pp. 252–255.

[35] R. J. Phillips, W. M. Deen, and J. F. Brady. "Hindered transport of spherical macromolecules in fibrous membranes and gels". In: *AIChE Journal* 35.11 (Nov. 1989), pp. 1761–1769.

[36] Brian Amsden. "Solute Diffusion within Hydrogels. Mechanisms and Models". In: *Macromolecules* 31.23 (Nov. 1998), pp. 8382–8395.

[37] John F. Brady. "The rheological behavior of concentrated colloidal dispersions". In: *The Journal of Chemical Physics* 99.1 (July 1993), pp. 567–581.

[38] John F. Brady and Michael Vicic. "Normal stresses in colloidal dispersions". In: *Journal of Rheology* 39.3 (May 1995), pp. 545–566.

[39] Todd M. Squires and John F. Brady. "A simple paradigm for active and nonlinear microrheology". In: *Physics of Fluids* 17.7 (2005), pp. 1–21.

[40] Jean Pierre Hansen and I. R. McDonald. *Theory of Simple Liquids: With Applications to Soft Matter: Fourth Edition*. Elsevier, 2013, pp. 1–619.

[41] R Castañeda-Priego, A Rodríguez-López, and J M Méndez-Alcaraz. "Depletion forces in two-dimensional colloidal mixtures". In: *Journal of Physics: Condensed Matter* 15.48 (Dec. 2003), S3393–S3409.

[42] Jaroslaw Piasecki, Lydéric Bocquet, and Jean Pierre Hansen. "Multiple time scale derivation of the Fokker-Planck equation for two Brownian spheres suspended in a hard sphere fluid". In: *Physica A: Statistical Mechanics and its Applications* 218.1-2 (1995), pp. 125–144.

[43] Lydéric Bocquet. "High friction limit of the Kramers equation: The multiple time-scale approach". In: *American Journal of Physics* 65 (1997), p. 140.

[44] L Bocquet. "From a stochastic to a microscopic approach to brownian motion". In: *Acta Physica Polonica B* 29.6 (1998), pp. 1551–1564.

[45] Frédéric Hecht and F Hecht. "New development in freefem++". In: *Journal of Numerical Mathematics* 20.0 (2012), pp. 1–14.

[46] John D. Weeks, David Chandler, and Hans C. Andersen. "Role of Repulsive Forces in Determining the Equilibrium Structure of Simple Liquids". In: *The Journal of Chemical Physics* 54.12 (Sept. 2003), p. 5237.

[47] Joshua A Anderson, Jens Glaser, and Sharon C Glotzer. "HOOMD-blue: A Python package for high-performance molecular dynamics and hard particle Monte Carlo simulations". In: *Computational Materials Science* 173 (2020), p. 109343.

[48] R Wulfert, U Seifert, and T Speck. "Soft Matter rsc.li/soft-matter-journal Nonequilibrium depletion interactions in active microrheology". In: *Soft Matter* 13 (2017), p. 9093.

[49] E. Balkovsky, A. Fouxon, and V. Lebedev. "Turbulent Dynamics of Polymer Solutions". In: *Physical Review Letters* 84.20 (May 2000), pp. 4765–4768.

[50] Donald L. Koch and G. Subramanian. "The stress in a dilute suspension of spheres suspended in a second-order fluid subject to a linear velocity field". In: *Journal of Non-Newtonian Fluid Mechanics* 138.2-3 (Oct. 2006), pp. 87–97.

[51] O. G. Harlen and Donald L. Koch. "Simple shear flow of a suspension of fibres in a dilute polymer solution at high Deborah number". In: *Journal of Fluid Mechanics* 252 (July 1993), pp. 187–207.

[52] Mengfei Yang, Sreenath Krishnan, and Eric S.G. Shaqfeh. "Numerical simulations of the rheology of suspensions of rigid spheres at low volume fraction in a viscoelastic fluid under shear". In: *Journal of Non-Newtonian Fluid Mechanics* 233 (July 2016), pp. 181–197.

[53] Kurt Kremer and Gary S. Grest. "Dynamics of entangled linear polymer melts: A molecular-dynamics simulation". In: *The Journal of Chemical Physics* 92.8 (1990), pp. 5057–5086.

[54] John C. Crocker et al. "Two-Point Microrheology of Inhomogeneous Soft Materials". In: *Physical Review Letters* 85.4 (July 2000), pp. 888–891.

[55] Todd M. Squires and Thomas G. Mason. "Fluid Mechanics of Microrheology". In: *Annual Review of Fluid Mechanics* 42.1 (Jan. 2010), pp. 413–438.

[56] A. Paul Alivisatos et al. "Organization of 'nanocrystal molecules' using DNA". In: *Nature 1996 382:6592* 382.6592 (1996), pp. 609–611.

[57] P. J. Santos, T. C. Cheung, and R. J. Macfarlane. "Assembling Ordered Crystals with Disperse Building Blocks." In: *Nano Lett.* 19 (2019), pp. 5774–5780.

[58] Chad A. Mirkin et al. "A DNA-based method for rationally assembling nanoparticles into macroscopic materials". In: *Nature 1996 382:6592* 382.6592 (1996), pp. 607–609.

[59] A Coniglio et al. "Percolation, gelation and dynamical behaviour in colloids". In: *Journal of Physics: Condensed Matter* 16.42 (Oct. 2004), S4831–S4839.

[60] Minaspi Bantawa et al. "Microscopic interactions and emerging elasticity in model soft particulate gels". In: *Journal of Physics: Condensed Matter* 33.41 (Oct. 2021), p. 414001.

[61] Yujie Jiang and Ryohei Seto. "Colloidal gelation with non-sticky particles". In: *Nature Communications* 14.1 (May 2023), p. 2773.

[62] Roseanna N Zia, Benjamin J Landrum, and William B Russel. "A micro-mechanical study of coarsening and rheology of colloidal gels: Cage building, cage hopping, and Smoluchowski's ratchet". In: *Citation: Journal of Rheology* 58 (2014), p. 1121.

[63] James W. Swan, Roseanna N. Zia, and John F. Brady. "Large amplitude oscillatory microrheology". In: *Journal of Rheology* 58.1 (Jan. 2014), pp. 1–41.

[64] J. W. Swan. "The medium amplitude oscillatory shear of semi-dilute colloidal dispersions. Part I: Linear response and normal stress differences." In: *J. Rheo.* 58 (2014), pp. 307–337.

[65] I. M. De Schepper, H. E. Smorenburg, and E. G.D. Cohen. "Viscoelasticity in dense hard sphere colloids". In: *Physical Review Letters* 70.14 (Apr. 1993), pp. 2178–2181.

[66] M. Foglino et al. "Flow of Deformable Droplets: Discontinuous Shear Thinning and Velocity Oscillations". In: *Physical Review Letters* 119.20 (Nov. 2017), p. 208002.

[67] A. E. Nel et al. "Understanding biophysicochemical interactions at the nano–bio interface." In: *Nat. Mater.* 8 (2009), pp. 542–557.

Chapter 5

Spatial heterogeneities on biological cell membranes

1. This chapter includes content from our previously published article:

1 Arnold, D. P., Xu, Y., and Takatori, S. C. "Antibody binding reports spatial heterogeneities in cell membrane organization." *Nature Communications* 2023, **14**, 2884. doi: 10.1038/s41467-023-38525-2.

Y.X. conducted the simulations, analyzed the data, and participated in the writing of the manuscript.

5.1 Introduction

Physical crowding of the cell surface glycocalyx has been shown recently to alter the biophysical properties of membranes in a manner that significantly impacts cell function. These alterations include membrane bending, stretching, and fission on reconstituted lipid bilayers [1, 2, 3, 4, 5], as well as tubulation and fission in the plasma membranes of cultured cells [6, 7]. In addition to inducing membrane deformation, cell surface crowding

also modulates the physical accessibility of surface receptors to large soluble ligands and macromolecules [8]. Experiments on reconstituted membranes with grafted synthetic polymers or purified proteins further confirm a decrease in protein binding affinity with increasing grafting density [9, 10, 11, 12]. Most clinical monoclonal antibody drugs that rely on direct effector-cell activity are known to target antigen receptors that are buried deep inside the glycocalyx, often within 10 nm from the membrane surface [13, 14], suggesting that their effectiveness may be highly dependent upon crowding near the receptor. However, there are currently no methods to characterize the piconewton-scale forces generated by the crowding of ∼10 nm cell surface proteins [15].

In addition to surface-orthogonal variations, the mammalian plasma membrane composition is also laterally-heterogeneous, with nanometer-scale protein and lipid clusters forming and dissipating on sub-second timescales [16, 15]. In giant plasma membrane vesicles (GPMVs) isolated from cells, Gurdap et al. showed that liquid-ordered membrane microdomains exclude proteins with bulky, heavily glycosylated extracellular domains [17]. Given the lateral and membrane-orthogonal heterogeneity of the glycocalyx, a complete picture of the crowding profile requires three-dimensional (3D) characterization.

While techniques like electron microscopy enable nanometer-scale characterization of the plasma membrane, the preparation process is destructive [18], leaving a need for appropriate molecular probes to study these complex, dynamic systems *in-vivo* [15]. Recently, Houser et al. [19] quantified the surface pressures on reconstituted crowded membranes by measuring the separation distance between FRET fluorophores that stretch due to steric interactions within the brush. The stretching distance in polymer brushes depends weakly on surface density, as height scales with chain density according to $h \sim n^{1/3}$ in the brush regime [20, 21] and follows even weaker scaling in the mushroom regime [22]. Therefore, the technique may lose accuracy at the crowding densities observed in physi-

ological surface densities on live cells.

In this work, we develop synthetic antigen sensors with precise spatial localization and measure the binding affinity of complimentary immunoglobulin G (IgG) monoclonal antibodies in these local crowding environments. We leverage a technique developed recently by Takatori and Son et al. [23], in which a macromolecular probe is introduced to the extracellular side of a plasma membrane to quantify the local osmotic pressure posed by the crowded cell surface via a reduction in effective binding affinity. We advance this technique by enabling spatial localization of the binding site to measure the membrane-orthogonal crowding heterogeneity on both reconstituted membranes and red blood cell (RBC) surfaces. We then reconstruct these systems in-silico, combining proteomics with molecular dynamics (MD) simulations and experiments to map RBC glycocalyx crowding with nanometer-scale spatial precision. Using targeted antigen probes, we expand our spatial resolution laterally, in the plane of the membrane, measuring differences in crowding between plasma membrane domains on live tumor cells. Our findings support the hypothesis that raft-like domains of native membranes exclude proteins with bulky extracellular domains, consistent with the findings of Gurdap et al. on GPMVs [17]. Our simple IgG binding assay to probe spatial heterogeneities on native cell membranes suggests an important role of structural complexities on glycocalyx organization.

5.2 Results

5.2.1 Synthetic antigen sensors report crowding heterogeneities with nanometer height resolution

The glycocalyx is heterogeneous in both composition and density, which vary as a function of distance from the membrane surface (henceforth "height"). Height hetero-

geneities in crowding can arise from variations in protein sizes [24, 25, 26, 27] and also from polymer brush dynamics of disordered glycoproteins like mucins in the glycocalyx [28, 29, 30, 6, 8]. To characterize the cell surface height heterogeneity, we developed a non-invasive synthetic antigen sensor that inserts into the lipid membrane using a cholesterol tag conjugated to a polyethylene glycol (PEG) linker and a fluorescein isothiocyanate (FITC) fluorophore (Fig. 5.1A). We developed a family of cholesterol-PEG-FITC sensors with varying PEG linker lengths to adjust the height of the FITC antigen presented above the membrane. After presenting the antigen sensors on the cell surface, we obtain the effective binding avidity of anti-FITC (FITC) IgG antibody as a function of antigen height.

The PEG linker enables the FITC antigen to sample a distribution of heights above the membrane, while the mean height, $\langle h \rangle$, increases with the molecular weight of PEG. We used cell surface optical profilometry (CSOP) [31] to measure $\langle h \rangle$ of the FITC antigen for sensor linker lengths of 0.5 kDa PEG (PEG0.5k), 2k, 5k, and 10k using silica beads coated with a 1,2-dioleoyl-sn-glycero-3-phosphocholine (DOPC) supported lipid bilayer (SLB). We recovered the predicted increase in $\langle h \rangle$ with molecular weight (Fig. 5.1B), suggesting that the antigen is probing different crowding microenvironments as a function of linker length.

To validate that our different sensors are probing the height heterogeneities of a crowded membrane surface, we measured FITC IgG binding to our antigen sensors on a reconstituted glycocalyx-mimetic PEG brush. Our reconstituted SLB on 4 µm silica beads included 3% 1,2 dioleoyl-sn-glycero 3 phosphoethanolamine N methoxy (polyethylene glycol) 2000] (DOPE-PEG2k) to act as a repulsive brush, with synthetic antigen sensors of a single type inserted into the outer membrane leaflet (see Materials and Methods). Beads were incubated in varying concentrations of fluorescently-labeled FITC antibodies and allowed to reach equilibrium before fluorescence intensities of beads were

collected via fluorescence microscopy. Intensities were fit to a Hill binding isotherm to calculate the dissociation constant K_{D} (see Supplementary Information). The ratio of K_D on the PEG-crowded SLB to that on a bare SLB with no PEG crowders, $K_{\mathrm{D}}/K_{\mathrm{D,0}}$, decreases toward unity as the average FITC height increases (Fig. 5.1C). The FITC antigen on our 10k antigen sensor samples the majority of its height distribution above the DOPE-PEG2k steric brush and has a FITC binding avidity that is essentially unchanged from the bare membrane value. In contrast, the 0.5k antigen sensor is buried deep inside the PEG brush and the accessibility of the FITC antigen is hindered by a factor of six (Fig. 5.1C). Our results are consistent with classical polymer brush theory, which predicts a monotonic decrease in brush monomer density with height [28] and a reduction in the effective adsorption energy of a globular protein onto a brush-coated surface [33].

Based on our results for synthetic sensors on a PEG brush surface, we hypothesized that the height-dependent avidity of IgG would also apply to protein antigens buried within a crowded surface of other membrane proteins. To investigate, we reconstituted an SLB containing 5% 1,2-dioleoyl-sn-glycero-3-[(N-(5-amino-1- carboxypentyl)iminodiacetic acid)succinyl] (DGS-NTA) and created a crowded surface of poly-histidine tagged glycoprotein, Glycophorin A (GYPA). Instead of synthetic antigen sensors, we tethered a dilute surface density of tyrosine phosphatase CD45 on the SLB among the crowded excess of GYPA. As a readout of GYPA crowding, we used CD45 antibodies that target two different epitope sites: pan-CD45 I3 epitope on the first FN3 domain ($\langle h \rangle = 2.5$ nm), and $\mathrm{R_B}$ isoform epitope C363 on the upper mucin-like domain ($\langle h \rangle = 15$ nm).

Using CSOP [31], we measured the height of an GYPA monoclonal antibody (clone HIR2) that binds to the N-terminus of GYPA, and found that the average GYPA height is ≈ 12 nm tall. Thus we expected the C363 epitope on CD45 to explore uncrowded regions above the GYPA brush, while the I3 epitope to remain buried within the brush. Indeed, the relative avidities of C363 and I3 agree with this hypothesis, as $K_{\mathrm{D}}/K_{\mathrm{D,0}}$ is ≈ 1 for

C363 while it is ≈ 1.5 for I3 (Fig. 5.1C). The consistent correlation between increasing antigen height, $\langle h \rangle$, and decreasing dissociation constant, $K_{\mathrm{D}}/K_{\mathrm{D},0}$, on both PEG and protein brushes confirms that antibody avidity is a robust metric of local crowding.

5.2.2 Macromolecular binding is a direct reporter of steric energies on crowded surfaces

In this section, we aim to obtain a direct relation between the antibody binding avidity and the local steric free energy penalty of a crowded surface. We combine polymer brush theories with coarse-grained MD simulations to obtain a mechanistic understanding of our synthetic antigen sensors and their applicability on crowded membrane surfaces.

To characterize the energy profile on the membrane, we separately simulated free antibody insertion into a surface-tethered PEG2k brush and antibody binding to surface-tethered sensors to obtain the repulsive penalty associated with crowding, ΔU, (Fig. 5.2A), and the attractive binding free energy, U_0, respectively (see Materials and Methods). We invoke the theory of Halperin [33] and hypothesize that the effective antibody binding free energy on a crowded interface, U_{net}, is a superposition of U_0 and ΔU. The bare membrane binding avidity reports the attractive enthalpic term $U_0 = k_{\mathrm{B}}T \ln K_{\mathrm{D},0}$, so that the repulsive entropic energy penalty posed by the brush is given by

$$\Delta U = U_{\mathrm{net}} - U_0 = k_{\mathrm{B}}T \ln \left(\frac{K_{\mathrm{D}}}{K_{\mathrm{D},0}} \right). \tag{5.1}$$

Antibody insertion into the brush reduces the volume available to the polymer and is entropically disfavored. This repulsive energy barrier, ΔU, is proportional to the osmotic pressure, Π, which scales with monomer volume fraction ϕ as $\Pi \sim \phi^{9/4}$ [33, 22]. The Milner, Witten, and Cates [28] self-consistent field description of a polymer brush pre-

dicts a parabolic monomer distribution, so the crowding penalty ΔU follows a stretched parabolic profile (Fig. 5.2B, see Supporting Information for analytical form). Kenworthy et al. showed experimentally that the pressure between apposite membrane-tethered PEG brushes under compression varies with distance according to a profile derived from Milner theory [34]. We therefore invoke this theory to describe the form of our PEG2k crowding penalty, which we verify using MD simulations (see Materials and Methods, Supplementary Movie S2).

The flexibility of the PEG linker in our synthetic antigen sensors causes the antibody to bind across a distribution of FITC heights for any given sensor. Thus, we define our experimentally-measured crowding free energy for a given sensor as a mean energy penalty $\langle \Delta U \rangle$, which can be predicted by weighting the FITC 1-D probability density P_{FITC} by the crowding penalty ΔU and integrating across all space:

$$\langle \Delta U \rangle = \int_0^\infty P_{\mathrm{FITC}}\left(z; \langle h \rangle\right) \Delta U\left(z\right) \mathrm{d}z. \tag{5.2}$$

To describe P_{FITC}, we invoke the continuous Gaussian chain model of a surface-tethered polymer of mean height $\langle h \rangle$ in an ideal solvent, calculating the chain-end distribution (see Supporting Information for calculations) [32]. We verified P_{FITC} with coarse-grained MD simulations of dilute surface-tethered PEG polymers, finding that the end-monomer distribution closely agrees with theory (Fig. 5.2B, Supplementary Movie S1). Numerically evaluating the integral in Eq. 5.2 for a set of PEG-FITC sensors with mean heights $\langle h \rangle$ yields matching theoretical and computational predictions for the observed crowding profile as a function of mean sensor height (Fig. 5.2C).

Recasting the data from Fig. 5.1C in the form given by Eq. 5.1 and plotting as a function of the mean sensor heights reported in Fig. 5.1B, shows quantitative agreement with the theoretical and MD profiles developed in Eq. 5.2 (Fig. 5.2C). Our experimental

and simulation data support a mechanism by which the brush sterically excludes the antibody, suggesting that our synthetic antigen sensors act as direct reporters of crowding heterogeneities with nanometer resolution.

5.2.3 Synthetic sensors validate crowding predictions based on red blood cell proteomics

After validating our experimental antigen sensors on reconstituted membranes with analytical theory and coarse-grained simulations, we sought to use theorertical and computational methods synergystically with experiments to map the extracellular crowding landscape of the human red blood cell (RBC). Since the RBC surface proteome is fully-characterized [35, 36], we identified the most abundant extracellular proteins, and estimated extracellular domain sizes (Fig. 5.3A). In particular, we identified two abundant proteins with bulky extracellular domains: anion transporter Band 3 and mucin-like sialoglycoprotein GYPA [36, 35, 37].

Using both analytical theory and coarse-grained MD simulations, we modeled the RBC glycocalyx as a bidisperse polymer brush whose extracellular crowding profile opposes the adsorption of colloids like IgG (Fig. 5.3B, Supplementary Movie S3). We acknowledge that not all cell surface biopolymers can be represented as brushes; certain glycoproteins form gel-like meshes that can restrict colloidal transport [42, 43]. However, while surface proteins may crosslink, to our knowledge the extracellular domains of GYPA and Band 3 have not been reported to do so. We used the lengths of extracellular peptides and glycans to estimate both the statistical monomer size and chain height of GYPA and Band 3 (see Supporting Information). We coarse-grained the biopolymers as simple bead-spring polymers that interact by excluded volume interactions and a bending penalty to account for additional effects like electrostatic repulsion that may alter

the polymer persistence length. Our goal in the simulations is to develop a minimal model to capture the key qualitative trends of height-dependent crowding on a crowded cell surface, but additional effects like electrostatic interactions and crosslinking of surface biopolymers may be included to improve model accuracy. We input predicted chain height and known chain grafting densities into a model that superimposed two parabolic polymer brush density profiles [28], and applied the scaling $\Delta U \sim \phi^{9/4}$ to model the repulsive energy penalty [22, 33]. Note that this simplification treats the two brushes independently, with no interactions between the two species. Thus the curve (plotted in Fig. 5.3B) has a discontinuous slope at the point at which the monomer density in the shorter brush (Band 3) is predicted to reach zero. We also developed an in-silico model of a bidisperse brush, with each protein modeled as a bead-spring polymer (see Supporting Information for coarse-graining details). Fig. 5.3B shows close agreement between the analytical and MD descriptions of the glycocalyx, with the MD crowding energy likely decaying faster because it relaxes the assumption of a strongly-stretched brush inherent to the theory of Milner, Witten, and Cates [28].

To verify our predicted z-direction crowding profile, we incubated human RBCs in our synthetic antigen sensors so that the sensors incorporated to roughly equal surface concentrations (supplemental Fig. S8). Unincorporated sensors were thoroughly washed from the bulk to prevent quenching of unbound antibody, with approximately 80% of sensors remaining bound over the course of the experiment ($\sim$1 hour). We measured the dissociation constant of anti-FITC binding to PEG0.5k, 2k, 5k, and 10k sensors, normalizing by the uncrowded $K_{\mathrm{D},0}$ on beads to find $\langle \Delta U \rangle$ (Eq. 5.1). Antibody binding increased $\approx$ 5x from the most surface-proximal (PEG0.5k) to the most membrane-distal probe (PEG10k), corresponding to the crowding free energy penalty doubling from $z =$ 6.5nm to $z = 0$ (Fig. 5.3C). The experimental crowding landscape closely tracks the theoretical and simulated free energies, weighted by the FITC distributions in Fig. 5.2B.

As a control, we also treated RBCs with neuraminidase (NA), which cleaves negatively-charged sialic acid from glycans exposed on the cell surface, confirming cleavage via a $\approx 60\%$ reduction in wheat germ agglutinin binding on the cell surface (see supporting figure S9). We found a $\approx 30\%$ reduction in crowding at the surface on NA-treated cells when compared to WT, as well as a flatter crowding profile for larger, more membrane-distal sensors (Fig. 5.3C). Given that GYPA contains $\sim$75% of RBC sialic acid, and that between one-third to one-half of sugars on its 15 O-glycosylations are sialic acid [36], this result suggests that GYPA plays a major role in mediating RBC crowding heterogeneity. This reduction in crowding is consistent with prior work by Takatori and Son et al. which showed similar reductions in crowding at the RBC surface ($h = 0$) using dextran-based sensors upon sialic acid cleavage, with NA treatment shortening the RBC glycocalyx mean height by about 30% [23]. These authors also showed simulations suggesting that the removal of charge may also play a role in de-swelling of the glycocalyx [23]. Given an approximate Debye length of 0.7 nm in phosphate buffered saline, we expect that adjacent glycan-glycan charge interactions may play a role in de-swelling the polymer brush, but expect the charges to be largely screened at the length scales of glycan-IgG interactions.

These data demonstrate that for the relatively simple RBC plasma membrane, detailed proteomics data including copy number, structure, and glycosylation of surface proteins provide a robust approximation of membrane-orthogonal crowding heterogeneity. Computational techniques like machine learning are rapidly accelerating the identification of surface proteins and glycosylation sites [44, 44, 45], and with more detailed characterization of glycan sequences and surface protein densities on the horizon, we expect that the in-silico reconstruction of more complex mammalian cells will become feasible. Mapping crowding heterogeneities on these nanometer length scales with simulations and molecular probes may reveal the accessibility of receptors based on height,

improving our understanding of signaling and optimizing drug delivery target selection.

5.2.4 Development of phase-partitioning antigen sensors to measure lateral heterogeneities in surface crowding

Lateral heterogeneities in composition of lipids, cholesterol, and proteins on plasma membranes, including lipid rafts and protein clusters, have been hypothesized to govern various physiological processes, like signal transduction, endocytosis, and membrane reorganization [46, 47, 48, 49, 50, 51, 52, 53, 54, 55]. Levental et al. showed that ordered domains on giant plasma membrane vesicles (GPMVs) isolated from cells are depleted of transmembrane proteins [56, 57, 58] while Gurdap et al. further showed glycosylation and extracellular protein size to be inversely correlated with ordered domain partitioning in GPMVs [17], suggesting that crowding is likely reduced in more ordered domains like lipid rafts, compared to the bulk of the cell. However, while plasma membrane vesicles undergo mesoscopic phase separation, lipids and proteins on live cells are known to form transient 10-200 nm domains and clusters, which often exist on sub-second timescales[59, 60, 50, 61, 62]. As a result, the optical characterization of small, transient protein and lipid clusters on live cells is challenging [63, 64, 65]. To probe the lateral crowding heterogeneities that one might expect to arise from the lateral segregation of membrane constituents mammalian cells, we used different antigen sensors that either distribute approximately uniformly on the cell surface, or self-associate to form clusters with unique local protein and lipid compositions. By measuring IgG binding to these different antigens on both reconstituted and live plasma membranes, we then show that cell surface crowding can vary laterally on nanometer length scales.

In this section, we present crowding measurements on phase-separated reconstituted giant unilamellar vesicles (GUVs) where spatially heterogenous crowding is engineered to

be easily visualized. We produced GUVs containing the ternary lipid mixture 2:2:1 1,2-dipalmitoyl-sn-glycero-3-phosphocholine (DPPC):DOPC:cholesterol, which phase separates into micron-scale liquid-ordered (Lo) and liquid-disordered (Ld) domains [66]. We preferentially crowded the Ld phase with 2% DOPE-PEG2k (Fig. 5.4A) and added DOPE-biotin and 1,2-dipalmitoyl-sn-glycero-3-phosphoethanolamine-N-(biotinyl) (DPPE-biotin) to present the biotin antigens in each phase. We measured the crowding energy for Biotin IgG binding to each domain (Fig. 5.4A). Consistent with the experiments in Figs. 5.1-5.2, the PEG brush inhibited antibody binding on the crowded Ld domain and increased the normalized effective K_D by 60% compared to the bare surface (Fig. 5.4B). In contrast, biotin binding in the less crowded Lo domain did not change relative to a bare membrane.

Although macroscopic phase domains on GUVs enable a simple measurement of lateral crowding heterogeneity, this approach is often impossible on live cell surfaces where hetergeneities can occur on diffraction-limited length scales. To address this challenge, we performed crowding measurements on SLB-coated beads with the same ternary lipid mixture, where the underlying substrate friction arrests phase domains into $\approx$ 90 nm nanoscopic features, similar to the size of lipid rafts and self-assembled protein clusters [67, 50, 62]. Since the individual phase domains cannot be identified, we measured the crowding on each phase by quantifying biotin IgG binding on beads containing only one type of antigen: either DPPE-biotin or DOPE-biotin.

As shown in Fig. 5.4B, we found that the Ld antigen (DOPE-biotin) reported a crowding penalty 7x higher than the Lo antigen (DPPE-biotin). While the absolute magnitudes of observed ΔU were higher on beads than GUVs, we attribute this difference to lower incorporation of DOPE-PEG2k through the GUV electroformation process. Given the strong qualitative difference in crowding reported by antibody binding to antigens partitioning into Lo or Ld domains, we conclude that laterally-segregating antigen probes

suitably report diffraction-limited lateral crowding heterogeneities.

5.2.5 Antibody binding to surface-clustering antigens reports lateral crowding heterogeneities

Motivated by our ability to measure crowding heterogeneities on nanoscopic phase domains on reconstituted membranes, we used cluster-forming proteins as antigen probes to measure in-plane crowding heterogeneities on live mammalian cells. It has been shown in-vitro that when cholera toxin B (CTB) binds to the ganglioside GM1, it can trigger the condensation of liquid-ordered lipid domains, enriched in CTB and GM1, from previously homogeneous lipid mixtures [68]. Not only are these 2D condensates enriched in CTB and GM1, but Hammond et al. showed that they can also exclude certain transmembrane proteins in-vitro [68]. Other in-vitro experiments have revealed that ganglioside-binding toxins can alter liquid-ordered domain composition and form self-associating clusters within phase domains [69]. We hypothesized that by leveraging the ability of CTB to form unique protein/lipid condensates on the surface, we could use anti-CTB antibody binding to probe crowding in a unique extracellular microenvironment, and thus gain insight into lateral crowding heterogeneities on live cells.

We bound Alexa Fluor 488-labeled CTB to HeLa human cervical cancer cells and T47D human breast cancer cells and measured crowding by comparing K_{D} of CTB IgG to that the intrinsic binding affinity on CTB on beads. CTB bound strongly to both cell lines, with approximately 40% greater binding on HeLa than on T47D (Fig. 5.4C, supplemental Fig. S10). We compared the K_{D} of CTB IgG to that of FITC binding to cholesterol-PEG0.5k-FITC sensors to differentiate CTB cluster-specific crowding from that of the bulk cell membrane (Fig. 5.4C). GM1 protrudes only 1-2 nm above the bilayer surface [70] and CTB is only about 2-3 nm in size [71], so we assume that crowding at

the CTB epitope is similar to that at the bilayer surface. While cholesterol-PEG-FITC has been observed to show a slight preference for ordered domains in GPMVs (26% greater enrichment in ordered domains) [72], we observed nearly uniform partitioning of cholesterol-PEG0.5k-FITC sensors between Lo and Ld phases on GUVs (supplemental Fig. S10), which is consistent with other work showing that functionalized cholesterol tends to favor the disordered phase due to its reduced packing efficiency [73, 53]. In addition, Windschiegl et al. showed that ganglioside-binding toxins can exclude Lo-favoring fluorescent dyes into the Ld phase on reconstituted bilayers [69]. Given these findings, we expect that any cholesterol-PEG-FITC enrichment in CTB/GM1 clusters is modest compared to that of CTB, and thus consider crowding reported by cholesterol-PEG0.5k-FITC to be approximately representative of the mean cell surface crowding.

We measured spatial crowding heterogeneities on human cervical cancer HeLa and human breast cancer T47D cells, both of which have surface proteomes rich in bulky proteins [74, 6]. Shurer et al. showed that wild type cells of both types form membrane tubules in response to high surface crowding [6]. The crowded surfaceomes of HeLa and T47D cells make these cells rich models for studying lateral heterogeneities. Bulk crowding for both cell lines as measured by our cholesterol-PEG0.5k-FITC sensors was on the order of 1-1.5 $k_{\mathrm{B}}T$, consistent with the brush exclusion energy on the surface of RBCs (Fig 5.4D).

On both cell lines, CTB antigens reported significantly less crowding than the cholesterol PEG FITC antigens, suggesting that the extracellular space around CTB is not heavily crowded with proteins and sugars (Fig. 5.4D). Moreover, less CTB bound to the surface of T47D than HeLa, but more CTB IgG bound to T47D (supplemental Fig. S10), offering further evidence that any reduction in IgG binding is due to local environmental factors, such as crowding. Between the two cell lines, the ratio of bulk to raft crowding free energy is also 18x greater in T47D than in HeLa, suggesting that the composition of

GM1-enriched domains is cell-specific, and that the lateral distribution of bulky extracellular proteins may vary considerably amongst different cell lines. Our unique ability to probe native cell membranes will advance further mechanistic insight into the roles of the actin cytoskeleton and other structural complexities on glycocalyx organization.

The reduction in crowding induced by CTB/GM1 clusters is qualitatively consistent with the results of Levental et al. [56, 57, 58] and Gurdap et al. [17] and supports the hypothesis that more ordered lipid domains of native membranes exclude proteins that contribute to extracellular crowding. This is a significant result because GPMVs exclude membrane proteins that are bound to the actin cytoskeleton, and it has long been unclear whether actin, myosin, and other structural features affect surface crowding. Our results reflect the first measurement to our knowledge of nanometer-scale crowding heterogeneity on an live plasma membrane, with intact cytoskeletal dynamics.

However, due to the fact that CTB both forms clusters and influences the local lipid composition, we cannot directly extrapolate our reduced CTB crowding to be representative of lipid rafts in general. CTB is known to drive GM1 association with caveolar invaginations in the membrane, and its lateral diffusion is restricted in an ATP-dependent manner that is not the norm for the GPI-anchored proteins that normally associate with rafts [48, 75]. Therefore, we conducted an additional control experiment to determine whether protein clustering alone is sufficient to alter the crowding landscape of the cell. We incubated HeLa in FITC-conjugated annexin V, a protein that binds to phosphatidylserine (PS) and forms a 2D lattice of repeating hexameric clusters on the membrane [62, 76]. PS is typically restricted to the intracellular leaflet of the plasma membrane on healthy cells, and thus our measurements were largely confined to blebbed regions of the membrane, in which PS was expressed the extracellular leaflet (see supplemental Fig. S12) [64]. Here, we found similarly reduced crowding to CTB (supplemental Fig. S12), suggesting that simply clustering antigen proteins together may be sufficient to

exclude other bulky extracellular proteins locally, leading to lateral variations in crowding.

5.3 Discussion

In this work, we developed a simple experimental technique to study the spatial heterogeneities of surface crowding on live cell membranes with exquisite spatial resolution. Alternative approaches like detergent resistant membranes (DRMs) and GPMVs [54] are invasive techniques that do not provide a description of surface organization in the native cell membrane environment. Prior to this work, existing techniques were capable of measuring spatial organization on cell surfaces with a very thick glycocalyx (0.2-1 µm), such as endothelial cells in the vasculature [77, 78, 79, 80]. However, studying the spatial organization of live cell surfaces with glycocalyx thicknesses of $\sim$ 10 nm was a challenge because standard optical microscopy cannot resolve nanometer variations.

While not reporting spatial heterogeneity, recent measurements with membrane-binding macromolecular probes reported osmotic pressures of 1-4 kPa at the surface of mammalian cells [23]. These surface pressures are comparable to and in some cases larger than the stiffness of the cell cortex ($\approx$ 1 kPa), providing new insight on the physical role of protein and glycan crowding on cell membranes. In this work, we demonstrated that these pressures are highly dependent on proximity to the membrane surface and that glycocalyx crowding decays rapidly away from the membrane. Our probes are physiologically relevant because many protein-protein interactions occur at a finite distance away from the membrane, like kinetic segregation in T-cell receptor triggering ($\approx$ 10-15 nm) [81, 82].

We present our antigen sensors on live cell surfaces with nanometer precision and use antibody binding equilibria to directly report spatial variations in surface crowding. Our

sensors achieve this nanometer spatial sensitivity by leveraging the exponential amplification of our readout (K_{D}) as a function of the crowding energy, $K_{\mathrm{D}} \sim \exp\left(\Delta U/(k_{\mathrm{B}}T)\right)$ (Eq. 5.1). This exponential amplification distinguishes our approach from previous techniques that rely on polymer brush height as the readout of crowding, which scales weakly with surface density, $h \sim n^{1/3}$ [19, 33, 22]. Taking the energy barrier to be proportional to the osmotic pressure, and in turn surface density, $\Delta U \sim \Pi \sim n^{9/4}$ [33, 22], we obtain the scaling $h \sim (\Delta U/(k_{\mathrm{B}}T))^{4/27}$, which is significantly weaker than $K_{\mathrm{D}} \sim \exp\left(\Delta U/(k_{\mathrm{B}}T)\right)$. The $\approx 1k_{\mathrm{B}}T$ change in crowding we observe within 6 nm of the RBC surface confirms this spatial sensitivity, and demonstrates the power of our technique in characterizing the highly heterogeneous membrane-proximal surfaceome, in which surface signaling and viral entry occur [30, 31].

Monoclonal antibody (mAb) drug candidates are currently screened using surface-plasmon resonance (SPR), in which binding affinity and avidity are measured on a bare hydrogel chip without regard to multi-body interactions [83]. With mAbs like the breast cancer treatment trastuzumab targeting a 4 nm tall epitope on human epidermal growth factor receptor 2 (HER2), probing local crowding variations may inform target selection and improve potency [31]. Indeed, Chung et al. found that trastuzumab and pertuzumab attenuate tubule structures enriched in HER2, suggesting that biophysical interactions like crowding may influence the potency of mAb therapies [84]. Our crowding measurements may also help inform the biophysical mechanisms governing antibody-dependent phagocytosis, which have been recently shown to have a strong dependence on the relative heights of the macrophage Fcγ receptor and the target cell surface proteins [13, 85]. In conclusion, our sensors may be used to inform important physiological processes, like antibody binding to buried surface receptors, membrane organization of lipid raft-like domains, and cellular phagocytosis.

When characterizing the RBC surface, we also demonstrated the potential to augment

experimental crowding measurements with an in-silico cell surface reconstruction based upon proteomics data. As recent advances in surface proteomics continue to better characterize glycocalyx components for a broad host of cell lines [44, 44, 45], we expect that accurate in-silico models will become possible on more complex mammalian cell surfaceomes. A technology to describe the extracellular crowding landscape for any cell a priori, using only proteomics data, may advance our basic understanding of cell membrane biology.

Using laterally-segregating antigen probes that exist in distinct crowding microenvironments on the plasma membrane, we demonstrated reduced crowding in GM1/CTB-enriched clusters on T47D and HeLa cells. These findings are consistent with the known reduction in transmembrane protein density on ordered domains in GPMVs [56, 57, 58], but our non-invasive measurements on live cells provide further insight into the dynamic cell surface ecosystem, including the interplay between the actin cytoskeleton and the membrane. Indeed, there has been considerable interest in the connection between the cytoskeleton and transmembrane protein organization over the past few decades [86, 87, 88], as actin is known to redistribute lipids and proteins on the cell surface [89, 65, 64, 90]. By bridging this gap and characterizing CTB-enriched clusters on live cells, we speculate that on length scales of order 10-100 nm, the cytoskeleton may not dramatically change bulky protein composition beyond that of equilibrium domains, supporting the use of actin-free systems like GPMVs to measure the lateral distribution of crowders [56, 17].

Viral particles like simian virus (SV) 40 and other polyomaviruses [91, 92], and toxins like Shiga and cholera toxin [93, 94], bind to gangliosides like GM1. SV40 virus is $\approx$ 45nm in size [95], about three times larger than an IgG. Since the mechanical work required to insert a particle into a crowded space scales approximately as the particle volume (see Supporting Information), a viral particle would be posed with an energy barrier of $\Delta U_{\text{virus}} \sim \Delta U_{\text{IgG}}(R_{\text{virus}}/R_{\text{IgG}})^3 \approx 20 - 30 k_{\text{B}}T$ if it tried to penetrate the glycocalyx

above the bulk membrane of T47D cells. In contrast, in ganglioside-enriched domains like those we study in this work, the binding penalty is merely $\Delta U_{\text{virus}} \approx 0.5 - 1 k_{\text{B}}T$ on T47D cells, suggesting that viral particles may experience a thirty-fold larger effective affinity towards the less-crowded, ganglioside-rich domains.

However, the discrepancy between relative raft-to-bulk crowding on HeLa and T47D cells indicates that the effect of GM1/CTB-enriched domains in reorganizing the glycocalyx varies considerably from cell to cell. Future direct comparisons between lateral heterogeneity on both live cells and their secreted membrane vesicles will provide a more thorough description of the fraction of extracellular bulk that remains anchored to the cytoskeleton in both disordered and raft-like membrane domains.

5.4 Methods

5.4.1 Antigen probe synthesis

Cholesterol-PEGx-NH_2, where x represents PEG0.5k, 2k, 5k, or 10k, was reacted with a 10x excess of N-hydroxy-succinimidyl ester (NHS)-FITC, overnight at 50°C in dimethylsulfoxide (DMSO). Unreacted FITC was removed via a 7K MWCO Zeba spin desalting column. SLB-coated beads were incubated with 100 nM FITC antigen sensors for 15 minutes at room temperature.

5.4.2 Microscope for all imaging experiments

All imaging was carried out on an inverted Nikon Ti2-Eclipse microscope (Nikon Instruments) using an oil-immersion objective (Apo 60x, numerical aperture (NA) 1.4, oil; Apo 100x, NA 1.45, oil). Lumencor SpectraX Multi-Line LED Light Source was used for excitation (Lumencor, Inc). Fluorescent light was spectrally filtered with emission filters

(432/36, 515/30, 595/31, and 680/42; Semrock, IDEX Health and Science) and imaged on a Photometrics Prime 95 CMOS Camera (Teledyne Photometrics). Microscope images were collected using MicroManager 1.4 software [96].

5.4.3 Sensor height measurement

Small unilamellar vesicles (SUVs) were formed using an established sonication method [13]. A lipid film containing 1,2-dioleoyl-sn-glycero-3-phos-phocholine (DOPC), 3% 1,2 dioleoyl sn glycero 3 phosphoethanolamine N [methoxy (polyethylene glycol) 2000] (DOPE-PEG2k), and DOPE-rhodamine was dried under nitrogen and then vacuum for 30 minutes. The film was rehydrated in Milli-Q (MQ) water to 0.2 mg/mL lipids, sonicated at low power using a tip sonicator (Branson SFX250 Sonifier) at 20% of maximum, 1s/2s on/off, for three minutes. We added MOPS buffer at a final concentration of 50 mM MOPS pH 7.4, 100 mM NaCl to the resulting SUV mixture. Then, 10 µL of 4 µm silica bead slurry (10% solids) was cleaned with piranha solution (3:2 H_2SO_4:H_2O_2) and washed three times with 1 mL MQ water before being suspended in 100 µL MQ water (1% solids). 3 µL of bead slurry was mixed with 30µL SUVs and incubated for ten minutes at room temperature before washing five times with HEPES buffer (50 mM HEPES pH 7.4, 100 mM NaCl).

FITC sensor heights were established using cell surface optical profilometry (CSOP) [31]. SLB-coated beads were incubated in 200 nM cholesterol-PEGx-FITC at room temperature for 15 minutes, where x represents PEG0.5k, 2k, 5k, and 10k. Unbound sensors were washed from the bulk and CSOP measurement used to find the difference in apparent bead radius on the 488 nm FITC channel and 555 nm rhodamine channel $\langle h_{\text{observed}} \rangle$. To correct for chromatic aberration, a baseline difference in 488nm and 555 nm radii $\langle h_{\text{baseline}} \rangle$ was measured on SLB-coated beads containing DOPC with 0.05% DOPE-

rhodamine, and 0.05% DOPE-Atto 488 lipids. The FITC antigen height was obtained by subtracting this baseline from the observed height: $\langle h \rangle = \langle h_{\text{observed}} \rangle - \langle h_{\text{baseline}} \rangle$.

5.4.4 Dissociation constant measurement for reconstituted PEG brushes

4 µm SLB-coated beads with PEG brushes were formed using a mixture of DOPC, 3% DSPE-PEG2k, and 0.05% DOPE-rhodamine. Bare beads for measuring $K_{\text{D},0}$ were formed with only DOPC and 0.05% DOPE-rhodamine. Beads were incubated in 100nM cholesterol-PEGx-FITC antigen sensors for 15 minutes at room temperature, then washed with HEPES buffer.

Lysine residues of anti-FITC (FITC) IgG antibodies were randomly labeled by reacting with 8x excess NHS-Alexa Fluor 647 for one hour at room temperature in 50 mM sodium bicarbonate solution. Unreacted dye was separated via a 7MWCO spin desalting column and the recovery and labeling ratio measured via Nanodrop UV-vis spectroscopy.

Coverslips were passivated with 1 mM bovine serum albumin (BSA) to prevent nonspecific antibody adsorption. Antigen-coated beads were added to coverslip wells containing FITC-647 and allowed to sediment and equilibrate with IgG for 30 minutes at room temperature. Bulk antibody concentrations ranged from 0.67 to 20 nM (see Source Data). At least 50 beads were imaged for each bulk IgG concentration, with an approximately equatorial focal plane. Images were subdivided into individual beads, and the edges identified by the brightest 5% of pixels, on the 555 nm (DOPE-rhodamine) channel, for each sub-image. The background intensity was taken to be the 30th percentile of FITC intensities for each bead subimage, and the bead intensity signal was calculated by subtracting background from the FITC signal associated with the brightest rhodamine pixels. The intensity signal for each bead was averaged to yield a mean bead signal, and

the mean bead signals were then averaged for each FITC bulk concentration, and fit to a Hill isotherm to find K_{D}.

5.4.5 Dissociation constant measurement for CD45 antigens

A GYPA brush with dilute CD45 antigens was reconstituted by incubating beads in 10:1 GYPA:CD45. SLB-coated beads containing DOPC, 8% 1,2-dioleoyl-sn-glycero-3-[(N-(5-amino-1-carboxypentyl) iminodiacetic acid)succinyl] (DGS-Ni-NTA), and 0.2% DOPE-Atto 390 were incubated with 10 nM His-tagged mouse CD45 and 100 nM His-tagged glycophorin A (GYPA) for 15 minutes at 37°C. Unbound protein was washed five times from the bulk with HEPES buffer. GYPA was labeled with NHS-Alexa Fluor 555 and CD45 was labeled with NHS-Alexa Fluor 488, and we thus confirmed a qualitative excess of the GYPA blockers on the beads. Beads were incubated in either Alexa Fluor 647-labeled C363 or I3 on CD45 for 30 minutes, and the K_{D} measured. Antibody bulk concentrations ranged from 0.33 to 20nM for C363 and 0.67 to 33 nM for I3 (see Source Data). Baseline $K_{\mathrm{D},0}$ for was measured for both CD45 epitopes on beads with no GYPA.

GYPA height was measured via CSOP using fluorescently-labeled purified anti-human glycophorin AB monoclonal antibody (clone HIR2), BioLegend (cat. no. 306602). Antibody was diluted to 10 nM.

5.4.6 Red blood cell (RBC) dissociation constant measurement

Single-donor human whole blood in K2-EDTA was purchased from Innovative Research and used within three days of arrival. The researchers in this study had no contact with human subjects and vendor samples were de-identified, precluding a need for IRB clearance. Blood was centrifuged at 300g for five minutes to isolate RBCs. For experiments with sialic-acid deficient red blood cells, red blood cells were treated with

100 mU/mL neuraminidase at 37°C for two hours. Cells were centrifuged and washed with PBS three times to remove bulk neuraminidase. RBCs were incubated with 100 nM cholesterol-PEGx-FITC (x represents PEG0.5k, 2k, 5k, and 10k) antigen sensors for 15 minutes at 37°C. RBCs were diluted 10x in PBS, centrifuged, and the supernatant discarded to remove unbound cholesterol. RBCs were washed in this way four more times, with a ∼100x dilution in fresh PBS each time. RBCs were added to FITC-647, pipette mixed, and incubated for 30 minutes before imaging. Antibody bulk concentrations ranged from 0.13 to 27 nM (see Source Data). RBC images were analyzed using the same methods as beads, with at least 50 cells per IgG concentration, to calculate K_{D}. For ΔU calculations, K_{D} was normalized against the bare-bead $K_{\mathrm{D},0}$, for each antigen.

5.4.7 Lateral crowding heterogeneity on mesoscale membrane domains

Antibody dissociation constants were measured on crowded and uncrowded coexisting domains in liquid-liquid phase-separated giant unilamellar vesicles (GUVs). DOPC, 1,2-dipalmitoyl-sn-glycero-3-phosphocholine (DPPC), and cholesterol were combined in a 2:2:1 ratio, which phase separates at room temperature [66]. 0.3% DOPE biotin and 0.05% 1,2 dipalmitoyl sn glycero 3 phosphoethanolamine N (biotinyl) (DPPE biotin) were added as liquid-disordered and liquid-ordered antigen probes, respectively. We set the relative amounts of DOPE- and DPPE-biotin such that the antigen density in each phase was approximately equivalent, as reported by Biotin binding. GUVs were formed either with or without 2% DOPE-PEG2k, which formed a crowding brush in only the liquid-disordered (Ld) phase. 0.05% each of DOPE-rhodamine and 1,2 distearoyl sn glycero 3 phosphoethanolamine N [poly (ethylene glycol) 2000 N' carboxyfluorescein] (DSPE-PEG2k-FITC) were also added to label the Ld and liquid-ordered (Lo) phases,

respectively.

GUVs were produced via a modified electroformation protocol [97, 98]. Lipids dissolved in chloroform were spread onto an indium tin oxide (ITO)-coated slide and the resulting film dried under vacuum for greater than 30 minutes. The lipid film was rehydrated in a 300 mM sucrose solution, placed in contact with a second ITO-coated slide, and an AC sinusoidal voltage applied across the two slides: 10 Hz/1.0 V for two hours then 0.4V/2 Hz for 20 minutes. GUVs were electroformed at 50°C to ensure phase mixing, then cooled below the melting point to room temperature once electroformation was stopped.

Phase-separated GUVs were incubated in Alexa Fluor 647-labeled Biotin antibody for at least 30 minutes. Antibody bulk concentrations ranged from 2 to 67 nM (see Source Data). The GUV size distribution spanned tens of microns, requiring that each vesicle be imaged individually to preserve a consistent equatorial focus. For each vesicle, Lo and Ld domains were identified by selecting the brightest 2% of pixels on the 488 (DSPE-PEG2k-FITC) and 555 nm (DOPE-rhodamine) channels, respectively, for each GUV image. The corresponding 647 nm intensities for these pixels were averaged and subtracted from the bottom 30th percentile of 647 intensities across the entire image, yielding a mean intensity for each phase. Lo and Ld intensities were averaged across all GUVs for each bulk IgG concentration and fit to a Hill isotherm to find K_{D} (with DOPE-PEG2k) and $K_{\mathrm{D},0}$ (without DOPE-PEG2k).

5.4.8 Lateral crowding heterogeneity on diffraction-limited domains

Antibody dissociation constants were measured for Lo- and Ld-favoring antigens on phase-separated SLBs, with kinetically-arrested nanoscopic domains. Beads were coated

with SLBs containing 2:2:1 DOPC:DPPC:cholesterol, with 0.05% DOPE-rhodamine Ld label and 1% DOPE-PEG2k Ld crowder. Only one of either DOPE-biotin or DPPE-biotin was also included, localizing the antigens primarily on either the Ld or Lo domains, respectively. Beads were incubated in Biotin-647, imaged, and K_{D} fit for each antigen. $K_{\mathrm{D},0}$ was measured with SLBs containing no DOPE-PEG2k.

5.4.9 Lateral crowding heterogeneity measurements on human cancer cells

Human cervical cancer HeLa and breast cancer T47D cells were obtained from ATCC. HeLa cells were cultured in Dulbecco's Modified Eagle Medium (DMEM) and T47D cells were cultured in RPMI 1640 Medium, both supplemented with 10% fetal bovine serum (FBS) and and 1% Pen-Strep. Cells were incubated at 37°C with 5% CO_2.

Cells were plated approximately 24 hours before imaging. Immediately before imaging, media was exchanged with PBS containing either 100 nM cholesterol-PEG0.5k-FITC and cholesterol-PEG0.5k-Alexa Fluor 555; 20 nM annexin V-FITC; or 100 nM Alexa Fluor 488-labeled cholera toxin B (CTB), and incubated for 20 minutes at 37°C. Unbound antigen was washed from the well five times with PBS.

Cells were incubated in either FITC-647 or CTB-647 for 30 minutes. Antibody concentrations ranged from 0.33 to 100 nM (see Source Data). At least 15 cells were analyzed for each bulk concentration. Fluorescence images of individual cells were captured, focusing on the equatorial plane, so that the plasma membrane outline was clearly visible. To select pixels for analysis, we took the product of the antigen and antibody signal for each pixel, identifying the top 7% for analysis. We took the mean IgG signal for these pixels, for each cell, to obtain the peak signal for that cell. In HeLa and T47D cell measurements, we observed some sensor internalization into the cell interior, but the antibody largely

remained on the exterior of the cell. Taking the product of IgG and antigen ensured that only plasma membrane signal was analyzed. For cells with cholesterol-PEG0.5k-FITC antigens, we used the co-incubated Alexa Fluor 555 constructs to identify the pixels of highest antigen density, because the FITC IgG quenches FITC. The background signal was set to the bottom 30th percentile of pixels, and the mean of the differences between peak and baseline for each cell taken to represent the surface-bound antibody. Bound antibody fraction was plotted against bulk IgG concentration and fit using the Hill isotherm (n=2) to find K_{D}.

The bare dissociation constant $K_{\mathrm{D},0}$ for CTB was measured on SLB-coated beads containing DOPC and 0.05% ovine brain GM1. Beads were incubated with 100 nM CTB for 15 min, washed, incubated in CTB for one hour, and then imaged. $K_{\mathrm{D},0}$ was fit to IgG intensity data according to the procedures in earlier bead experiments. For the cholesterol-PEG0.5k-FITC antigen, the $K_{\mathrm{D},0}$ value from earlier bead experiments was used. We calculated the free energies associated with CTB-reported raft-like domain crowding and FITC-reported bulk crowding using Eq. 5.1.

5.4.10 Molecular Dynamics Simulations

To validate theoretical predictions for the surface crowding profile, we performed coarse-grained molecular dynamics simulations using a graphics processing unit (GPU)-enabled HOOMD-Blue simulation package [99, 100]. We simulated membrane-bound PEG-conjugated FITC sensors using the Kremer-Grest bead-spring model [101] for polymers chains, with bead diameter $\sigma = 0.33$nm to represent the ethylene glycol monomer. One polymer end was confined to the bottom of the simulation box using wall potentials but was allowed to diffuse laterally [31]. We imposed periodic boundary conditions along x and y while the $z = \pm L_{\mathrm{z}}/2$ boundaries were impenetrable. We used a system box

size of $V = L^2 L_z$ where $L_z = 50 - 200\sigma$ and L was adjusted to achieve the specified surface density and number of chains. All particle pair interactions and wall potentials are modeled using the Weeks-Chandler-Anderson potential [102]. The bond potentials were modeled using the finite extensive nonlinear elastic (FENE) potential with spring constant $k = k_B T/\sigma^2$. The semiflexibility of polymer chains was imposed through a harmonic angle potential $U_B = \epsilon_B(1 - cos(\theta_{ijk} - \theta_0))$, where θ_{ijk} is the bond angle between adjacent particles (i, j, k), θ_0 is the resting angle, and $\epsilon_B = k_B T L_P/L_B$ is the bending energy, defined with persistence length $L_P = 0.97\sigma$ and bond length $L_B = \sigma$. We first simulated the experimental surface density of ∼1000 chains/μm^2 and averaged over ∼2000 polymers to verify that chains were dilute and non-interacting. We then simulated single chains and varied the degrees of polymerization to span PEG0.5k to PEG10k. Using simulation snapshots, we binned the spatial distribution of the FITC sensor normal to the surface, P_{FITC}. Single-chain dynamics were averaged over 15 simulations of 1000 snapshots each.

To characterize surface crowding, we separately simulated spherical antibody particles in the presence of surface-confined polymers. PEG2k crowders on reconstituted beads were modeled as a monodisperse polymer brush with degree of polymerization $N = 45$ and surface density of 30,000/μm^2 and averaged over ∼1000 chains. In separate simulations, we also modeled RBC cell surface proteins using a bidisperse polymer brush with the same coarse-graining as PEG. GYPA was coarse-grained into a 7-bead chain with a bead diameter of 4 nm, corresponding to the size of the sugar side chains along the backbone. Band 3 was coarse-grained into a 10-bead chain with 2 nm beads, representing the two large branches of the N-glycan. We chose surface coverages of 1300 and 6700 chains/μm^2 to match reported copy numbers of GYPA and Band 3. The Fab region of IgG was coarse-grained into a single spherical bead of size 4 nm in simulations of the reconstituted PEG2k brush, while the full IgG antibody was coarse-grained into an 11

nm bead in simulations of the RBC surface. The 2-3 nm PEG2k brush is smaller than a $\sim$ 10 nm IgG, so we assume only the Fab domain penetrates the reconstituted brush, while the full IgG penetrates the thicker RBC glycocalyx [103, 104].

We calculated the probability distribution of antibodies on the cell surface in the presence of crowding polymers or proteins, and used the Boltzmann relation to compute the repulsive energy penalty $U_{\text{brush}}(z) = -\ln\left(P_{\text{IgG}}\left(z\right)/P_{\text{bulk}}\right)$ of the brush at equilibrium. We numerically integrated Eq. 5.2 to compute the mean crowding energy $\langle \Delta U \rangle$ given height fluctuations in the FITC sensor (Figs. 5.2C, 5.3B).

5.5 Supplemental

MD Simulation Details

Coarse-grained model

The prepared systems are described using the overdamped Langevin equations of motion, also known as Brownian dynamics, where the velocity $\dot{\mathbf{x}}_i = \mathbf{F}_i/\gamma_i$ of particle i is numerically integrated forward in time and $\mathbf{F}_i$ is the sum of all forces on particle i. All simulations were performed using the GPU-enabled HOOMD-blue simulation package [100].

We coarse-grain (CG) PEG molecules as Kremer-Grest bead-spring polymer chains according to [105], where each CG bead represents the C-O-C monomer unit with length $\sigma = 0.33$ nm. Although our coarse-graining is at an atomic scale, we will still assume an implicit solvent in this simplified model and neglect any polymer interactions with the surrounding solvent molecules.

Non-bonded interactions between monomer pairs are modeled via a purely repulsive

Weeks-Chandler-Anderson (WCA) potential

$$V_{\mathrm{WCA}}\left(\mathbf{r}\right)=\begin{cases}0 & \text{if } |r|\geq 2^{1/6}\sigma\\ 4\epsilon\left(\left(\frac{\sigma}{|\boldsymbol{r}|}\right)^{12}-\left(\frac{\sigma}{|\boldsymbol{r}|}\right)^{6}\right) & \text{if } |r|<2^{1/6}\sigma\end{cases} \tag{5.3}$$

where we set $\epsilon = k_{\mathrm{B}}T$.

Bonded monomers along the polymer chain interact through the "finite extensible nonlinear elastic" (FENE) potential:

$$V_{\mathrm{FENE}}(\mathbf{r})=\frac{1}{2}kr_0^2\ln\left(1-\left(\frac{\mathbf{r}}{r_0}\right)^2\right)+V_{\mathrm{WCA}}\left(\mathbf{r}\right). \tag{5.4}$$

Additionally, the flexibility of polymer chains is represented using a harmonic bending potential:

$$V_{\mathrm{harm}}\left(\theta\right)=\frac{l_{\mathrm{p}}}{2l_{\mathrm{b}}}(\theta-\theta_0)^2 \tag{5.5}$$

where θ is the angle between three monomers along a chain. We choose the persistence length $l_{\mathrm{p}}=\sigma$ and equilibrium bond length as $l_{\mathrm{b}}=\sigma$.

All surface polymers are tethered using two wall-potentials V_{wall} which constrains the vertical position of the first monomer, similar to MD methods in [31].

Antibodies interact through a similar WCA potential with PEG monomers:

$$V_{\mathrm{WCA}}\left(\boldsymbol{r}\right)=\begin{cases}0 & \text{if } |r|\geq 2^{1/6}r_{\mathrm{a}}\\ 4\epsilon\left(\left(\frac{r_{\mathrm{a}}}{|\mathbf{r}|}\right)^{12}-\left(\frac{r_{\mathrm{a}}}{|\mathbf{r}|}\right)^{6}\right) & \text{if } |r|<2^{1/6}r_{\mathrm{a}}\end{cases} \tag{5.6}$$

where the equilibrium distance is $r_{\mathrm{a}}=\left(\sigma+d_{\mathrm{a}}\right)/2$ where d_{a} is the coarse-grained antibody diameter.

Average sensor height

We simulated sensor polymers at a surface density of $1000/\mu m^2$, in agreement with the experimental coverage of PEG-FITC conjugates on silica beads.

The degree of polymerization was varied from $N = 10$ to $N = 200$ to span the range of polymer contour lengths between PEG0.5k and PEG10k. After an initial equilibration period, we track the vertical height z of the end monomer above the surface, which corresponds to the location of the FITC sensor. The monomer hard sphere radius $r_{\mathrm{HS}} = 2^{1/6}\,(\sigma/2)$ was subtracted from z since the hard sphere bead never overlaps with the underlying surface. The spatial data were binned and averaged to compute the probability distribution $P(z)$ of sensor positions for various polymer linker lengths. The relationship between N and $\langle h \rangle$ is observed to follow $\langle h \rangle \sim N^{3/5}$, in agreement with Flory theory of a mushroom brush (Fig. 5.5). This result is expected given the diluteness of the polymer sensors on the surface.

Antibody insertion into PEG brush

We simulate free antibody with PEG2k polymers with $N = 45$ tethered to the cell surface at a surface density of $30000/\mu m^2$. After equilibration, the center of mass position of the antibody was binned as a function of height above the surface, and the hard sphere radius of the antibody was again subtracted such that $z = 0$ indicates antibodies that are flush with the cell surface. The size of an IgG antibody is ≈ 10 nm [103, 104], which is larger than the PEG2k brush size of $\approx 2 - 3$ nm. We assume that only the Fab region sticks into the PEG2k brush. Therefore, we modeled only the Fab region of the IgG with 4 nm spherical particles, which also recovered he experimentally observed brush potential of $\Delta U = 1 k_{\mathrm{B}} T$ at the surface. To obtain the effective brush crowding potential $\langle \Delta U \rangle$, numerical integration of Eq. **??** was performed and normalized by the effective potential

of the PEG0.5k sensor.

Coarse graining RBC proteins

Based on proteomics literature, we model the RBC cell surface as a bidisperse polymer brush consisting of the two most abundant proteins based on extracellular size and surface density, GYPA and Band 3 (Fig. 5.6). We choose the coarse-grained bead diameter of GYPA to be 4 nm, representing the 4-sugar side chain, and use $N = 7$ beads to maintain the contour length of GYPA to be roughly 28 nm. For Band 3, we coarse-grain the branched N-glycan on the extracellular domain into a single chain with 2 nm beads while choosing $N = 10$ to maintain the ≈ 20 nm contour length. In doing so, we have neglected the entropic penalty of confining these side branches, which may lead to slight underestimation of the crowding penalty. Since the RBC surface proteins are taller than the size of an IgG, we assume that the whole IgG interacts with the glycocalyx. Therefore, we modeled the IgG with 11 nm spherical particles, which recovered a repulsive penalty of $\Delta U = 2k_{\mathrm{B}}T$ at the surface, which is reasonable since the RBC brush is taller than the PEG brush and the bulk size of the antibody will dictate the repulsive potential. The effective brush potential $\langle \Delta U \rangle$ was then obtained similarly as in the PEG brush simulations.

Although we have coarse-grained the IgG into a spherical bead, in reality it has a Y-shaped structure consisting of two Fab and one Fc regions. Thus, one potential drawback to simulating the IgG as a spherical particle is the overestimation of the free energy penalty when inserted into the brush. Furthermore, only the Fab regions target and bind to the antigen, so our measured IgG affinity could deviate from experiments. However, our main simulation result is the brush crowding potential U, and we do not expect the IgG coarse-graining to have significant consequences other than a small overestimation of the osmotic penalties associated with insertion.

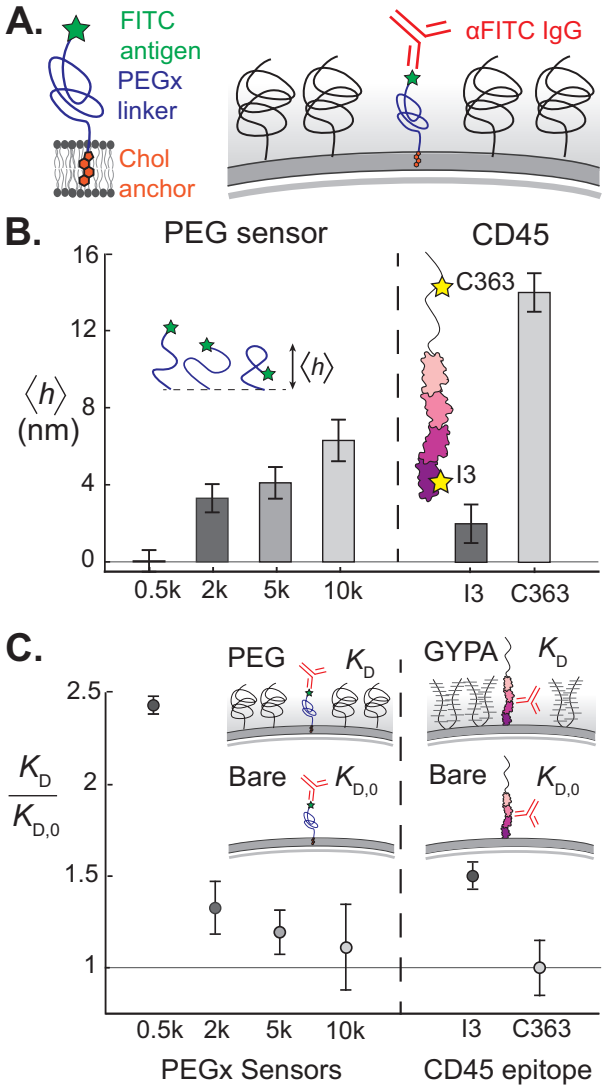

Figure 5.1: Synthetic antigen sensors enable precise localization and measurement of IgG binding avidity on crowded membrane surfaces. (A) Cholesterol-PEG-FITC sensors insert into the membrane and present the FITC antigen at varying heights above the membrane, depending on the PEG linker length. Sensors are exogenously inserted into reconstituted or live plasma membranes, and FITC IgG avidity is a direct reporter of local crowding. (B) (*Left*) Mean height $\langle h \rangle$ of synthetic antigen sensors increases as a function of PEG linker molecular weight, as measured by CSOP [31]. (*Right*) Epitope heights of two different CD45 antibodies, I3 and C363 on the transmembrane tyrosine phosphatase CD45, as reported by Son et al. [31]. (C) (*Left*) Dissociation constants of FITC to the synthetic antigen sensors on a supported lipid bilayer, containing 3% DOPE-PEG2k as a surface crowder. Dissociation constants are normalized by the bare membrane value, $K_{D,0}$. (*Right*) Two CD45 antibodies with distinct epitope heights experience a significant difference in normalized avidity on a reconstituted membrane crowded with a mucin-like glycoprotein, Glycophorin A (GYPA).

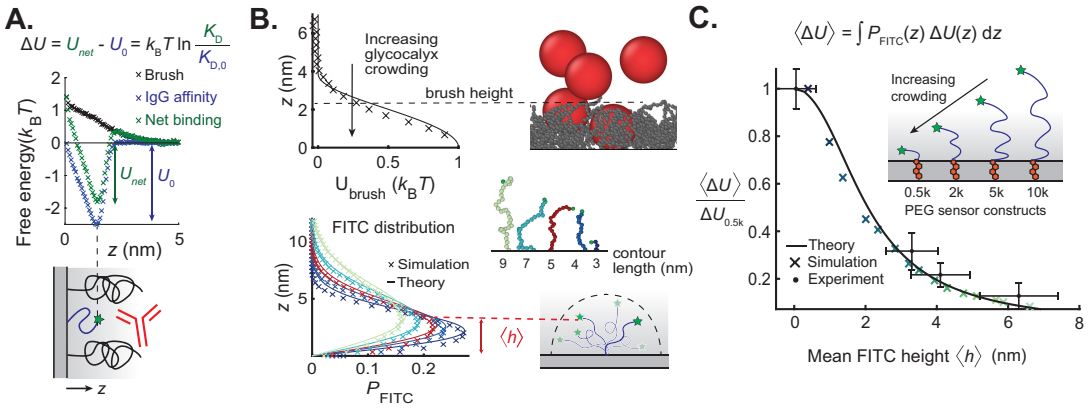

Figure 5.2: The binding avidity of macromolecules on crowded surfaces is a direct reporter of the energetic penalty posed by the crowded surface. (A) Coarse-grained molecular dynamics (MD) simulations of the IgG free energy versus height above the surface. The observed IgG avidity (U_{net}, green) is a superposition of an attractive enthalpic binding energy (U_0, blue) and a crowding-induced penalty due to crowding polymers (ΔU, black). Therefore, the normalized dissociation constants from Fig. 5.1C report the local energy penalty of the crowded surface. (B) (*Top left*) MD simulations of crowding penalty are re-plotted from Fig. 5.2A, with solid line indicating classical polymer brush theory [28]. (*Top right*) Simulation snapshot of antibody (red) on polymer (gray) coated surface. Weighting the crowding penalty by the FITC distribution yields a mean crowding penalty $\langle \Delta U \rangle$ for a sensor of given $\langle h \rangle$. (*Bottom left*) FITC position probability distributions for different polymer contour lengths based on continuous Gaussian chain model [32] (curve) and MD simulations (crosses). (*Bottom right*) MD snapshots of sensors of different linker lengths and illustration of average height $\langle h \rangle$ of a fluctuating FITC antigen. (C) Antibody avidity data from Fig. 5.1c are re-plotted to report steric crowding energy as a function of the mean FITC antigen height from Fig. 5.1B (black circles). Energies are normalized by the smallest antigen sensor size, $\Delta U_{0.5\mathrm{k}} = 0.9 k_{\mathrm{B}} T$. Theoretical prediction based on polymer brush theory (curve) agrees with experimental data and MD simulations (crosses).

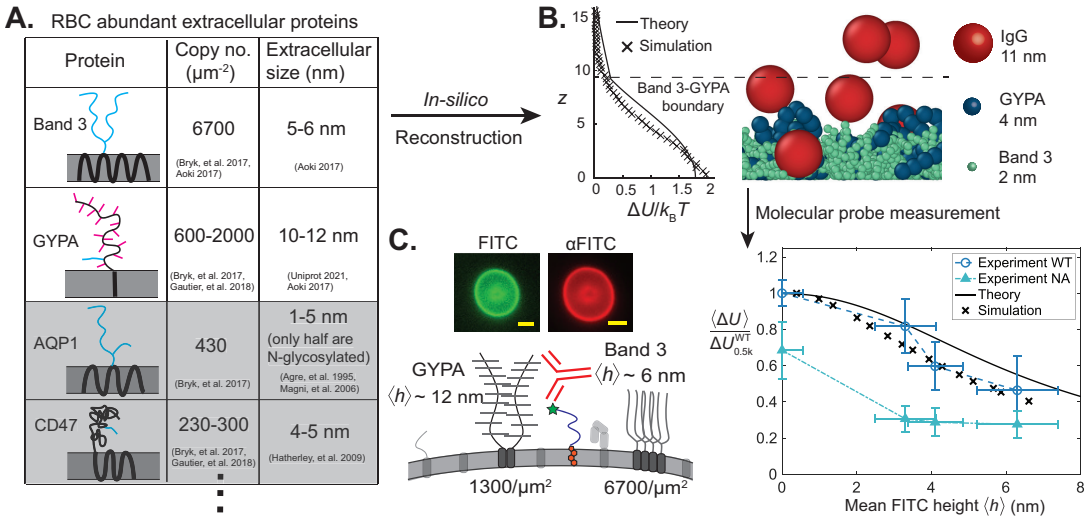

Figure 5.3: Red blood cell (RBC) membrane proteomics is integrated into an in-silico model to predict surface crowding heterogeneity validated by theory and experiments. (A) Relevant data from RBC proteomics for predicting surface crowding variation with extracellular height. Four of the most abundant RBC proteins with extracellular domains [35] are characterized according to copy number and extracellular domain size: Band 3, glycophorin A (GYPA), aquaporin 1 (AQP1), and CD47 [35, 36, 37, 38, 39, 40, 41]. Simplified schematics of transmembrane and extracellular domains are sketched in a lipid bilayer, with black peptide sequences, blue N-glycans, and magenta O-glycans. GYPA and Band 3 are the only proteins of sufficient extracellular size and density to be considered in our model. (B) MD simulations and analytical theory describe steric repulsion between an IgG antibody and a model RBC glycocalyx. (*Left*) Repulsive energy penalty ΔU from both analytical theory and MD simulation is plotted as a function of height. (*Right*) Snapshot of MD simulations with spherical IgG adsorbing to a bidisperse polymer brush of course-grained Band 3 and GYPA. (C) Molecular probes verify *in-silico* crowding heterogeneity predictions. (*Upper left*) Fluorescence micrographs demonstrate strong cholesterol-PEG-FITC sensor and anti-FITC IgG binding. Scale bar is 5 μm. (*Lower left*) Schematic of IgG binding to synthetic antigen sensors on an RBC surface, with GYPA and Band 3 dominating crowding. (*Right*) Mean crowding energy due to crowding ΔU, normalized by the surface value on wild type human red blood cells $\Delta U^{\mathrm{WT}}_{0.5\mathrm{k}}$ is plotted against mean sensor cholesterol-PEG-FITC sensor height $\langle h \rangle$. Analytical theory (black curve) and MD simulation (black crosses) predict weaker free energy penalties of crowding with increasing antigen sensor height on WT cells. Experimental measurements on WT red blood cells (blue circles) agree with theory and simulation, as crowding decreases similarly with height. Red blood cells treated with neuraminidase (NA) show reduced crowding overall (light blue triangles), with less height variation far from the surface. Dashed lines connecting experimental data are guides to the eye.

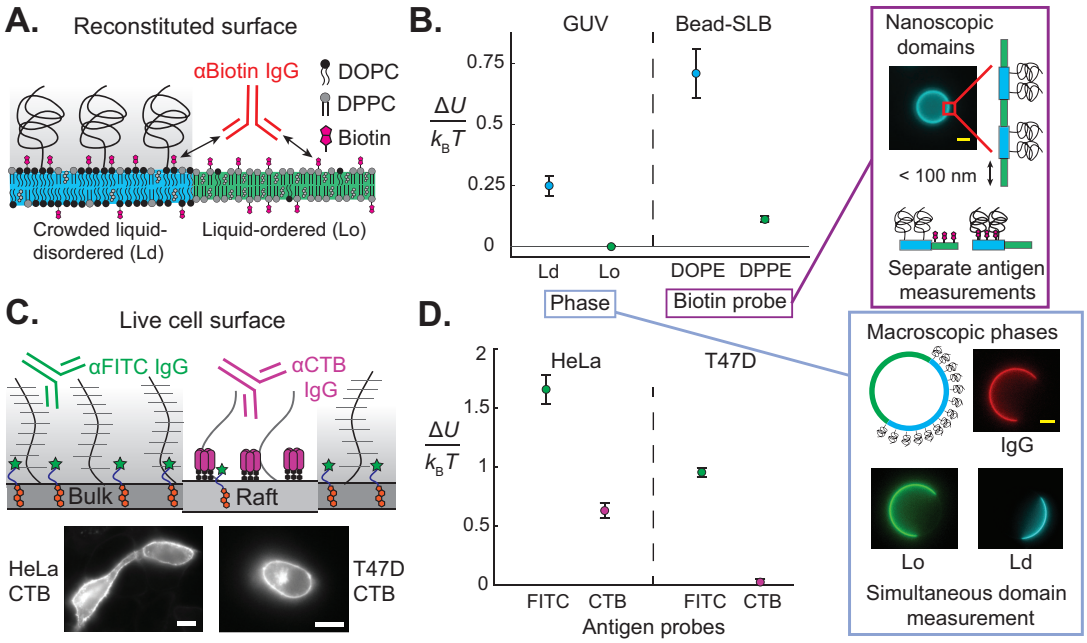

Figure 5.4: Antibody binding reports lateral crowding heterogeneities on membranes with coexisting domains. (A) Reconstituted ternary lipid mixtures of DOPC/DPPC/Cholesterol containing 2% DOPE-PEG2k produce preferential surface crowding in the liquid-disordered (Ld) phase compared to the liquid-ordered (Lo) phase. DOPE- or DPPE-conjugated biotin antigens were added to enable IgG antibody binding in the two phases. (B) Direct measurement of lateral crowding heterogeneity on macroscopic phase-separated domains in giant unilamellar vesicles (GUVs) yields similar trends to indirect crowding measurement of diffraction-limited domains on lipid-coated beads. (*Left*) The free energy due to crowding of a polyethylene glycol (PEG) brush is plotted for each domain on GUVs and for each antigen probe on kinetically-arrested SLBs on beads. (*Lower right inset*) We observed strong biotin IgG binding (image in red) only along the bare Lo surface (green), but not along the PEG-crowded Ld surface (blue) for the phase-separated GUVs. Scale bar is 5 µm. (*Upper right inset*) Ternary lipid mixtures on SLB-coated beads form nanoscopic domains due to arrested phase-separation caused by the underlying substrate friction, so we measured the crowding free energies with only one antigen sensor type at a time. DOPE-biotin prefers Ld and DPPE-biotin prefers Lo, so their avidities serve as an analog of local crowding in their respective phases. Scale bar is 2 µm. (C) Antigen probes partition amongst different cell membrane domains, enabling the direct characterization of lateral crowding heterogeneities on live cancer cells. (*Upper*) Cholera toxin B (CTB) antigens bind to ganglioside GM1, clustering and forming domains with a distinct protein/lipid composition, while cholesterol-PEG0.5k-FITC slightly favors the disordered bulk membrane. (*Lower*) HeLa and T47D cell membranes labeled with CTB. Scale bars are 10 µm. (D) Crowding free energy reported by CTB and FITC sensors on human cervical cancer HeLa and human breast cancer T47D cells.

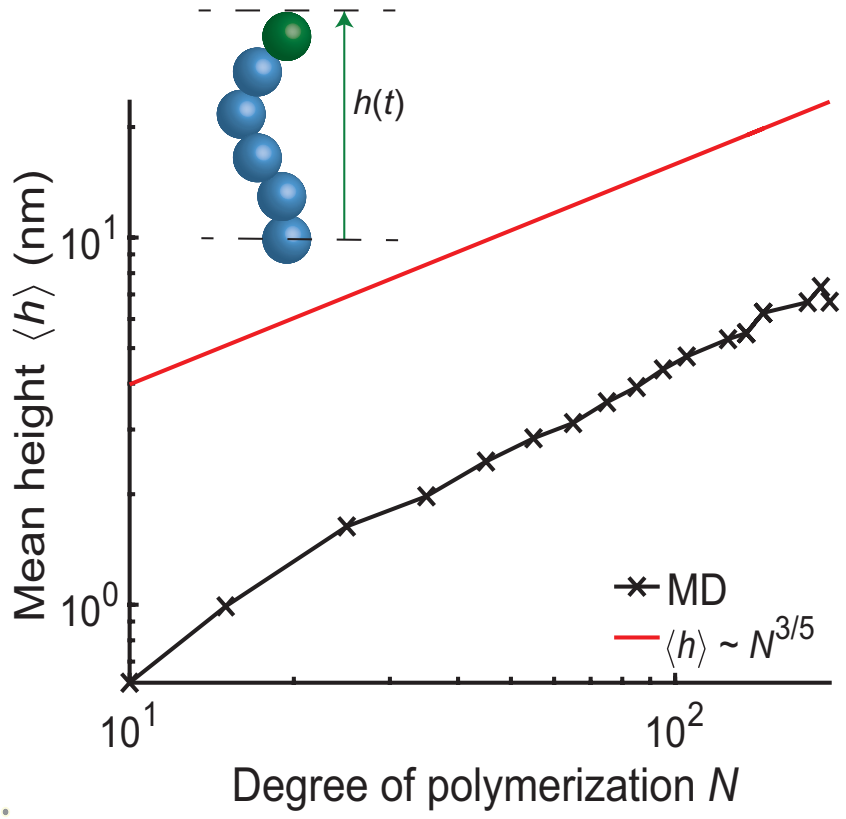

Figure 5.5: MD simulation of average height of FITC sensor. The average height of the FITC sensor (green) was obtained for various polymer degrees of polymerization, which is controlled by tuning the number of linker monomers (blue). The red theory line corresponds to a self-avoiding swollen polymer chain in a good solvent.

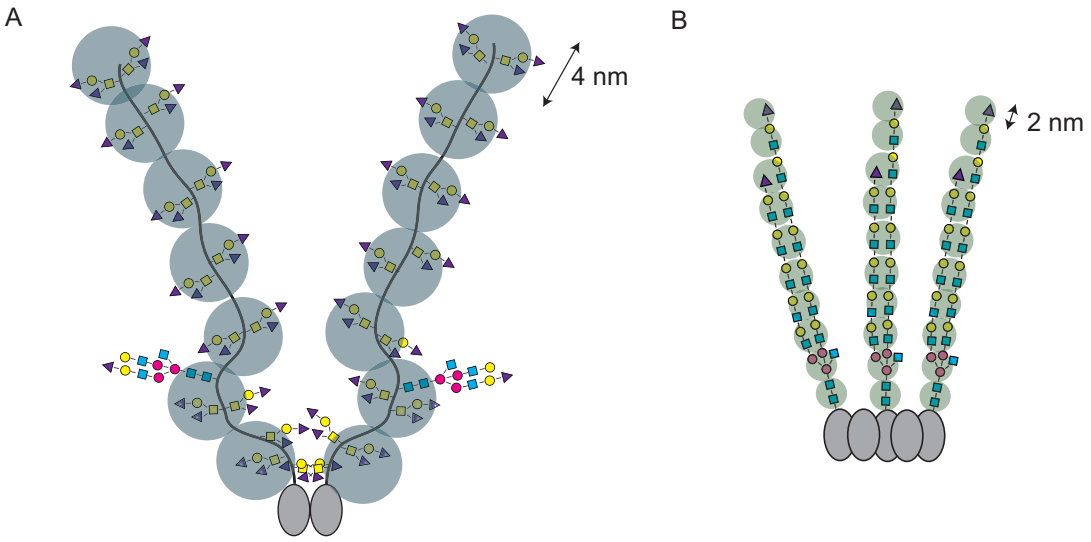

Figure 5.6: Coarse-graining of Glycophorin A (GYPA) and Band 3 on RBC glycocalyx. (A) In the molecular dynamics (MD) simulations, the extracellular domain of GYPA is modeled as two seven-bead polymer chains with bead diameter of 4 nm corresponding to the length of the sugar side chains. (B) Band 3 is modeled as three ten-bead polymer chains with bead diameter of 2 nm corresponding to a pair of sugars across the two side branches [36].

Bibliography

[1] Wilton T. Snead et al. "Membrane fission by protein crowding". In: *Proceedings of the National Academy of Sciences of the United States of America* 114 (16 2017), E3258–E3267.

[2] Jeanne C. Stachowiak et al. "Membrane bending by protein-protein crowding". In: *Nature Cell Biology* 14 (9 2012), pp. 944–949.

[3] David J. Busch et al. "Intrinsically disordered proteins drive membrane curvature". In: *Nature Communications* 6 (2015).

[4] Zhiming Chen, Ehsan Atefi, and Tobias Baumgart. "Membrane Shape Instability Induced by Protein Crowding". In: *Biophysical Journal* 111 (9 2016), pp. 1823–1826.

[5] Wade F. Zeno et al. "Dynamics of Crowding-Induced Mixing in Phase Separated Lipid Bilayers". In: *Journal of Physical Chemistry B* 120 (43 2016), pp. 11180–11190.

[6] "Physical Principles of Membrane Shape Regulation by the Glycocalyx". In: *Cell* 177 (7 2019), 1757–1770.e21.

[7] Wilton T. Snead et al. "BAR scaffolds drive membrane fission by crowding disordered domains". In: *Journal of Cell Biology* 218 (2 2019), pp. 664–682.

[8] Daniel J. Honigfort et al. “Glycocalyx crowding with mucin mimetics strengthens binding of soluble and virus-associated lectins to host cell glycan receptors”. In: *Proceedings of the National Academy of Sciences* 118 (40 2021), e2107896118.

[9] Sybille Rex et al. “Experimental and Monte Carlo simulation studies of the thermodynamics of polyethyleneglycol chains grafted to lipid bilayers”. In: *Biophysical Journal* 75 (6 1998), pp. 2900–2914.

[10] Hong Du, Parthapratim Chandaroy, and Sek Wen Hui. “Grafted poly-(ethylene glycol) on lipid surfaces inhibits protein adsorption and cell adhesion”. In: *Biochimica et Biophysica Acta (BBA) - Biomembranes* 1326 (2 June 1997), pp. 236–248.

[11] Rania Leventis and John R. Silvius. “Quantitative experimental assessment of macromolecular crowding effects at membrane surfaces”. In: *Biophysical Journal* 99 (7 2010), pp. 2125–2133.

[12] Hyunsook Jung et al. “Impact of hapten presentation on antibody binding at lipid membrane interfaces”. In: *Biophysical Journal* 94 (8 2008), pp. 3094–3103.

[13] Matthew H. Bakalar et al. “Size-Dependent Segregation Controls Macrophage Phagocytosis of Antibody-Opsonized Targets”. In: *Cell* 174 (1 2018). HeLa surface area 1600um, 131–142.e13.

[14] Nuray Gül and Marjolein Van Egmond. “Antibody-dependent phagocytosis of tumor cells by Macrophages: A Potent effector mechanism of monoclonal antibody therapy of cancer”. In: *Cancer Research* 75 (23 2015), pp. 5008–5013.

[15] Joe Chin Hun Kuo and Matthew J. Paszek. “Glycocalyx Curving the Membrane: Forces Emerging from the Cell Exterior”. In: *Annual Review of Cell and Developmental Biology* 37 (2021), pp. 257–283.

[16] Maryna Löwe et al. "The more the merrier: effects of macromolecular crowding on the structure and dynamics of biological membranes". In: *FEBS Journal* 287 (23 2020), pp. 5039–5067.

[17] Cenk Onur Gurdap et al. "Influence of the extracellular domain size on the dynamic behavior of membrane proteins". In: *Biophysical Journal* 121.20 (2022), pp. 3826–3836.

[18] Jade M. Noble et al. "Direct comparison of optical and electron microscopy methods for structural characterization of extracellular vesicles". In: *Journal of Structural Biology* 210 (1 2020).

[19] Justin R. Houser et al. "A Förster Resonance Energy Transfer-Based Sensor of Steric Pressure on Membrane Surfaces". In: *Journal of the American Chemical Society* 142 (49 2020), pp. 20796–20805.

[20] P. G. de Gennes. *Polymers at an interface; a simplified view*. 1987.

[21] S. T. Milner. "Polymer Brushes". In: *Science* 251.4996 (Feb. 1991), pp. 905–914.

[22] Michael Rubinstein and Ralph Colby. *Polymer Physics*. 1st ed. Oxford University Press, 2003.

[23] Sho C Takatori et al. "Engineered molecular sensors of cell surface crowding". In: *bioRxiv* (2022).

[24] Damaris Bausch-Fluck et al. "The in silico human surfaceome". In: *Proceedings of the National Academy of Sciences of the United States of America* 115 (46 2018), E10988–E10997.

[25] Christiaan Klijn et al. "A comprehensive transcriptional portrait of human cancer cell lines". In: *Nature Biotechnology* 33 (3 2015), pp. 306–312.

[26] Samuel B. Pollock et al. "Highly multiplexed and quantitative cell-surface protein profiling using genetically barcoded antibodies". In: *Proceedings of the National Academy of Sciences of the United States of America* 115 (11 2018), pp. 2836–2841.

[27] Marlon Stoeckius et al. "Simultaneous epitope and transcriptome measurement in single cells". In: *Nature Methods* 14 (9 2017), pp. 865–868.

[28] S. T. Milner, T. A. Witten, and M. E. Cates. "Theory of the Grafted Polymer Brush". In: *Macromolecules* 21 (8 1988), pp. 2610–2619.

[29] Anvy Moly Tom, Won Kyu Kim, and Changbong Hyeon. "Polymer brush-induced depletion interactions and clustering of membrane proteins". In: *The Journal of Chemical Physics* 154 (21 2021), p. 214901.

[30] Corleone S. Delaveris et al. "Membrane-tethered mucin-like polypeptides sterically inhibit binding and slow fusion kinetics of influenza A virus". In: *Proceedings of the National Academy of Sciences of the United States of America* 117 (23 2020), pp. 12643–12650.

[31] Sungmin Son et al. "Molecular height measurement by cell surface optical profilometry (CSOP)". In: *Proceedings of the National Academy of Sciences of the United States of America* 117 (25 2020), pp. 14209–14219.

[32] W. B. Russel, D. A. Saville, and W. R. Schowalter. *Colloidal Dispersions*. Cambridge University Press, Dec. 1989.

[33] A. Halperin. "Polymer brushes that resist adsorption of model proteins: Design parameters". In: *Langmuir* 15 (7 1999), pp. 2525–2533.

[34] A. K. Kenworthy et al. “Range and magnitude of the steric pressure between bilayers containing phospholipids with covalently attached poly(ethylene glycol)”. In: *Biophysical Journal* 68 (5 1995), pp. 1921–1936.

[35] Agata H. Bryk and Jacek R. Wiśniewski. “Quantitative Analysis of Human Red Blood Cell Proteome”. In: *Journal of Proteome Research* 16 (8 2017), pp. 2752–2761.

[36] Takahiko Aoki. “A comprehensive review of our current understanding of red blood cell (RBC) glycoproteins”. In: *Membranes* 7 (4 2017), pp. 1–19.

[37] Emilie Fleur Gautier et al. “Absolute proteome quantification of highly purified populations of circulating reticulocytes and mature erythrocytes”. In: *Blood Advances* 2 (20 2018), pp. 2646–2657.

[38] P. Agre, B. L. Smith, and G. M. Preston. “ABH and Colton blood group antigens on Aquaporin-1, the human red cell water channel protein”. In: *Transfusion clinique et biologique* 2 (4 1995), pp. 303–308.

[39] Alex Bateman et al. “UniProt: the universal protein knowledgebase in 2021”. In: *Nucleic Acids Research* 49 (D1 Jan. 2021), pp. D480–D489.

[40] Fulvio Magni et al. “Proteomic knowledge of human aquaporins”. In: *Proteomics* 6 (20 Oct. 2006), pp. 5637–5649.

[41] Deborah Hatherley et al. “Structure of Signal-regulatory Protein ”. In: *Journal of Biological Chemistry* 284 (39 Sept. 2009), pp. 26613–26619.

[42] Tao Jiang, Zhidong Li, and Jianzhong Wu. “Structure and swelling of grafted poly electrolytes: Predictions from a nonlocal density functional theory”. In: *Macromolecules* 40 (2 2007), pp. 334–343.

[43] Oliver Lieleg et al. “Mucin Biopolymers As Broad-Spectrum Antiviral Agents”. In: *Biomacromolecules* 13.6 (June 2012), pp. 1724–1732.

[44] Damaris Bausch-Fluck et al. “A mass spectrometric-derived cell surface protein atlas”. In: *PLoS ONE* 10 (4 2015), pp. 1–22.

[45] Zilu Zhou et al. “Surface protein imputation from single cell transcriptomes by deep neural networks”. In: *Nature Communications* 11 (1 2020), pp. 1–10.

[46] Kai Simons and Julio L. Sampaio. “Membrane organization and lipid rafts”. In: *Cold Spring Harbor Perspectives in Biology* 3 (10 2011), pp. 1–17.

[47] Mélanie Carquin et al. “Recent progress on lipid lateral heterogeneity in plasma membranes: From rafts to submicrometric domains”. In: *Progress in Lipid Research* 62 (2016), pp. 1–24.

[48] D. A. Brown and E. London. “Functions of lipid rafts in biological membranes”. In: *Annual Review of Cell and Developmental Biology* 14 (1998), pp. 111–136.

[49] Kai Simons and Elina Ikonen. “Functional rafts in cell membranes”. In: *Nature* 387 (6633 June 1997), pp. 569–572.

[50] Daniel Lingwood and Kai Simons. “Lipid Rafts As a Membrane-Organizing Principle”. In: *Science* 327 (5961 Jan. 2010), pp. 46–50.

[51] Deborah A. Brown and Erwin London. “Structure and function of sphingolipid- and cholesterol-rich membrane rafts”. In: *Journal of Biological Chemistry* 275 (23 2000), pp. 17221–17224.

[52] John R. Silvius. “Partitioning of membrane molecules between raft and non-raft domains: Insights from model-membrane studies”. In: *Biochimica et Biophysica Acta - Molecular Cell Research* 1746 (3 2005), pp. 193–202.

[53] Andrey S. Klymchenko and Rémy Kreder. “Fluorescent probes for lipid rafts: From model membranes to living cells”. In: *Chemistry and Biology* 21 (1 2014), pp. 97–113.

[54] Joseph Helmuth Lorent and Ilya Levental. “Structural determinants of protein partitioning into ordered membrane domains and lipid rafts”. In: *Chemistry and Physics of Lipids* 192 (2015), pp. 23–32.

[55] Rachel E. Lamerton et al. “The Role of Protein and Lipid Clustering in Lymphocyte Activation”. In: *Frontiers in Immunology* 12.March (2021), pp. 1–8.

[56] Ilya Levental, Michal Grzybek, and Kai Simons. “Raft domains of variable properties and compositions in plasma membrane vesicles”. In: *Proceedings of the National Academy of Sciences of the United States of America* 108 (28 2011), pp. 11411–11416.

[57] Kandice R Levental and Ilya Levental. “Chapter Two - Giant Plasma Membrane Vesicles: Models for Understanding Membrane Organization”. In: *Current Topics in Membranes* 75 (2015). Ed. by Anne K Kenworthy, pp. 25–57.

[58] Ilya Levental, Kandice R. Levental, and Frederick A. Heberle. “Lipid Rafts: Controversies Resolved, Mysteries Remain”. In: *Trends in Cell Biology* 30 (5 2020), pp. 341–353.

[59] Erdinc Sezgin et al. “Elucidating membrane structure and protein behavior using giant plasma membrane vesicles”. In: *Nature Protocols* 7 (6 2012), pp. 1042–1051.

[60] Linda J. Pike. “Lipid rafts: Bringing order to chaos”. In: *Journal of Lipid Research* 44 (4 2003), pp. 655–667.

[61] Ken Jacobson, Ping Liu, and B. Christoffer Lagerholm. "The Lateral Organization and Mobility of Plasma Membrane Components". In: *Cell* 177 (4 2019), pp. 806–819.

[62] H. A.M. Andree et al. "Clustering of lipid-bound annexin V may explain its anticoagulant effect". In: *Journal of Biological Chemistry* 267 (25 1992), pp. 17907–17912.

[63] Björn F. Lillemeier et al. "Plasma membrane-associated proteins are clustered into islands attached to the cytoskeleton". In: *Proceedings of the National Academy of Sciences of the United States of America* 103 (50 2006), pp. 18992–18997.

[64] Tore Skotland and Kirsten Sandvig. "The role of PS 18:0/18:1 in membrane function". In: *Nature Communications* 10 (1 2019), pp. 1–10.

[65] Riya Raghupathy et al. "Transbilayer lipid interactions mediate nanoclustering of lipid-anchored proteins". In: *Cell* 161 (3 2015), pp. 581–594.

[66] Sarah L. Veatch and Sarah L. Keller. "Separation of Liquid Phases in Giant Vesicles of Ternary Mixtures of Phospholipids and Cholesterol". In: *Biophysical Journal* 85 (5 2003), pp. 3074–3083.

[67] Alf Honigmann et al. "STED microscopy detects and quantifies liquid phase separation in lipid membranes using a new far-red emitting fluorescent phosphoglycerolipid analogue". In: *Faraday Discussions* 161 (2012), pp. 77–89.

[68] A. T. Hammond et al. "Crosslinking a lipid raft component triggers liquid ordered-liquid disordered phase separation in model plasma membranes". In: *Proceedings of the National Academy of Sciences of the United States of America* 102 (18 2005), pp. 6320–6325.

[69] Barbara Windschieg et al. “Lipid reorganization induced by Shiga toxin clustering on planar membranes”. In: *PLoS ONE* 4.7 (2009), pp. 1–11.

[70] Jinjun Shi et al. “GM1 clustering inhibits cholera toxin binding in supported phospholipid membranes”. In: *Journal of the American Chemical Society* 129 (18 2007), pp. 5954–5961.

[71] N. Ohtomo et al. “Size and structure of the cholera toxin molecule and its subunits.” In: *The Journal of infectious diseases* 133 Suppl (Supplement 1 Mar. 1976), pp. 31–40.

[72] Hong-Yin Wang et al. “Coupling of protein condensates to ordered lipid domains determines functional membrane organization”. In: *bioRxiv* (2022).

[73] Tobias Baumgart et al. “Fluorescence probe partitioning between Lo/Ld phases in lipid membranes”. In: *Biochimica et Biophysica Acta - Biomembranes* 1768 (9 2007), pp. 2182–2194.

[74] Nagarjuna Nagaraj et al. “Deep proteome and transcriptome mapping of a human cancer cell line”. In: *Molecular Systems Biology* 7 (548 2011), pp. 1–8.

[75] Charles A. Day and Anne K. Kenworthy. “Mechanisms underlying the confined diffusion of cholera toxin B-subunit in intact cell membranes.” In: *PloS one* 7 (4 2012).

[76] Yi Chih Lin, Christophe Chipot, and Simon Scheuring. “Annexin-V stabilizes membrane defects by inducing lipid phase transition”. In: *Nature Communications* 11.1 (2020), pp. 1–13.

[77] Sheldon Weinbaum, John M. Tarbell, and Edward R. Damiano. “The structure and function of the endothelial glycocalyx layer”. In: *Annual Review of Biomedical Engineering* 9 (2007), pp. 121–167.

[78] J. M. Tarbell and L. M. Cancel. "The glycocalyx and its significance in human medicine". In: *Journal of Internal Medicine* 280 (1 2016), pp. 97–113.

[79] Sheldon Weinbaum et al. "The Glycocalyx and Its Role in Vascular Physiology and Vascular Related Diseases". In: *Cardiovascular Engineering and Technology* 12 (1 2021), pp. 37–71.

[80] C. C. Michel. "Starling: The formulation of his hypothesis of microvascular fluid exchange and its significance after 100 years". In: *Experimental Physiology* 82 (1 1997), pp. 1–30.

[81] Simon J. Davis and P. Anton van der Merwe. "The kinetic-segregation model: TCR triggering and beyond". In: *Nature Immunology 2006 7:8* 7.8 (2006), pp. 803–809.

[82] Andrey S. Shaw and Michael L. Dustin. "Making the T cell receptor go the distance: A topological view of T cell activation". In: *Immunity* 6.4 (1997), pp. 361–369.

[83] Dina Lakayan et al. "Affinity profiling of monoclonal antibody and antibody-drug-conjugate preparations by coupled liquid chromatography-surface plasmon resonance biosensing". In: *Analytical and Bioanalytical Chemistry* 410 (30 2018), pp. 7837–7848.

[84] Inhee Chung et al. "High cell-surface density of HER2 deforms cell membranes". In: *Nature Communications* 7 (2016).

[85] Emily C. Suter et al. "Antibody:CD47 ratio regulates macrophage phagocytosis through competitive receptor phosphorylation". In: *Cell Reports* 36 (8 2021), p. 109587.

[86] Akihiro Kusumi et al. "Dynamic organizing principles of the plasma membrane that regulate signal transduction: Commemorating the fortieth anniversary of singer and nicolson's fluid-mosaic model". In: *Annual Review of Cell and Developmental Biology* 28 (2012), pp. 215–250.

[87] Akihiro Kusumi and Yasushi Sako. "Cell surface organization by the membrane skeleton". In: *Current Opinion in Cell Biology* 8 (4 1996), pp. 566–574.

[88] Ken Ritchie et al. "The fence and picket structure of the plasma membrane of live cells as revealed by single molecule techniques (Review)". In: *Molecular Membrane Biology* 20 (1 2003), pp. 13–18.

[89] Alf Honigmann et al. "A lipid bound actin meshwork organizes liquid phase separation in model membranes". In: *eLife* 2014 (3 2014), pp. 1–16.

[90] Concepción Gómez-Moutón et al. "Segregation of leading-edge and uropod components into specific lipid rafts during T cell polarization". In: *Proceedings of the National Academy of Sciences* 98 (17 Aug. 2001), pp. 9642–9647.

[91] Mengding Qian et al. "A lipid receptor sorts polyomavirus from the endolysosome to the endoplasmic reticulum to cause infection". In: *PLoS Pathogens* 5 (6 2009).

[92] Sabrina Engel et al. "Role of Endosomes in Simian Virus 40 Entry and Infection". In: *Journal of Virology* 85 (9 2011), pp. 4198–4211.

[93] Kirsten Sandvig et al. "Endocytosis and retrograde transport of Shiga toxin". In: *Toxicon* 56 (7 2010), pp. 1181–1185.

[94] Yukako Fujinaga et al. "Gangliosides That Associate with Lipid Rafts Mediate Transport of Cholera and Related Toxins from the Plasma Membrane to Endoplasmic Reticulm". In: *Molecular Biology of the Cell* 14 (12 Dec. 2003), pp. 4783–4793.

[95] Mariska G.M. Van Rosmalen et al. "Revealing in real-time a multistep assembly mechanism for SV40 virus-like particles". In: *Science Advances* 6 (16 2020), pp. 1–8.

[96] Arthur D Edelstein et al. "Advanced methods of microscope control using μManager software". In: *Journal of Biological Methods* 1.2 (Nov. 2014), e10.

[97] Miglena I Angelova and Dimiter S Dimitrov. "Liposome electroformation". In: *Faraday Discussions of the Chemical Society* 81 (1986), p. 303.

[98] Eva M Schmid, David L Richmond, and Daniel A Fletcher. "Reconstitution of proteins on electroformed giant unilamellar vesicles". In: *Methods in cell biology* 128 (2015), pp. 319–338.

[99] Joshua A. Anderson et al. "General purpose molecular dynamics simulations fully implemented on graphics processing units". In: *JCoPh* 227.10 (May 2008), pp. 5342–5359.

[100] Joshua A Anderson, Jens Glaser, and Sharon C Glotzer. "HOOMD-blue: A Python package for high-performance molecular dynamics and hard particle Monte Carlo simulations". In: *Computational Materials Science* 173 (2020), p. 109343.

[101] Kurt Kremer and Gary S Grest. "Dynamics of entangled linear polymer melts: A molecular-dynamics simulation". In: *The Journal of Chemical Physics* 92.8 (1990), pp. 5057–5086.

[102] John D. Weeks, David Chandler, and Hans C. Andersen. "Role of Repulsive Forces in Determining the Equilibrium Structure of Simple Liquids". In: *The Journal of Chemical Physics* 54.12 (Sept. 1971), p. 5237.

[103] Cristiano De Michele et al. “Simulation and Theory of Antibody Binding to Crowded Antigen-Covered Surfaces”. In: *PLoS Computational Biology* 12 (3 2016), pp. 1–17.

[104] Yih Horng Tan et al. “A Nanoengineering Approach for Investigation and Regulation of Protein Immobilization”. In: *ACS Nano* 2 (11 Nov. 2008), pp. 2374–2384.

[105] Hwankyu Lee et al. “A coarse-grained model for polyethylene oxide and polyethylene glycol: Conformation and hydrodynamics”. In: *Journal of Physical Chemistry B* 113 (40 2009), pp. 13186–13194.